Enabling communication and localization technologies for wireless capsule endoscopy

Ladić, Katjana

University of Zagreb

FACULTY OF ELECTRICAL ENGINEERING AND COMPUTING

Katjana Ladić

ENABLING COMMUNICATION AND LOCALIZATION TECHNOLOGIES FOR WIRELESS CAPSULE ENDOSCOPY

DOCTORAL THESIS

Zagreb, 2024

University of Zagreb

FACULTY OF ELECTRICAL ENGINEERING AND COMPUTING

Katjana Ladić

ENABLING COMMUNICATION AND LOCALIZATION TECHNOLOGIES FOR WIRELESS CAPSULE ENDOSCOPY

DOCTORAL THESIS

Supervisors:
Professor Dina Šimunić, Ph.D.
Kamran Sayrafian, Ph.D., Scientific Advisor

Zagreb, 2024

Sveučilište u Zagrebu

FAKULTET ELEKTROTEHNIKE I RAČUNARSTVA

Katjana Ladić

TEHNOLOGIJE ZA POTPORU KOMUNIKACIJE I LOKALIZACIJE BEŽIČNE ENDOSKOPSKE KAPSULE

DOKTORSKI RAD

Mentori:
prof. dr. sc. Dina Šimunić
dr. sc. Kamran Sayrafian, znanstveni savjetnik

Zagreb, 2024.

This doctoral thesis has been done at the University of Zagreb, Faculty of Electrical Engineering and Computing, Department of Wireless Communications. The research has been conducted at the Information Technology Laboratory of the National Institute of Standards and Technology.

Supervisors: Professor Dina Šimunić, Ph.D.
Kamran Sayrafian, Ph.D., Scientific Advisor

This doctoral thesis contains: 108 pages

Doctoral thesis number: _____

About supervisors

Dina Šimunić received B.Sc. and M.Sc. degrees in electrical engineering from the University of Zagreb, Faculty of Electrical Engineering and Computing (FER), Zagreb, Croatia, in 1985, and 1992, respectively. She received PhD at Graz University of Technology, Austria, in 1995. Since 1991 she is with Department for Wireless Communications at University of Zagreb, Faculty of Electrical Engineering and Computing.

She was a guest professor in research laboratories “Wandel & Goltermann” in Germany and Motorola Inc., USA in 1996. In 2007, she was promoted to Full Professor. In Croatia she served as a vice-president of Telecommunications Council. In the European Commission she acted as a vice-chair of COST for precompetitive research in information and communication technologies. Dr. Šimunić is a president of technical committee for telecommunications at Croatian Standards Institute. She is a leader of the group “Strategy towards the development of materials for education about standardization, as well as identification of common requirements” in ITU. She is the leader of the Scientific Green Engineering Laboratory (GEL). She participated in five and led three scientific projects of Croatian Ministry of Science, Education and Sports. She was WP coordinator of EU FP7 project: eWALL. She was a collaborator of the research project, financed through structural funds of EU, Ministry of Science, Education and Sports: “ICTGEN” (Information and Communication Technology for Generic and Energy-efficient Solutions with Application in e-/m- Health).

Prof. Šimunić participated in ten international program committees of scientific conferences, and she serves as a member of editorial board of international scientific journal JOSE (Journal of Structural Engineering), a reviewer of “Wireless Personal Communications”, and many other international scientific journals. She served as an editor-in-chief of the “Journal of Green Engineering”. She published more than 100 papers in journals and conference proceedings in the field of secure routing protocols against denial-of-service attack in mobile ad hoc networks, cognitive radio systems, radiofrequency simulations and biomedical effects of electromagnetic fields.

Kamran Sayrafian holds Ph.D. and M.S. degrees in Electrical and Computer Engineering from the University of Maryland and Villanova University, respectively. He is currently a Senior Scientist at the Information Technology Laboratory of the National Institute of Standards and Technology (NIST) located in Gaithersburg, Maryland where he leads a strategic program related to the application of the Internet-of-Things (IoT) in healthcare. He is also an affiliate Associate Prof. of Concordia University in Montreal, Canada since 2016 and the co-chair of the Vertical Track on Health and Well-Being at the COST CA20120 "Intelligence-Enabling Radio Communications for Seamless Inclusive Interactions". Prior to joining NIST, he was the cofounder of Zagros Networks, Inc. a fabless semiconductor company based in Rockville, Maryland where he served as the President and senior member of the architecture team.

Dr. Sayrafian has served as the Technical Program Committee and Executive Co-Chair of the IEEE PIMRC 2014 and organizer of several other IEEE Communication Society Conferences and international workshops focused on the applications of wireless communication in healthcare. He was also a member of the Editorial Board of the IEEE Wireless Communication Magazine from 2016 to 2020. His current research interests include body area networks, micro energy-harvesting, automatic exposure notification, and IoT technology in healthcare. He has published over 140 conference and journal papers, and book chapters, and has been the recipient of the IEEE PIMRC 2009, SENSORCOMM 2011, IEEE CSCN 2018 and IEEE EuCNC 2019 best paper awards.

Dr. Sayrafian was a major contributor to the development of the IEEE802.15.6 international standard on Body Area Networks; and the recipient of the 2015 U.S. Department of Commerce Bronze Medal for his contribution to this emerging field. In 2014, he also served as the U.S. Embassy Science Fellow in Croatia. Dr. Sayrafian is the co-inventor/inventor of four U.S. patents and a Fellow of the Washington Academy of Sciences.

O mentorima

Dina Šimunić je redoviti profesor Fakulteta elektrotehnike i računarstva u Zagrebu. Diplomirala je na Elektrotehničkom fakultetu u Zagrebu 1985., a magistrirala 1992. godine. Doktorirala je na Tehničkom Sveučilištu u Grazu, Austrija 1995. godine. 1991. godine zaposlila se na Fakultetu elektrotehnike i računarstva, gdje i danas radina na Zavodu za kominikacije.

Bila je gost profesor u istraživačkim laboratorijima "Wandel & Goltermann" u Njemačkoj i Motorola Inc., SAD 1996. Godine 2007. promaknuta je u redovnog profesora. U Hrvatskoj je obnašala dužnost potpredsjednice Vijeća za telekomunikacije. U Europskoj komisiji obnašala je dužnost potpredsjednice COST-a za istraživanja informacijskih i komunikacijskih tehnologija. Dr. Šimunić predsjednik je tehničkog odbora za telekomunikacije Hrvatskog zavoda za norme. Voditeljica je grupe "Strategija prema razvoju materijala za obrazovanje o standardizaciji, kao i identifikacija zajedničkih zahtjeva" u ITU-u. Voditeljica je Scientific Green Engineering Laboratory (GEL). Sudjelovala je u pet i vodila tri znanstvena projekta Ministarstva znanosti, obrazovanja i sporta RH. Bila je WP koordinator EU FP7 projekta: eWALL. Bila je suradnica na znanstveno-istraživačkom projektu financiranom iz strukturnih fondova EU, Ministarstva znanosti, obrazovanja i sporta: "ICTGEN" (Informacijska i komunikacijska tehnologija za generička i energetski učinkovita rješenja s primjenom u e-/m-zdravstvu).

Prof. Šimunić sudjelovala je u deset međunarodnih programskih odbora znanstvenih skupova, članica je uredništva međunarodnog znanstvenog časopisa JOSE (Journal of Structural Engineering), recenzentica je "Wireless Personal Communications" i mnogih drugih međunarodnih znanstvenih časopisa. Radila je kao glavna urednica časopisa "Journal of Green Engineering". Objavila je više od 100 radova u časopisima i zbornicima radova na konferencijama iz područja sigurnih protokola usmjeravanja protiv napada uskraćivanjem usluge u mobilnim ad hoc mrežama, kognitivnih radio sustava, radiofrekvencijskih simulacija i biomedicinskih učinaka elektromagnetskih polja.

Kamran Sayrafian stekao je diplomu u području elektrotehnike i računarstva na Sveučilištu Villanova, a doktorat na Sveučilištu Maryland. Trenutno je viši znanstvenik u Laboratoriju za informacijsku tehnologiju Nacionalnog instituta za standarde i tehnologiju (National Institute of Standards and Technology, NIST) smještenom u Gaithersburg, Maryland, gdje vodi strateški program vezan uz primjenu "Internet Stvari" (Internet of Things, IoT) u zdravstvu. Također je izvanredni profesor na Sveučilištu Concordia u Montreal, Kanada, od 2016. godine, te suorganizator "Vertical Track on Health and Well-Being" u okviru COST CA20120 "Intelligence-Enabling Radio Communications for Seamless Inclusive Interactions". Prije nego što je započeo raditi u NIST-u, bio je suosnivač tvrtke Zagros Networks, Inc., tvrtke za dizajn i razvoj poluvodiča sa sjedištem u Rockville, Maryland, gdje je obavljao dužnost predsjednika i višeg člana arhitektonskog tima.

Dr. Sayrafian je bio član odbora tehničkog programa i izvršni suorganizator na IEEE PIMRC 2014, te organizator nekoliko drugih konferencija poput "IEEE Communication Society Conferences" i međunarodnih radionica usmjerenih na primjenu bežičnih komunikacija u zdravstvu. Također je bio član uredničkog odbora časopisa "IEEE Wireless Communication Magazine" od 2016. do 2020. godine. Njegovi trenutni istraživački interesi uključuju mreže za prijenos signala ljudskim tijelom, mikroenergetsko prikupljanje energije, automatsko obavještavanje o izloženosti, te IoT tehnologiju u zdravstvu. Objavio je preko 140 konferencijskih i istrazivačkih radova u časopisima i književnim poglavljima, te je dobitnik nagrada za najbolje radove na "IEEE PIMRC 2009, "SENSORCOMM 2011", "IEEE CSCN 2018" i "IEEE EuCNC 2019".

Dr. Sayrafian bio je ključni suradnik u razvoju međunarodnog standarda IEEE802.15.6 za mreže za komunikaciju ljudskim tijelom i dobitnik brončane medalje U.S. Department of Commerce 2015. godine za doprinos tom rastućem području. 2014. godine također je služio kao znanstveni suradnik Veleposlanstva SAD-a u Hrvatskoj. Dr. Sayrafian je nositelj četiri američka patenta te član Washington Academy of Sciences.

Acknowledgements

This doctoral thesis would not have been possible without the help and encouragement from several people. First and foremost, I would like to express my deepest gratitude to my supervisors, Prof. Šimunić and Dr. Sayrafian, for their support and guidance throughout my PhD journey. I am especially thankful to Dr. Sayrafian for believing in me and giving me the opportunity to join NIST as a guest researcher and work on this research. Your continuous mentorship has been invaluable to me, and I am forever grateful.

I also want to extend my thanks to Wesley Griffin, Steven Satterfield, and John Hagedorn for their help and assistance during my work within the NIST immersive platform.

A big thank you goes to Ivana for all the help, support, and our long chats, regardless of the time zone difference. Your friendship means the world to me, and I am grateful to have you in my life.

I would like to express my deepest appreciation and love to my family for their endless support, encouragement, and understanding. And to my brother, thank you for being an inspiration even before I decided to follow your footsteps and study at FER.

And above all, I am incredibly grateful to my husband for his willingness to relocate to another continent for me. Your love and support gave me the strength to keep going. I would never have made it without you, *Ljubi*.

Summary

Endoscopy procedure plays a significant part in nearly all gastrointestinal related diseases as well as a crucial role in clinical research. A wireless capsule endoscopy is an ingestible capsule equipped with a miniaturized video camera that allows observation of abnormalities in the entire length of the small intestine from locations that are not accessible by conventional endoscopy or colonoscopy technology. The research in this thesis mainly focuses on two communication technologies, Ultra-Wideband and Human Body Communication, that can meet the higher data rate and/or lower communication power consumption of the next generation capsules.

A statistical pathloss model that effectively captures the impact of transmitter antenna orientation as well as various body tissues as the capsule moves along its natural path inside the small intestine was obtained for UWB frequency range. To obtain this model, a 3D immersive platform including a detailed computational human body and gastrointestinal tract models that allow for an in-depth study of the wireless propagation channel between a capsule and on-body receivers and an innovative methodology that enables judicious placement of the capsule along its natural trajectory inside the small intestine were developed. Partial model verification and the potential impact of the measurement points distribution on the extracted pathloss exponent is also presented.

The obtained pathloss was contributed to the IEEE revision of the 15.6 standard and was accepted as a standard channel model document for the Capsule Endoscopy use-case.

Using inverse Fast Fourier Transform, time domain responses of the channels were obtained to perform the time domain characteristics and multipath propagation analysis. In addition to the communication technologies, methodologies that can assist in estimating the position or orientation of a capsule endoscope were studied. The algorithms to estimate the orientation of the capsule inside the small intestine using received signal strength were developed and tested to assess capsule orientation estimation with respect to a reference position.

HBC technology is another candidate for the next generation of capsule endoscopy. A FEM-based parametric simulation platform including a full 3D computational human body model was presented. The parameters of the model are all design variables that can be adjusted to emulate specific measurement scenario. The developed customizable computational platform allows comprehensive study of the HBC channel by considering different electrode sizes and placements on the surface and inside the human body.

Keywords: capsule endoscopy, computational human body models, statistical pathloss model, ultra-wideband, time response, multipath propagation, human body communication, capacitive coupling

Sažetak

Tehnologije za potporu komunikacije i lokalizacije bežićne endoskopske kapsule

BAN je radio komunikacijska mreža u kojoj se mrežni čvorovi nalaze unutar, na površini ili oko ljudskog tijela. IEEE 802.15.6 standard je BAN standard za tri komunikacijska protokola: uskopojasni, ultraširokopojasni (UWB) i komunikacija ljudskim tijelom (*eng. Human Body Communication*, *HBC*). Standard je trenutno u postupku revizijw s fokusom na proširenje UWB-a na implantate ili ugradive elektronske senzore, i unesive elektroničke senzore ili senzore koji se unose u tijelo gutanjem. Jedna od specifičnih primjena koja se razmatra unutar revizije standarda je endoskopska kapsula.

Kao jedna od BAN primjena, bežična endoskopija kapsulom (*eng. Capsule Endoscopy, CE*) nudi bezbolnu vizualizaciju cijelog gastrointestinalnog trakta i trenutno je jedina dijagnostička tehnologija koja može pregledati cijelu dužinu tankog crijeva. Endoskopska kapsula je oblika cilindrične tablete i sastoji se od kamere, izvora svjetlosti, baterije i radio odašiljača. Endoskopske kapsule postižu veliku popularnost, posebice jer omogućuju potpuni pregled probavnog sustava bez ikakvih neugodnosti i komplikacija. Međutim, postojećim komercijalnim endoskopskim kapsulama potreban je dug vremenski period za slanje slika iz probavnog trakta do prijamnika. Razlog za tako dugo vrijeme slanja podataka leži u nedostacima RF pojasa pri niskim frekvencijama kao što su MICS (*eng. Medical Implant Communication Service)* i ISM (*eng. Industrial, Scientific and Medical*) frekvencijski pojasevi. Kako bi se izbjegli nedostaci pri niskim frekvencijama, kreće se prema UWB pojasu (3,1 GHz do 10,6 GHz) koji omogućava veće brzine prijenosa podataka i slanje slika veće rezolucije, kao i nižu potrošnju snage.

Ovaj doktorski rad rezultat je istraživanja u području bežičnih tehnologija za nosive, ugradive i unesive elektronske senzore s naglaskom na primjenu u endoskopiji bežičnom kapsulom. Istraživanje se usredotočuje na sljedeću generaciju endoskopskih kapsula koje mogu zadovoljiti veću brzinu prijenosa podataka i/ili manju potrošnju energije. Proučavane su dvije komunikacijske tehnologije koje se mogu koristiti za sljedeću generaciju bežičnih endoskopskih kapsula, ultraširokopojasna (UWB) i komunikacija ljudskim tijelom (HBC). Osim komunikacijskih tehnologija, dio istraživanja također se usredotočuje na metodologije koje mogu pomoći u procjeni položaja ili orijentacije endoskopske kapsule. Kako bi se inicirala studija korištenja UWB tehnologije, razvijen je fleksibilan i interaktivni imerzivni platformski sustav koji sadrži poboljšani 3D model tijela i realistične antene. Platforma može oponašati komunikacijsku vezu između endoskopske kapsule i nekoliko prijemnih senzora na tijelu, te je korištena za proučavanje karakterizacije kanala za bežičnu endoskopsku kapsulu. Razvijena platforma također je proširena dodatnim alatima koji omogućuju procjenu orijentacije, koja je samo jedan dio puno složenijeg problema pozicioniranja kapsule unutar probavnog trakta. U sklopu istraživanja orijenatije kapsule, provedena je preliminarna studija procjene orijentacije kapsule temeljena na jačini primljenog signala (*eng. Received Signal Strength, RSS*). Za istraživanje komunikacije ljudskim tijelom (HBC) i mogućnosti primjene HBC tehnologije za sljedeću generaciju endoskopske kapsule, razvijen je svestran i prilagodljiv model baziran na metodi konačnih elemenata (*eng. Final Element Method, FEM*) koji omogućuje sveobuhvatno proučavanje HBC kanala na površini i unutar ljudskog tijela.

Prvo poglavlje opisuje važnost teme istraživanja i pruža pregled tehnologije ultra-širokopojasnog pojasa (UWB) i tehnologije prijenosa signala ljudskim tijelom (HBC) u literaturi. Poglavlje također sadrži detaljni pregled prethodnih istraživanja karakterizacije komunikacijskog kanala kroz ljudsko tijelo korištenjem tih tehnologija. Studije u ovom području su izazovne i sadrže razna ograničenja. Istraživanja se najčešće provode korištenjem različitih simulacijskih ili eksperimentalnih scenarija i antena za endoskopsku kapsulu koje nisu praktične i realne za ovu primjenu, što dovodi do razlika u rezultirajućim karakteristikama širenja signala. U ovom doktroskom istraživanju posebna pažnja dana je odabiru praktičnih antena za primjenu kod endoskopskih kapsula. Također je predstavljena i metodologija za pažljivo postavljanju antene kapsule unutar tankog crijeva kako bi se postigla željena statistička distribucija udaljenosti i što realističnije opisao komunikacijski kanal i model gubitaka.

Za HBC i primjenu te tehnologije za unosive i unesive elektroničke senzore postoji tek nekoliko studija u literaturi. Provođenje fizičkih eksperimenata s uređajima unutar ljudskog tijela gotovo je nemoguće; stoga se mjerenja kanala za HBC u tijelu obično izvode

korištenjem tekućih ili tkivnih fantoma ili računalnih simulacija. Međutim, rezultati uvijek ovise o uvjetima mjerenja, posebice o vrsti i veličini elektroda i razmaku između elektrodnih ploča. Ciljevi istraživanja te kratak pregled sadržaja rada zaključuju ovo poglavlje.

Drugo poglavlje opisuje razvoj nove 3D imerzivne virtualne vizualizacijske platforme koja omogućuje oponašanje prostiranja radiofrekvencijskih (RF) signala između endoskopske kapsule i nekoliko prijemnika na površini tijela. Platforma omogućuje sveobuhvatno istraživanje bežičnog komunikacijskog kanala kroz ljudsko tijelo za ugradive ili unesive elektronske senzore na UWB frekvencijama. Opisane su ključne komponente platforme, poput modela probavnog trakta visoke razlučivosti i kapsule/senzora na tijelu. Za ovo istraživanje, položaji prijemnika odabrani su na temelju lokacije senzora za postupak endoskopije korištenjem komercijalne PillCam kapsule. Korišteno je ukupno 10 prijemnika raspoređenih po površini trbuha. S ovim prijamnicima, svaki položaj antene kapsule unutar probavnog trakta rezultira s 10 neovisnih komunikacijskih kanala širenja signala. Također je predstavljena metodologija za pažljivo postavljanje kapsule unutar tankog crijeva. U tu svrhu, izračunata je 3D središnja linija kao prosjek svih mogućih puteva kroz tanko crijevo. Zatim su položaji kapsule odabrani postavljanjem antene duž te središnje linije. Metodologija za pronalaženje najboljih položaja antene kapsule uključuje razvoj nekoliko interaktivnih alata koji se mogu koristiti u imerzivnoj platformi opisanoj ranije. Položaji antene kapsule moraju pokrivati cijelo područje tankog crijeva, a također je važno imati dovoljan broj mjernih uzoraka koji su ravnomjerno raspoređeni u cijelom rasponu udaljenosti odašiljača i prijemnika. Zadovoljavanje ovih uvjeta rezultira preciznijim i realnijim vrijednostima parametara u statističkom modelu gubitaka. Poglavlje zaključuje utvrđivanjem odgovarajućeg skupa scenarija simulacije za prostiranje radiokomunikacijskih valova i mjerenje komunikacijskog kanala.

U trećem poglavlju definiran je model gubitka za propagacijski kanal bežične endoskopske kapsule i navedeni su detalji o izračunu parametara modela. Predstavljeni statistički model gubitaka je model logaritamske udaljenost i uključuje komponentu sjenjenja koja učinkovitije predočuje utjecaj različitih električnih svojstva tkiva tijela, kao i orijentaciju antene za frekvencijski raspon od 3,1 GHz do 4,1 GHz. Uobičajeno je kod drugih primjena da komponenta sjenjenja opisuje samo sjenjenje zbog prepreka u okruženju prostiranja signala. Međutim, u primjeni za endoskopsku kapsulu, budući da je antena kapsule dio komunikacijskog kanala, komponenta sjenjenja uključuje i utjecaj neizotropnog dijagrama zračenja antena. Ovo poglavlje također opisuje i djelomičnu provjeru modela i potencijalni

utjecaj distribucije mjernih točaka na dobiveni eksponent gušenja signala.
Dobiveni model gubitaka prihvaćen je u IEEE reviziji standarda 802.15.6 i kao standardni dokument modela kanala za primjenu kod endoskopske kapsule.
Korištenjem inverzne brze Fourierove transformacije dobiveni su vremenski odzivi kanala. Za unosive ili unesive senzore općenito se pretpostavlja da okolina ljudskog tijela uzrokuje jako višestazno širenje zbog mogućih refleksija, difrakcija ili raspršenja od različitih slojeva tkiva. Međutim, nedostaju detaljna istraživanja o jačini višestaznog širenja i utjecaju na primljeni signal. Za istraživanje višestaznog širenja, detaljno se pretražilo vremenske odzive svih 200 kanala između antene endoskopske kapsule i senzora na površini tijela kako bi se našli primjeri ili scenariji u kojima je vidljiva jaka reflektivna komponenta signala. Proučavanje odziva kanala otkrilo je višestazno širenje s malim brojem putanja (obično jedna izravna i jedna neizravna putanja). Stoga se pretpostavlja da bi model putanje kašnjenja za endoskopsku kapsulu na UWB frekvencijama uglavnom uključivao dvije glavne putanje, jednu izravnu (*eng. line of sight, LOS*) i jednu neizravnu (*eng. non-line of sight, NLOS*).

Četvrto poglavlje opisuje metodologije koje mogu pomoći u procjeni položaja i/ili orijentacije endoskopske kapsule. Revolucionarni utjecaj endoskopske kapsule u medicini je što omogućuje otkrivanja abnormalnosti unutar cijele dužine tankog crijeva s mjesta koja nisu dostupna tijekom ispitivanja s tradicionalnim dijagnostičkim tehnologijama endoskopije ili kolonoskopije. Međutim, pozicioniranje i mapiranje u ovom području još uvijek je u ranoj fazi. Elastičnost probavnog trakta, kao i petljasta i presavijena priroda njegovih komponenti, zajedno s promjenjivom brzinom i isprekidanim načinom kretanja endoskopske kapsule predstavljaju nekoliko jedinstvenih izazova za ovaj problem. Stoga, do sada, ne postoji pouzdana metodologija koja može točno odrediti lokaciju i/ili orijentaciju endoskopske kapusle unutar tankog crijeva probavnog trakta. Budući da kamera unutar kapsule ima ograničen kut vidnog polja, informacija o orijentaciji kapsule unutar tankog crijeva probavnog trakta također može biti značajna. Vizualizacijska platforma, opisana u drugom poglavlju, proširena je dodatnim alatima i korištena za razvoj algoritama za procjenu orijentacije kapsule unutar tankog crijeva. Rezultati ukazuju da se bilo koja usmjerenost u dijagramu zračenja antene kapsule može iskoristiti za procjenu orijentacije preko mjerenja jačine dolaznog signala na prijemnicima na tijelu. Mogućnost praćenja položaja i/ili orijentacije kapsule tijekom endoskopije značajno će povećati dijagnostičke mogućnosti endoskopske kapsule.

Peto poglavlje usredotočuje se na tehnologiju prijenosa signala ljudskim tijelom (HBC) koja je još jedan od kandidata za sljedeću generaciju endoskopske kapsule. Jedan od

nedostataka istraživanja HBC tehnologije je što rezultati uvijek ovise o uvjetima i scenarijima mjerenja. U ovom radu predstavljena je platforma koja sadrži cjeloviti 3D računalni model ljuskog tijela i omogućuje parametarske simulacije na temelju metode konačnih elemenata (FEM). Parametri modela mogu se proizvoljno prilagoditi kako bi oponašali određeni scenarij mjerenja. Time se omogućuje sveobuhvatno istraživanje HBC komunikacijskog kanala uzimajući u obzir različite veličine i položaje elektroda na površini i unutar ljudskog tijela.

U šestom poglavlju sažeti su glavni zaključci istraživanja. Iznesena su najvažnija postignuća i znanstveni doprinosi, te su predloženi potecijalni smjerovi za buduća istraživanja.

Ključne riječi: endoskopska kapsula, računalni model ljudskog tijela, statistički model gubitaka, prijenosna karakteristika, ultraširokopojasna tehnologija, vremenski odziv signala, višestazno širenje signala, prostiranje signala unutar ljudskog tijela, prijenos signala ljudskim tijelom,

Contents

CHAPTER 1
Introduction

The Internet-of-Things (IoT) refers to the networks of connected devices and technologies that facilitate communication between them. IoT is one of the fastest growing technological trends of the current decade that continues to transform every aspect of our daily lives. The recent IoT Analytics report[1] “State of IoT - Spring 2023” shows that the number of global IoT connections grew by 18% in 2022 to 14.3 billion active IoT endpoints. In 2023, the global number of connected IoT devices is projected to grow another 16%, to 16 billion active endpoints by the end of the year. IoT device connections are expected to continue to grow for many years to come and by 2030 this number is expected to almost double to 29.42 billion.

In the healthcare sector, IoT is most often used for remote patient monitoring. Connected devices with IoT sensors offer a continuous flow of real-time health data, including vital signs such as heart rate, blood pressure, and glucose levels. This allows patients and doctors to keep track of an individual’s health outside the traditional clinical setting. Furthermore, IoT can enable virtual visits that connect patients to healthcare providers while allowing doctors to quickly access patient data.

A critical component of IoT in healthcare applications is a Wireless Body Area Network (BAN). BAN is a radio communication network in which nodes are located on the surface, inside, or near the human body [1]. As a communication system that operates within the

---

[1] https://iotbusinessnews.com/2023/05/25/34645-state-of-iot-2023-number-of-connected-iot-devices-growing-16-to-16-0-billion-globally-wi-fi-bluetooth-and-cellular-driving-the-market/

human body environment, BAN is optimized for short-range transmission with low-power and high reliability. In addition to healthcare, BAN has applications in military as well as sports. For medical applications, RF-enabled sensor nodes can be worn, ingested, or implanted in the body and used for various medical monitoring, diagnosis and therapeutic applications such as Electrocardiogram (ECG), blood glucose level, insulin pump, smart pills for precision drug delivery, wireless capsule endoscopy, and brain telemetry.

The standardization of BAN communication started with IEEE Task Group 15.6, which presented the first international standard for BAN (IEEE Std 802.15.6) in February 2012. IEEE Std 802.15.6 [1] is a standard for short-range wireless communications to connect small devices placed on the surface, inside or in proximity of the human body. The standard specifies the characteristics of the Physical (PHY) and Medium Access Control (MAC) layers for the implementation of BANs in existing Industrial, Scientific, and Medical (ISM) bands as well as frequency bands approved by the national medical and/or regulatory authorities. The two most popular types of technologies currently being considered for BANs are narrowband ISM and Ultra-Wide Band (UWB) communications. Another technology for BAN applications specified in the IEEE 802.15.6 standard is Human Body Communication (HBC). In the HBC system, the human body is used as a part of a communication channel between the transmitters and receivers placed on the surface of the skin.

Based on the locations of the BAN nodes, there are seven different propagation scenarios (Table 1.1) in which IEEE 802.15.6 applicable devices can operate [2]. The location of the BAN nodes can be classified as follows:

- Implant: inside the human body
- Body surface: in direct contact with the skin or within 2 cm distance
- External: more than 2 cm and up to 5 m from the body surface

Table 1.1: Propagation scenarios for BANs [2]

Scenario	Description	Frequency band
S1	Implant to implant	402-405 MHz
S2	Implant to body surface	402-405 MHz
S3	Implant to external	402-405MHz
S4	Body surface to body surface (LOS)	13.5, 50, 400, 600, 900 MHz 2.4, 3.1-10.6 GHz
S5	Body surface to body surface (NLOS)	13.5, 50, 400, 600, 900 MHz 2.4, 3.1-10.6 GHz
S6	Body surface to external (LOS)	900 MHz 2.4, 3.1-10.6 GHz
S7	Body surface to external (NLOS)	900 MHz 2.4, 3.1-10.6 GHz

In IEEE Standard for BAN, several statistical channel models that describe the mean pathloss and the random variations around this mean have been provided for various communication scenarios. Modeling the radio channel for implant communication is a difficult task. The human body is an extremely challenging environment for the operation of wireless communications systems. Since obtaining physical measurements within the human body for implant communication is impossible, researchers typically use computer simulation techniques and computational models to study the electromagnetic wave propagation.

K. Sayrafian et al. [3] contributed a statistical pathloss model for implant to implant and implant to body surface scenarios using the Medical Implant Communication Services (MICS) frequency spectrum. In their study, they used a 3D virtual reality simulation platform to study electromagnetic propagation from a medical implant. This 3D immersive and visualization platform was developed at the Information Technology Laboratory of National Institute of Standards and Technology (NIST) [4]. The main components of this system include: a three-dimensional human body model, the three-dimensional full-wave electromagnetic field simulator, and implantable and body surface antennas [5, 6, 7].

Antennas were designed considering the influence of the surrounding tissues on its characteristics and exhibited good impedance matching in the MICS frequency band.

The statistical pathloss model can be described by the following equation:

$$\mathrm{PL}(d,f)=\mathrm{PL}(d_0,f)+10n(f)\log_{10}\left(\frac{d}{d_0}\right)+\mathrm{S}(f) \quad d \geq d_0 \tag{1.1}$$

Where d_0 is the reference distance (i.e., 50 mm) and n is the pathloss exponent which depends on the environment of the propagation. S is the random scatter around the mean and represents deviation caused by different receiver and transmitter positions on the body and their antenna gains in different directions, as well as varying dielectric properties of the different organs along the propagation path.

To obtain this pathloss model, simulations were performed for four near-surface and two deep-tissue implant scenarios. The transmitter locations were chosen according to realistic applications in healthcare. For each transmitter location, the received power was calculated, and the results were divided into three sets: in-body to in-body, in-body to body surface, and in-body to out-body propagation sets. Using the pathloss model (1.1), the authors calculated parameters for implant to body surface and implant to implant channel model (Table 1.2).

Table 1.2: Parameters for the statistical pathloss model: a) Implant to body surface channel, b) Implant to implant channel

(a)

Implant to Body Surface	**PL(d0) [dB]**	**n**	**σ_s**
Deep Tissue	47.14	4.26	7.85
Near Surface	49.81	4.22	6.81

(b)

Implant to Implant	**PL(d0) [dB]**	**n**	**σ_s**
Deep Tissue	35.04	6.26	8.18
Near Surface	40.94	4.99	9.05

The frequency band 402–405 MHz has been assigned for Medical Implant Communication Services (MICS) by the Federal Communications Commission (FCC) in the United States. Compared to the ISM and UWB frequencies, MICS band offers better propagation behavior through the human tissues. However, the bandwidth limitations at these frequencies create a limit on the achievable data transmission rates. UWB technology could alleviate such limitations and enable medical applications that requires much higher data rates.

1.1. UWB Technology for Implants Communication

In the past few years, the UWB technology has received considerable attention as a promising candidate for implant communication. The technology offers low power consumption due to simpler transceiver complexity as well as high transmission data rate. However, high attenuation due to the human body tissues at UWB frequencies creates a challenge to establish a reliable communication link with deep-tissue implants. The penetration loss of a communication signal through the human tissues increase with increasing frequency. For this reason, wearable devices in body area networks may use the entire UWB band (3.1 to 10.6 GHz), while in-body devices would be limited to the lower UWB band (i.e., 3.1 to 5.1 GHz).

There are few studies to model the propagation channel of in-body devices that operate within the UWB frequency range. These studies typically use numerical simulations using computational body models [9, 11, 12, 13], or experimental measurements using liquid phantoms [10, 12] or animal meat layers setup [13]. Limited experiments using animals have also been conducted by some authors in the literature [10].

In [9], J. Wang et al. investigated the feasibility of using lower-band UWB to establish a wireless link between an implant located inside the human chest and a receiver on the body surface. Using a disc dipole antenna for the implant, they have derived the channel characteristic based on the frequency-dependent Finite Difference Time Domain (FDTD) methodology. They also investigated the Bit Error Rate (BER) performance using Pulse Position Modulation (PPM) for transmission mechanism. In their simulations, the antenna was placed inside the chest in one of the 20 locations ranging from 0,6 cm to 2 cm away from the body surface. The receiver was located 20 cm away from the body surface right in front of the chest. The body model used in the simulation is the upper half of a human model which was developed based on magnetic resonance imaging data. Their model includes 50 types of tissue with a spatial resolution of 2 mm. From the FDTD-calculated impulse responses, the arrival time and the amplitude were obtained. Using the cumulative distribution of amplitude, the authors reported the amplitude for the 1st path from -62 dB to -53 dB. The focus in this research was the wireless link for cardiac pacemaker application. The modeling effort considers the link between an implant and an off-body receiver.

D. Anzai et al. [10] performed experiments on a liquid phantom as well as a living animal to evaluate the performance of a UWB transmission link. The authors developed an Ultra-Wideband Impulse Radio (UWB-IR) communication system for implant application. The transmission channel was first studied by using a liquid phantom, and then evaluated through experiment with a living animal. For the liquid phantom experiment, the authors reported a pathloss of around 80 dB at a depth of 7 cm from the body surface. In addition to the pathloss measurement, they also evaluated the communication performance of the UWB-IR transceivers. The bit error rate of 10^{-2} was achieved for the distance of around 7 cm with a data rate of 1 Mb/s. The authors then repeated their experiment using a living animal (pig) and placing the transmitter in five different locations in abdomen and chest area of the animal. Despite the large pathloss of more than 80 dB, they concluded that their UWB-IR implant communication system can achieve a BER performance of around 10^{-2} with a data rate of 1 Mb/s up to a distance of 12 cm. The liquid phantom used in this study is a homogeneous environment which is different than the non-homogeneous human body environment, especially for endoscopy applications. Therefore, a more sophisticated computational phantom could be more accurate for this study. Also, the size of receiver antenna is not suitable for practical applications. This directly effects the antenna gain which is reflected in the calculated pathloss.

M. Kanaan et al. in [11] have focused on the non-linearity of the pathloss versus frequency in UWB and attempted to provide mathematical models that capture this relationship. They also investigated frequency dependence of the scattering component of the pathloss. They propose to use these models to identify sub-bands that minimize amplitude distortion at the receiver. The antenna used in this study is an elliptic disc dipole antenna placed inside the chest of a computational 3D human body voxel model. The antenna was placed at a depth d_0 from the body surface. Three different values of d_0 were considered i.e., 4, 5, and 6 cm. Results of their investigation indicate that in order to minimize the amplitude distortion, appropriate sub-bands should be selected based on the depth of the implant and the distance at which the receiving antenna will be located from the body surface. The results are more relevant to cardiac pacemaker or defibrillator applications.

Using different anatomical models and simulation scenarios can lead to variations in statistical propagation models. Also, since in BAN applications, the radio channel includes the transmitting and receiving antennas, antenna characteristics would impact the resulting channel models. Therefore, it is quite challenging to develop a common UWB propagation model for all implant applications.

1.2. UWB Technology for Communication with Ingestible Devices

Capsule Endoscopy (CE) is an innovative and relatively new technology that offers a non-invasive mechanism to examine the gastrointestinal (GI) tract. While traditional endoscopy is often described as painful and uncomfortable for patients, there is also a limited access to the different parts of the digestive system, for example, small intestine [14, 15]. Therefore, CE is gaining more attention, as it can be used to examine the entire gastrointestinal tract without much discomfort and limitations.

Wireless Capsule Endoscopy was first presented in [14]. CE offers a patient-friendly, minimally invasive, and painless investigation of not only the entire small intestine but also other GI parts. It is a cylindrical pill-shaped device with a length of approximately 26 mm and a diameter of 11 mm, equipped with a camera, light source (white LEDs), battery and RF transceiver.

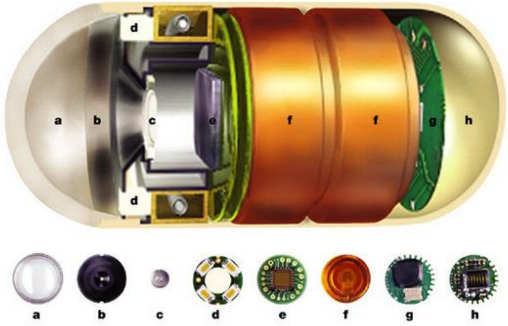

Figure 1.1: The architecture of CE: a) Optical dome, b) Lens holder, c) Lens, d) Illuminating LEDs, e) CMOS imager, f) Battery, g) RF transmission, h) Antenna [14]

After a patient swallows the pill, it travels through the GI tract with the sequence of contraction and relaxation of muscles along the digestive system (i.e., peristalsis wave). The RF signal transmitted from the CE travels through the human body to reach the multiple receiver sensors that are placed on a belt worn by the patient. All transmitted data (i.e., sequence of images captured by the camera) is stored inside a memory module on the belt.

After the procedure, a specialist can look through the collected images in order to investigate potential problems or abnormalities inside the patient's GI tract.

Current commercially available capsules operate at Medical Implant Communication Service (MICS) band (402 to 405 MHz). The bandwidth limitation at these frequencies creates a limit on the transmitted image resolution and the maximum data rate that can be transmitted [17, 18]. The provided images have a maximum resolution of 512 × 512 pixel and around 2 to 6 frames per second [19]. Moreover, the battery lifetime is often a limiting factor for the operation of these capsules. In 16.5% of procedures, the battery cannot support the entire journey of the capsule along the GI tract [20]. The comparison of technical specifications between different commercially available video capsule endoscopy platforms is presented in Table 1.3.

Table 1.3: Comparison of technical specifications between different video capsule endoscopy platforms

Platform	Size	Cameras	LEDs	View angle	Battery life	Frames	Resolution
PillCam SB3	11x26	1	4	156°	8 h	2-6 fps	340 x 340
PillCam Colon	11x36	2	8	172°	10 h	4-35 fps	256 x 256
EndoCapsule	11x26	1	4	160°	12 h	2 fps	512 x 512
CapsoCam Plus	11x30	4	16	360°	15 h	3-5 fps	288 x 206 (x4)
MiroCam	11x26	1	6	170°	11 h	3 fps	320 x 320
OMOM	11x24	1	4	140°	7-9 h	2 fps	640 x 480

The next generation of endoscopy capsules are expected to deliver higher resolution images or even continuous videos as well as more diagnostic and therapeutic functionalities. This in turn requires a higher data rate for the transmission of information from the capsule. Ultra-Wideband (UWB) technology can fulfill the higher data rate requirements while also offering less power consumption which is critical for these capsules. In the upcoming revision of the international standard for Body Area Networks (IEEE Std 802.15.6ma), the unlicensed UWB spectrum from 3.1 GHz to 10.6 GHz is currently being considered for potential application in the ingestible electronics and implants [21].

However, UWB signals experience high attenuation when traveling through body tissues which creates a challenge in establishing a strong communication link. Human body consists of variety of organs and tissues, each with different electrical properties that are also frequency dependent. This dependency might lead to additional distortion in the transmitted signal. The performance of the communication link between the capsule and the on-body receiver is also highly affected by the transmitting and receiving antennas. The dimension of these antennas depends on the operational frequencies and higher frequencies allow smaller antennas to be designed and used for this application. This is especially important for the design of the transmitting antenna, given the physical space limitation in developing CE.

1.2.1. Literature Overview

Understanding the radio frequency (RF) propagation channel in a wireless communication link is essential for efficient transceiver design. However, studying RF propagation channels for implant or ingestible electronics is a challenging task. Performing *in vivo* experiments in a living human to conduct RF signal measurements is practically impossible. Therefore, studies in this area are usually performed using software-based simulations with computational human body models, measurement experiments using liquid phantoms, or *in vivo* experiments on animals [22–28].

In the past several years, there have been few studies in the literature focusing on UWB channel evaluation for capsule endoscopy application. In [22], authors used the finite difference time domain (FDTD) numerical method with an anatomical human body model to find the channel characteristics and investigate feasibility of space diversity to enhance communication performance at UWB frequency from 3.4 to 4.8 GHz. The elliptic disc dipole antenna was designed and used as an on-body receiver placed at five locations in the front of abdomen. The transmitting antenna of the capsule endoscope was a 4 mm line element, moved along the small intestine. The transmitter was placed at 33 different locations with three different polarizations (x, y and z). For each of the five receiver locations on the abdomen, the pathloss exponents and standard deviation of the shadow fading were reported to range from 1.00 dB to 2.07 dB, and 7.1 dB to 8.48 dB respectively. The resulting low pathloss exponents in [22] are likely due to several factors including the simple line element assumed for the capsule antenna, the limited variations of the distances used in the simulations and using free space antenna gains in the computation. Additionally, it was not specified whether the computational model used for the small intestine included sufficient details for the placement of the capsule antenna. The authors conclude by showing the possibility of using the UWB technology to achieve a data-rate of 80 Mbps for capsule endoscopy.

In [23], authors analyze the pathloss, specific absorption rate (SAR), and temperature variation of the tissues inside the human body caused by an IR-UWB-based capsule endoscope inside the abdomen. Since their primary objective is the electromagnetic power absorption and thermal effects caused by in-body propagation of the wireless signal from the capsule, the pathloss calculation is more focused on in-body propagation channel. To characterize this channel, the authors used a voxel-based human body model and computed the pathloss based on time-varying Poynting vector at points that lie within the tissue medium between the capsule and body surface. For this research, an UWB antenna with dimensions of 11.85 x 9 x 1.27 mm operating at 3.5 to 4.5 GHz frequency was designed. Based on observation from their simulations, the authors state that pathloss at the surface of the body varies from 80 to 100 dB, which they also confirmed using experimental validation. For experimental setup, they used porcine abdominal tissue samples. However, they note the possible dependency of this value on the frequency as well as the position of the capsule inside the GI tract. The resulting pathloss model for the in-body channel does not include the effect of the on-body receiver which is normally part of the CE communication channel.

Authors in [24] developed an UWB antenna based on polarization diversity technique for implant applications. To develop an implant antenna, authors combined two planar loop antennas with different direction to make a diversity antenna. They evaluated the performance of the antenna through computer simulation, liquid phantom as well as experiment with a living animal. Considering the frequency range 3.4 GHz to 4.8 GHz, the authors report the average pathloss between the implant and on-body antennas with distances ranging from 2 cm to 12 cm. Based on the measurement data from 6 sample points inside a liquid phantom and 8 sample points inside a female pig, they conclude that using polarization diversity for the implant antenna can improve the performance of the UWB communication link. The measurement experiments have limited number of sample points and only one receiver antenna at fixed position on the body surface.

In [25, 26], authors present a comparative pathloss study for capsule endoscopy in the frequency range 3.1 GHz to 5.1 GHz. Simulations using a simple computational model, liquid phantom experiment and *in vivo* measurements with a living porcine were conducted to do the study. The UWB antennas used in simulations and experiments are patch antennas with a quasi-omnidirectional radiation pattern. Their dimensions are 2.3 cm × 2 cm for in-body antenna and 5 cm × 4.4 cm for on-body antenna. For phantom experiment, they used multi-layer phantom container made of polyethylene terephthalate (PET) material and filled with two layers of muscle and fat liquid phantoms with a divider sheet (also made of PET) between them. A distance range of approximately 3 cm to 8 cm was considered for evaluation of the pathloss between the capsule antenna and the on-body receiver. The 8 cm limitation on distance is primarily due to the noise floor of the vector network analyzer used for signal measurements. For a logarithmic pathloss model, the pathloss exponents and standard deviations of the shadowing component were reported to range from 5.3 dB to 10.3 dB, and 3.6 dB to 28.1 dB across simulations, liquid phantom, and *in vivo* measurements, respectively. In-body antenna used for simulations and measurements has much larger dimensions than the current commercially available endoscopic capsule, which is not practical. In addition, in software simulations antennas are always aligned which is not a realistic scenario. Since antennas are part of a channel for in-body communications, the orientation and size of antennas will affect the pathloss values.

In [27, 28], authors studied the propagation channel between an endoscope capsule antenna and a directional on-body antenna using a voxel-based computational body model for the frequency range 3.75 GHz to 4.25 GHz. The capsule antenna was placed in three different areas of the small intestine and two on-body locations were considered for their evaluation. The authors concluded that the channel characteristics strongly depend on the locations of the antennas inside the small intestine and on the abdomen surface. In addition, they showed that the antenna radiation pattern and capsule orientation have a strong impact on the received signal strength. Their research was expanded into a comprehensive study of radio channels for capsule endoscopy application utilizing multiple antenna system with 7 on-body receivers and using an anatomically realistic human voxel model [29]. They studied frequency and time domain characteristics of the channels for different capsule locations and orientations and provided statistical analysis of the channel data, including path loss and root mean square (RMS) delay spread.

As can be concluded from this brief overview, using different anatomical or computational body models, simulation or experiment scenarios and capsule or on-body antennas often leads to noticeable differences in the resulting statistical propagation models for capsule endoscopy. For in-body or on-body propagation studies, the transmitter and receiver antenna characteristics are part of the channel. This is because antenna de-embedding for wireless wearables, implants and ingestible electronics is nearly impossible, and using realistic and practical antennas for propagation study in these applications becomes important. For capsule endoscopy, the size of the transmitting antennas used in some of the studies in the literature is larger than the current commercially available capsules (i.e., 11 mm × 26 mm). Antenna size has a direct impact on the realized gain and efficiency of the antenna, which is reflected in the resulting pathloss. Therefore, it is more accurate to use antennas with practical sizes during virtual or physical measurements. Additionally, different antenna orientations are typically not considered as part of the simulation or physical experiment scenarios to measure the pathloss. The orientation of the capsule antenna continually changes as the capsule traverses through the GI tract. Due to its non-isotropic radiation pattern, the antenna orientation will have a considerable impact on the experienced pathloss. Therefore, this impact should be captured in a practical statistical pathloss model for this application.

1.3. Human Body Communication

Human Body Communication (HBC) is another technology defined within the IEEE 802.15.6 standard. In HBC, the human body is used as a part of a communication channel between a transmitter and receiver placed on the surface of the skin. In literature, HBC is also referred to as body channel communications (BCC) or intrabody communication (IBC).

The HBC channel is typically characterized for the frequency range between 100 kHz and 100 MHz. For frequencies lower than 100 kHz, human body is susceptible to EM interference, while for frequencies higher than 100 MHz, human body acts as an antenna since the carrier wavelength reaches the length of human body parts [30]. Nevertheless, low frequencies also have advantages such as simpler design, lower power consumption, physical layer safety and security, etc.

Two main human body communication methods are capacitive and galvanic signal coupling. In capacitive signal coupling, the change of the voltage between the transmitter signal and reference electrodes leads to the change in the electric field between the receiver electrodes. In the presence of a weak electric field the human body acts as a signal guide and couples the signal capacitively, while the return path from the receiver reference electrode to the transmitter receiver electrode is provided through the environment. In a galvanic signal coupling, the signal is controlled by a current flow through the body, and all four electrodes must be in direct contact to the body. Two coupler electrodes induce currents into the human tissue and two detector electrodes sense the potential differences.

In 1995 Zimmerman presented a concept of Personal Area Networks (PAN), a wireless system that allows devices on and around the human body to exchange digital information. He also developed the first prototype system using capacitive signal coupling [31]. The prototype used a signal with an amplitude of 30 V, 330 kHz carrier frequency, and on-off keying (OOK) modulation. Data rate of 2400 bps and a power consumption of 1.5 mW were achieved. The galvanic coupling HBC was firstly reported in 1997 by the Japanese researchers Handa et al. [32]. The ECG signal from the chest, coupled into human body by electrodes, was detected by a pair of receiving electrodes on the wrist. The transmitting and receiving electrodes were in direct contact with the body, resulting in galvanic coupling signal transmission. In 1998, Lindsey et al. [33] tested the galvanic coupling HBC between an implantable device and an on-body receivers. Two platinum electrodes were used to inject sinusoidal currents with frequencies of 2–160 kHz and amplitudes of 1–3mA into the leg of a human cadaver. EMG electrodes on the surface of the leg were used to detect the voltage differences.

Since then, there have been different studies to investigate the mechanism of sending and receiving data through the human body and to model the HBC channel. Methods used for channel modeling are simple circuit model, finite element method (FEM), finite difference time domain method (FDTD), or analytical electromagnetic model [30–45].

First circuit model was first proposed by Zimmerman [31, 34]. The body was modeled as a perfect conductor and capacitors were used to model electric fields between the HBC system and the environment. The return signal path was closed through the environment ground also using capacitors. Callejon et all developed the circuit model of skin for both capacitive coupling and galvanic coupling [35, 36]. They reported that attenuation increased up to 200 kHz and remained approximately constant for higher frequencies in galvanic coupling HBC. For capacitive HBC, a bandpass profile was observed within 1~100MHz. They determined that the optimal frequency range was 20–60 kHz for the galvanic coupling and 60–70 MHz for the capacitive coupling.

Wegmueller [37, 38] developed a simple four-terminal circuit model with six body tissue impedances and four electrode-skin impedances for low frequency (<1 MHz) galvanic coupling HBC. They also developed a 3-D FEM model of a human arm consisting of five cylinders representing skin, fat, muscle, cortical bone, and bone marrow layers [39]. Numerical simulation for specific body parts using FE cylindrical model were validated by *in vivo* measurements on 20 subjects. The measurements were performed for a short-range communication path along the extremities for frequency from 10 kHz to 1 MHz. Different sizes of Blue Sensor electrodes were also compared. The results showed that the size of the receiver electrode did not have an influence on the attenuation in simulation and experimental measurements, while the larger transmitter electrode sizes were found to have lower attenuation.

J. Bae et al. [40] presented the theoretical background study to unify and explain all mechanisms of the electrical signal transmission through the human body. Based on the physical and electromagnetic theory, a general Body Channel Communication (BCC) model was developed to analyze the pathloss according to frequency and distance for on-body transmission. The distances between the Tx and Rx were varied from 10 cm to 130 cm by changing the Tx locations from the left arm to the right arm across the chest with 5 cm interval. The highest reported pathloss in 10-100 MHz frequency range was -10, -20 and -35 dB for 10, 40 and 120 cm distance respectively.

Xu et al. [41] proposed a circuit coupled FEM model for capacitive coupling HBC. The human body was considered as a circuit of lumped resistors paralleled with lumped capacitors. The FEM model is then verified by experimental measurements. Both the measurements and simulations are conducted in the 1–180 MHz frequency range. Their results showed that channel gain has a high-pass profile. Below 4 MHz, the channel gain is almost independent of the body path length and increases by 20 dB/dec. This is because the channel is dominated by the capacitive return path. Beyond 4 MHz, longer body path leads to higher attenuation due to the higher impedance in the body path and the larger leakage from the body to the external ground.

Z. Lucev Vasic [42, 43] explored the characteristics of the human body as a part of the capacitive intra-body communication system. Measurements of the human body transmission characteristics were performed on several test subjects, with and without environment influence, using multiple electrode types, several ways of connecting the electrodes to the body, and using few measurement setups (battery- and power-line-powered network analyzers, with and without decoupling). All transmission amplitude characteristics shared the same trend: increase 20 dB/decade up to around 45 MHz, steep decrease up to 85 MHz, and above 90 MHz the gain increased again.

J. Park et al. [44] presented a paper with contribution to estimate the pathloss of capacitive HBC systems. They concluded that measurements of pathloss in capacitive HBC systems strongly depend on instrumentation configurations. Most prior work utilizes large, grounded instruments to perform pathloss measurements, resulting in overly optimistic pathloss estimates for wearable HBC devices. In this paper, small battery-powered transmitter and receiver devices were implemented to measure pathloss under realistic assumptions. The simulations using hybrid electrostatic circuit – three-dimensional (3-D) finite element method (FEM) model for pathloss simulations, match measurement results within 2.5 dB.

From the studies mentioned above, the HBC channel gain generally has a bandpass profile. However, there are some inconsistencies in the results provided in the literature. These are likely due to the methodology and experimental conditions, e.g., type and size of electrodes, different grounded instruments, electrode-impedance matching, body position and movements of the subject, etc. [36, 42, 43]. Therefore, a comprehensive study to provide standardized design and methods for HBC would be beneficial. Moreover, considering that HBC can provide high data-rate communications, it is valuable to also investigate whether HBC could be used for implants or ingestible applications such as capsule endoscopy.

Most of the investigations on implant HBC are focused on galvanic coupling type [46–49]. Nevertheless, the signal attenuation in galvanic coupling HBC is more sensitive to channel length and electrodes placement, and it has lower data rates due to the lower operated frequency [50]. On the other hand, capacitive coupling HBC device seems impractical due to the electrode configuration. One electrode (signal electrode) is implanted into human body, while ground electrode should be exposed to air. J. Li et al. investigated the channel characteristics between the human brain and body surface with a ground electrode exposed to air [51]. Their study was performed using FDTD simulations and experimental measurements on a pig. The signal return path was shortened in both simulations and measurements, and results showed low pass profile.

In [52] the authors derived the transfer function of the implant HBC based on capacitive coupling and investigated its characteristics in measurements and simulations. The implant capacitive electrode contains a signal electrode made of a metal stick and a ground electrode made of a metal cylindrical casing. The signal electrode is in direct contact with the human tissue, while insulating shell is used to insulate the ground electrode from both the tissue and the signal electrode. More recently, same authors developed a 3-D finite element method model of the human arm and compared results obtained using fully implanted capacitive and galvanic electrodes, [53]. They also performed empirical verification measurements using porcine tissue.

Lucev-Vasic et al [54] presented a preliminary characterization of in-body to on-body capacitive HBC channel under implantable-like conditions. The communication link was emulated by placing the transmitter under the armpit and taking different body positions, while covering transmitter electrodes with tissue. EEG electrode was affixed to the bottom side of a PCB board and used as a transmitter signal electrode. Copper side of a PCB was used as a transmitter ground electrode and was covered in hot glue to ensure insulation from signal electrode and body tissue. Measurements emulating in-body to on-body HBC channels transmission characteristics were performed in the frequency range between 100 kHz and 100 MHz. Same team recently presented characterization of implantable capacitive HBC in-body to on-body channel using liquid phantom measurements [55]. Measurements were performed using proprietary developed battery-powered devices (transmitter and receiver) for both in-body to on-body and on-body to in-body scenarios. The results highlighted the importance of minimizing the bandpass profile effect caused by the long cables. Also, insulating the ground electrode affected the measured attenuation by about 6 dBm.

Authors in [56–58] developed a capsule endoscope system with four VGA-resolution cameras offering 360° field of view. Communication between the capsule and on-body receiver was established through capacitive coupling via two gold-coated signal electrodes on the transmitter. To increase overall coupling the authors proposed increasing the size of metallic ground plane integrated in the receiver. Intrabody communication performance was tested with measurements using human tissue phantom and pig small intestine for 10 MHz to 200 MHz frequency band. Authors also tested location accuracy and presented results demonstrated less than 1 cm localization error on average.

1.4. Contributions and Thesis Outline

Comprehensive study of wireless communication for ingestible electronics is a very challenging task. From the limited number of studies on this topic in the literature, it can be observed that using different models, simulation or experiment scenarios, and antennas often lead to noticeable variations in the resulting statistical channel models for capsule endoscopy. As common in almost all in-body or on-body propagation studies, the transmitter and receiver antenna characteristics will become part of the propagation channel. Each application or use-case could necessitate a different type of antenna, and measurement (or simulation) scenarios. For these reasons, it is conjectured that channel models for ingestible applications such as CE may not necessarily be the same as implant applications operating at UWB frequencies.

In this dissertation, two communication technologies that can be used for next generation wireless capsule endoscopy are studied. These technologies are Ultra-Wideband (UWB) and

Human Body Communication (HBC). To initiate the study on using UWB, a flexible and interactive immersive platform containing an enhanced 3D body model and detailed antennas has been developed. The platform can emulate the communication link between a CE and several on-body sensors. The orientation of the capsule antenna continually changes with respect to the on-body receiver as the capsule traverses the complex path along the GI tract. This is especially the case for the small intestine. The developed platform is also extended with additional tools that enable orientation and localization of a CE in the small intestine. Another low-complexity technology that could be promising for CE application is HBC. HBC uses electric field communication to connect two electrodes that are in contact with the human body. Several recent experimental studies of HBC (with differing results) are available in the literature for wearable sensors; however, there is a lack of agreement between the reported results. Also, potential use of this technology for implants (and specifically capsule endoscopy application) has not been fully investigated. Therefore, a simulation platform that can emulate an HBC link for implant, as well as wearable sensors has been developed in this study.

The scientific contributions of this thesis are summarized as follows:

- A 3D immersive platform to study wireless channel in Capsule Endoscopy
- UWB channel characterization in Capsule Endoscopy
    - An UWB statistical pathloss model for wireless Capsule Endoscopy inside the small intestine
    - A study of the time-domain response of an UWB communication channel in capsule endoscopy
- Capsule orientation estimation inside the small intestine
    - Algorithms for orientation estimation of a wireless Capsule Endoscopy using signal strength-based methodology
- A FEM-based parametric computational platform to study Human Body Communication channel and the impact of electrodes size and location
    - Feasibility of using the Human Body Communication technology for Capsule Endoscopy application

1.4.1. Outline of the thesis

In Chapter 1 of the doctoral thesis (“Introduction”) a short overview of the wireless body area networks is given. Capsule endoscopy technology and its current communication limitations are explained. A comprehensive literature review focusing on the Ultra-Wideband (UWB) and Human Body Communication (HBC) technologies and channel characterization is presented. The chapter is concluded with goals and scientific contributions, and outline of the thesis.

In Chapter 2 (“Immersive platform”) the development of a novel 3D immersive platform to emulate radio frequency (RF) propagation between a capsule endoscope and several on-body receivers is explained. The platform allows for an in-depth study of the wireless propagation channel for implants and ingestible electronics at UWB frequencies. Key components of the platform i.e., the high-resolution GI tract model and capsule/on-body antennas are described. A methodology for judicious placement of the capsule antenna inside the small intestine to achieve the desirable statistical distance distribution is defined. Finally, a proper set of simulation scenarios for radio wave propagation and communication channel measurements is identified.

Channel pathloss model and details on calculations of the channel model parameters are provided in Chapter 3 (“UWB Channel Characterization in Capsule Endoscopy”). A statistical pathloss model including a fading component that more effectively captures the impact of various body tissues as well as the antenna orientation for the 3.1 GHz to 4.1 GHz frequency range is obtained. The obtained pathloss was contributed to the IEEE revision of the 802.15.6 standard and was accepted as a standard channel model document for Capsule Endoscopy use-case. Partial model verification and the potential impact of the measurement points distribution on the extracted pathloss exponent is also presented. Using inverse Fast Fourier transform, time domain responses of the channels are also obtained and studied in more detail.

In Chapter 4 (“Capsule Orientation Estimation”) methodologies that can assist in estimating the position or orientation of a capsule endoscope are presented and a short overview of previous studies in the literature is given. A preliminary study of capsule orientation estimation by observing the received signal strength (RSS) is conducted. Two methodologies, i.e., complex cross-correlation and Minkowski distance, were used to assess capsule orientation estimation with respect to a reference position. The study was performed within the Ultra-Wide Band frequency range.

Human Body Communication (“HBC”) technology, another candidate for the capsule endoscopy application, is explained in Chapter 5 (“Human Body Communication”). A FEM-based parametric simulation platform including a full 3D computational human body model is developed. The parameters of the model are all design variables that were adjusted to emulate several specific measurement scenarios. The developed customizable computational platform allows comprehensive study of the HBC channel by considering different electrode sizes and placements on the surface and inside the human body.

Finally, in the discussion and conclusion chapter of the thesis (Chapter 6), key research results and the original scientific contributions of the thesis were summarized and the directions for further research were determined.

CHAPTER 2
Immersive Platform

Since conducting physical experiments is nearly impossible, one of the challenges in studying radio frequency (RF) propagation for CE is a platform that can be used to evaluate potential technologies. There are three main approaches to conduct such studies in WBAN: simulations using computational body models, experimental measurements with phantoms, and *in vivo* experiments. Each of these approaches has limitations and shortcomings.

Liquid phantoms are aqueous solutions that mimic electromagnetic properties of human tissues. Liquid phantom can emulate a single or multi-layer dielectric environment. The material at each layer homogeneously models the dielectric properties of a specific tissue. However, the human body is a non-homogenous complex environment with multiple different tissues, each having a wide range of frequency-dependent dielectric properties. Nevertheless, multi-layer liquid phantom may offer a good representation of the channel for wireless implant applications were the implant and receiver are both at fixed position and properties of the tissue layers between them are known. However, for CE applications, the RF signal transmitted from the capsule will experience different composition of the body tissues and organs as the capsule moves through the GI tract.

In vivo experiments, performed in hospitals or laboratories on a living animal, can better approximate the complex human body environment. However, flexible placement of the transmitter antenna inside the living animal body is a challenging task. Typically, very few antenna positions can be considered inside the animal's body, leading to a small number of measurement samples with a limited distance range. Moreover, there is also a radio signal leakage through the connecting cables, as well as possible errors in the estimated distance between the capsule transmitter antenna and on-body receivers during pathloss measurements.

Compared to liquid phantoms, computational body models offer better approximation of the non-homogeneous and diverse dielectric environment in CE application. However, the high level of details and resolution of computational body models increases the complexity and computational resources needed to perform simulations. In order to simplify the simulations and achieve manageable runtime, most of the studies in literature use a partial computational body model. They usually focus on a specific area like the abdomen and reduce the number of organs involved. This simplification limits the ability to accurately define scenarios for placing the capsule inside the specific segment of the GI tract. Therefore, having a more detailed model that includes the internal structure and surfaces of the digestive tract becomes necessary to accurately characterize the continuous path of the capsule. Moreover, it will also help to better define capsule antenna positions and perform more accurate channel measurements.

For this study, a novel 3D immersive system to emulate RF propagation between a capsule endoscope and several on-body antennas has been developed at the Information Technology Laboratory of the National Institute of Standards & Technology (NIST) [3, 4, 5]. The system, as presented on Figure 2.1, has following components:

- A 3D high resolution human body model with enhanced, high-resolution GI tract model
- A full-wave electromagnetic field simulator (ANSYS Electronics desktop simulation software)
- Validated models of the capsule and on-body antennas
- A 3D immersive and visualization platform

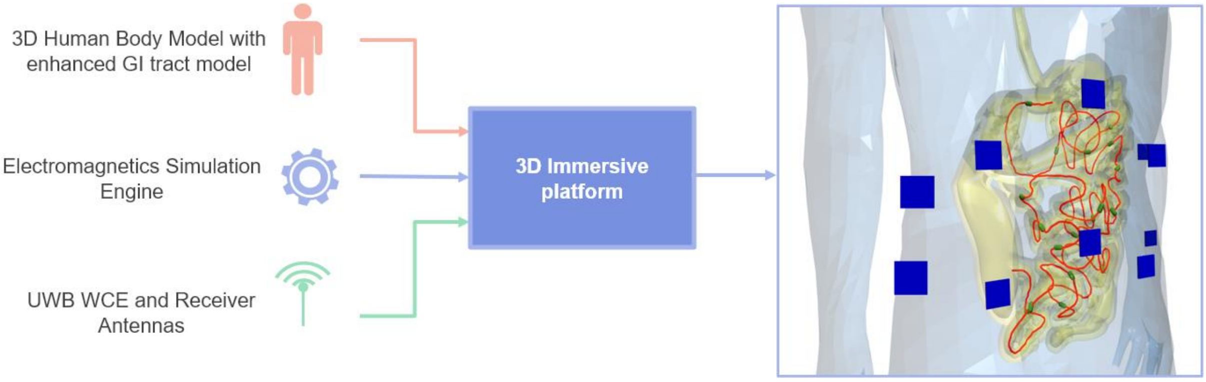

Figure 2.1: 3D immersive platform

2.1. Computational Human Body Model

A high-resolution, enhanced GI tract model, including internal tubes and surfaces without self-intersections or other “non-manifold” features, has been developed and integrated with a 3D computational human body model of an adult male (Figure 2.2). The 3D computational body model used in this system has a resolution of 2 mm and includes complex, frequency-dependent dielectric properties of 300+ parts of a male human body. Muscle-like properties were assigned for body exterior and Debye model was used for frequency dependent dielectric properties of human tissues. These dielectric properties are user-definable in case custom modifications or changes are desired. Table with dielectric properties at 3.6 GHz is shown below.

Table 2.1: Dielectric properties of human tissues at 3.6 GHz

Tissue	***Permitivity (ε_r)***	***Conductivity (σ)***
Stomach	60.3	3.38
Small Intestine	52.3	4.21
Large Intestine	52	3.06
Muscle	51.3	2.65
Fat	5.16	0.161
Skin	36.9	2.09

The electromagnetic simulation engine in this system enables the user to calculate a variety of different electromagnetic quantities; examples of which are scattering parameters, electric field, Poynting vectors, Specific Absorption Rate (SAR), etc.

Validated models of practical UWB antennas have also been incorporated in the computational system to accurately characterize the UWB wireless link between the capsule and the on-body receivers.

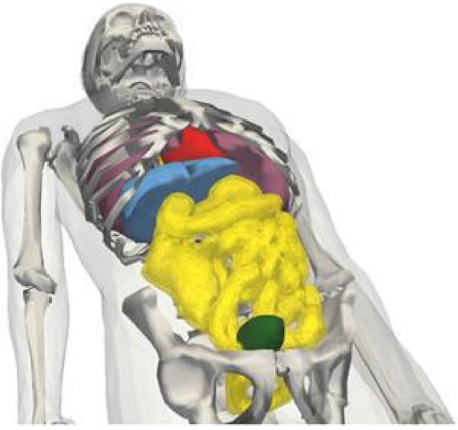

Figure 2.2: The 3D human body model with enhanced GI tract

The 3D immersive platform assists a user to visualize and interact with the data. The platform includes a visual display consisting of three large screens, stereoscopic glasses that are motion-tracked, and an input device that is also motion-tracked. The three large video projection screens are used as a single 3D stereo display. The 3D scene is updated for the position of the stereo glasses given by the motion tracker. This enables the immersive platform to present a virtual 3D world within which the user can move and interact with a virtual object. The virtual object in this study is the 3D human body model, as observed in Figure 2.3, and a hand-held motion-tracked wand is the main interaction device. This immersive system effectively captures the complexity of the propagation environment around the capsule as it travels through the GI tract; and therefore, has been used to study the UWB channel characteristics for capsule endoscopy.

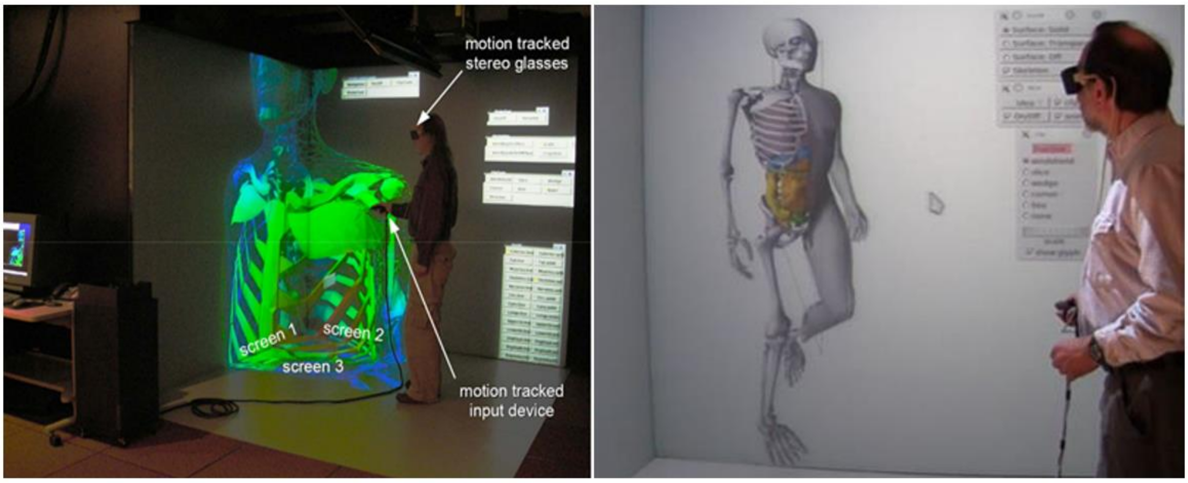

Figure 2.3: NIST immersive visualization environment

2.2. Antennas

2.2.1. In-body Antenna

Antenna is one of the key components of wireless body area network both for on-body and in-body communication systems. The environment for an implant antenna is completely different from the usual free space communications, making the antenna design a challenging task. To achieve good performances for WBAN applications, antenna must be designed considering the influence of the body tissues on its characteristics. Also, since de-embedding of the antenna gain pattern from the communication channel becomes impossible for in-body or on-body applications, using a realistic and practical antenna for channel characterization becomes extremely important.

The capsule endoscopy antenna is a single metallic layer planar antenna designed for UWB transmission from 3.1 GHz to 10.6 GHz. The antenna is printed on a Rogers1 RT Duroid 6100™ substrate with dielectric constant of 10.2 and thickness of 0.8 mm. The antenna dimensions are 8.4 mm x 6 mm x 1.036 mm (Figure 2.4), which fits inside typical CE pills currently available in the market. The diameter and length of the current commercially available pills are greater than 9 mm and 23 mm respectively [60].

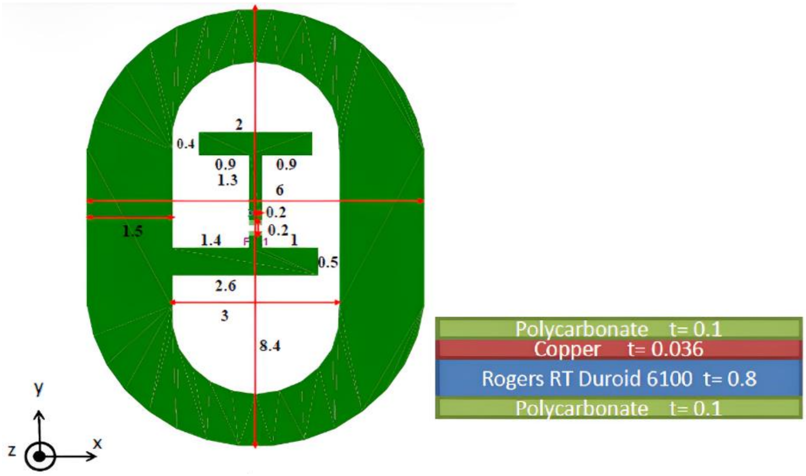

(a) *(b)*

Figure 2.4: Configuration and dimension (in mm) of the CE antenna a) top view b) side view [61]

The antenna has been designed and evaluated using the tissue layers [61]. To ensure applicability of the antenna throughout the entire GI tract, three scenarios (stomach, small and large intestines), were considered. The return-loss of the antenna for all three environments is shown in Figure 2.5. These results show the effectiveness of this antenna as the capsule travels through the GI tract.

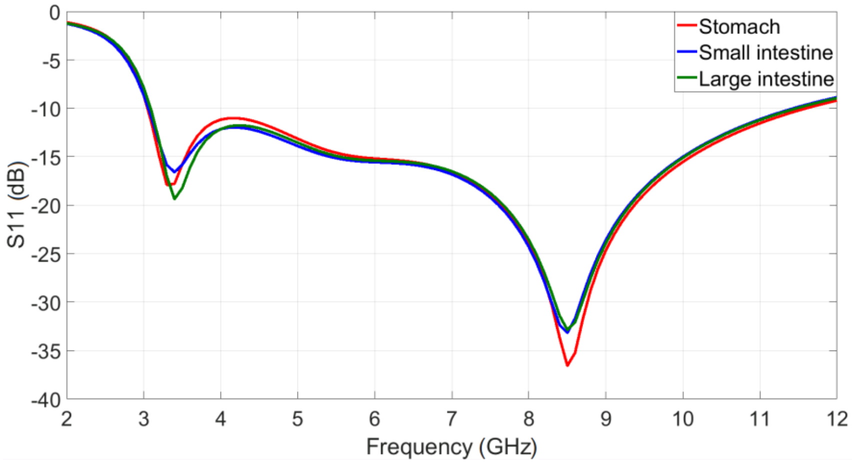

Figure 2.5: S_{11} of the capsule UWB antenna using customized layered tissue models for stomach (red), small intestine (blue) and large intestine (green)

To better investigate the influence of the inhomogeneous environment surrounding the antenna, the return-loss performance of the antenna when located inside the stomach, small and large intestines of the computational human body model has also been verified. The results show close agreement between the S_{11} of the simplified layered models and the antenna located inside the GI tract of the computational human body (Figure 2.6).

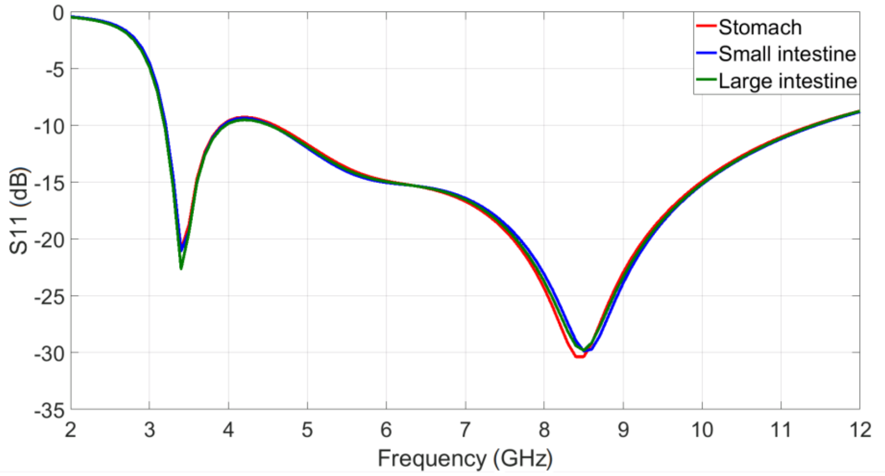

Figure 2.6: S_{11} of the capsule UWB antenna inside the GI tract of the computational human body model: stomach (red), small intestine (blue), and large intestine (green)

The 3D in body radiation pattern of this antenna showed that the antenna has a null. As it will be shown in Chapter 4, this observation has been used to do a preliminary study on orientation estimation of the capsule.

2.2.2. On-body Antenna

The receiving on-body antenna is an L-loop antenna that has been designed to operate in the lower band UWB (i.e., frequency range of 3.1–5.1 GHz). As shown in Figure 2.7, the size of the surface antenna is 24 mm x 25 mm x 1 mm. In order to minimize the effect of the human body on the antenna characteristics, antenna elements should be separated from the skin. Therefore, a RH-5 dielectric substrate with a thickness of 14 mm was added. The relative permittivity of RH-5 is identical to air. This substrate will not affect the antenna parameters and the same level of Voltage Standing Wave Ratio (VSWR) as in free space can be achieved when the antenna is placed on the body surface near the abdomen. Detailed study of this surface antenna can be found in [62].

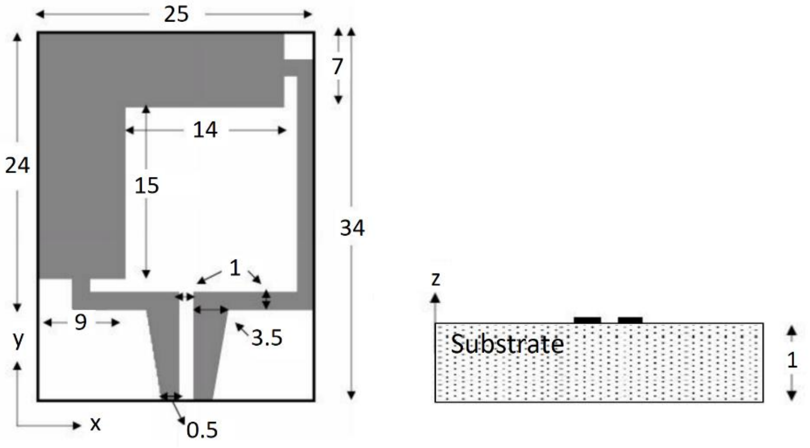

(a) *(b)*

Figure 2.7: Configuration and dimensions (in mm) of the UWB L-loop on-body antenna a) top view, b) side view [63]

The on-body antenna was also evaluated with the computational body model. The S_{11} and VSWR of the antenna, shown in Figure 2.8, are obtained by placing it on the abdomen area of the body model. As observed, the antenna shows good performance for the frequency range 3.1 GHz to 4.1 GHz. A slight frequency shift in VSWR was observed when comparing the antenna performance to the original layered tissue model it was designed with. However, such small discrepancies are to be expected since on-body antennas are often sensitive to their exact distance from the body surface. The curvature on the computational body model will cause some variations in antenna distance compared to the simple layered tissue model that was used during the antenna design process. However, for the frequency range 3.1 GHz to 4.1 GHz, all antenna placements on the body surface covering the abdomen showed very good reflection coefficient response.

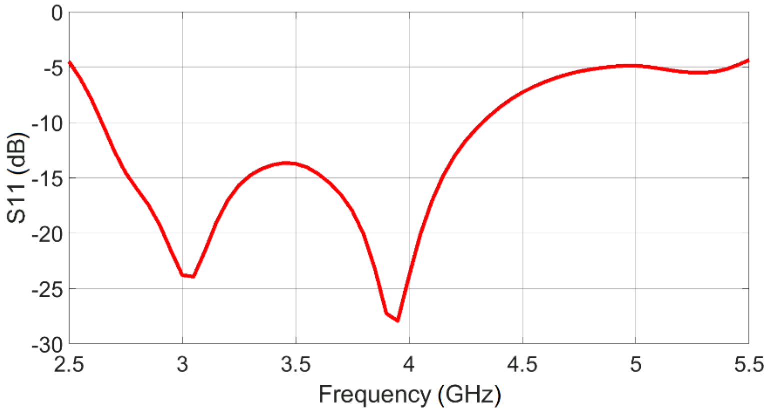

(a)

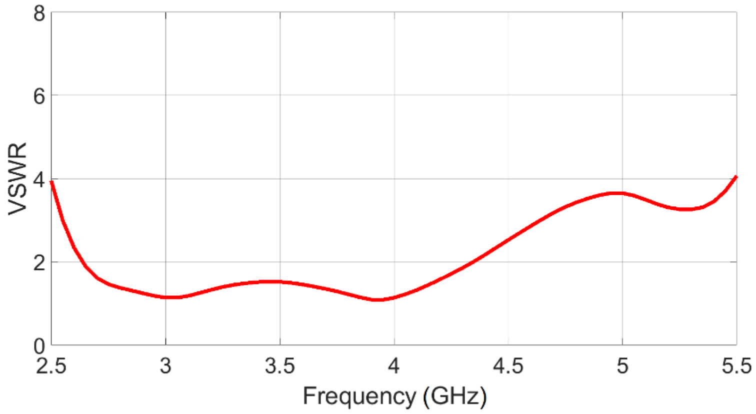

(b)

Figure 2.8: (a) S_{11} and (b) VSWR of the on-body antenna with the computational body model

2.3. Using the Immersive System to Study Wireless Channel in CE

During a Capsule Endoscopy procedure, a patient wears a belt across the abdomen with multiple embedded receivers. For this study, positions of the receivers were approximately selected based on the sensor's location used in the small bowel PillCam Capsule Endoscopy procedure [64]. The blue squares in Figure 2.9 show the locations of the on-body antennas during virtual experiments. A total of 10 receivers, sufficiently apart from each other and spread across the abdomen surface, have been used. With these receivers, each capsule antenna location results in 10 independent propagation channels.

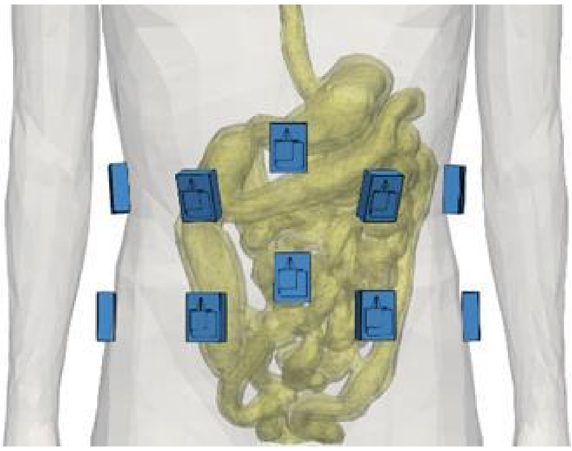

Figure 2.9: Locations of the on-body receivers (blue squares) covering the abdomen

To have an accurate evaluation of the propagation channel, it is important to carefully choose the locations of the capsule inside the GI tract. The 3D centerline that passes through the GI tract has been calculated to assist with placing the capsule antenna inside the small intestine. This centerline (shown with red colored line in Figure 2.10) is the average of all possible paths that go through the small intestine. On average, this line can be considered as the forward progression path of the capsule. Several sample antenna positions on this line have been selected to conduct electromagnetic simulations and obtain channel parameters for pathloss modeling [65].

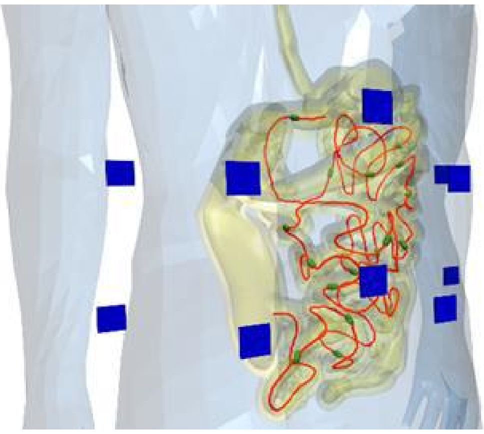

Figure 2.10: Locations of the on-body receivers (blue squares) and the centerline passing through the small intestine (red line)

Using a high-performance computing server with 64 cores and 4 TB of high-speed memory, the forward transmission coefficient of the channel has been obtained through simulations. Simulations were conducted for the frequency range 3.1 GHz to 4.1 GHz with 20 MHz step size. Computational simulation took close to 24 hours for each sample capsule position. Therefore, some simplifications were applied to the high-resolution computational body model to reduce the running time of each simulation. For the final set of simulations only the torso of the human body model along with all the organs surrounding the GI tract was used. It has been verified that other body parts, removed from the model, do not have any noticeable impact on the UWB propagation channel.

To conduct statistical analysis of the measurement data, judicious selection of the best candidate positions for the capsule antenna inside the small intestine is necessary. In addition to keeping the total simulation runtime manageable, this will lead to a balanced transmitter-receiver distance distribution. As will be explained in the next section, placing the antenna uniformly spaced along the GI centerline does not lead to an acceptable set of candidate positions. Therefore, a methodology has to be developed to achieve the desirable distance distribution.

2.3.1. Capsule Position Selection Using an Interactive Tool at the Immersive Platform

To obtain a statistical pathloss model for the communication link between the capsule and on-body receivers, a set of sample capsule positions inside the small intestine is needed. These capsule positions will define a set of simulation scenarios for radio wave propagation and signal measurements. The first approach that comes to mind is to choose uniformly spaced locations along the tract centerline as sample positions. However, due to the complex and intertwined nature of the GI tract, using evenly spaced sample positions causes situations where the distances between the capsule and on-body receivers are heavily concentrated within certain ranges. And furthermore, there are not enough samples in other distance ranges. This lack of balance in distance representation will have a negative effect on the accuracy of the statistical analysis required for pathloss modeling. The impact of a measurement points distribution for statistical modeling has been shown in additional study [66] and will be explained in more details in the next chapter.

The methodology to find the best positions of the capsule antenna involves developing several interactive tools that can be used in the immersive platform described earlier. These locations must cover the entire area of the small intestine to reflect comprehensive channel measurements. It is also important to have a sufficient number of measurement samples that are evenly distributed across the entire range of transmitter-receiver distances. Meeting these conditions will ensure a full representation of the small intestine environment and enable to obtain more accurate parameters in the resulting statistical pathloss model. Figure 2.11 shows the inner GI tract with an example set of capsule positions. Capsules (shown in green) are placed and oriented along the centerline of the small intestine to better reflect the impact of the radiation pattern of the transmitting antenna on the pathloss measurement. D_1, d_2, d_3 are examples of the distance of one sample capsule position to three on-body receivers. To select the best sample locations for the capsule antenna inside the small intestine while satisfying the conditions mentioned before, an interactive tool in the NIST immersive platform has been developed. This interactive tool consists of several different modules, summarized in the block diagram on Figure 2.13, with the following functions:

1) INITIAL POSITION SELECTION

To initiate the selection process, an algorithm has been developed to compute positions along the small intestine centerline that are specific distance away from the on-body receivers. The distances were chosen to be from 5 cm to 25 cm away from a receiver in increments of 2 cm.

2) SELECTING POSITIONS ALONG THE CENTERLINE

The NIST immersive platform supports interactive probing and picking in a 3D scene. Using this capability, the user can select positions along the small intestine centerline. However, the chosen position has to be a specific distance from the receivers based on the precomputed positions in step 1. Therefore, a K-nearest-neighbor search using CGAL [67] was used. This algorithm takes the user-chosen position and then finds the closest matching precomputed position.

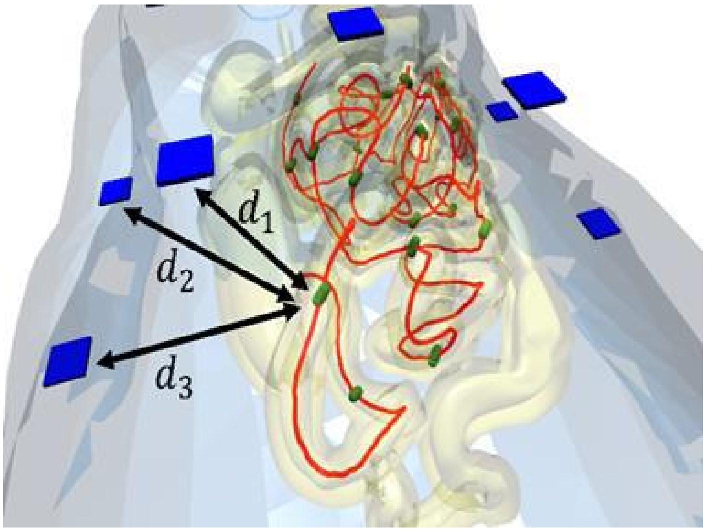

Figure 2.11: Sample capsule position along the small intestine centerline and its distance from the on-body receivers

3) HISTOGRAM OF DISTANCES

For each selected point, the visualization system calculated distances to each of the receivers and presents them within a histogram (Figure 2.12). This allows to instantly see if the selected sample points are uniformly spread across the range of interest and if further adjustments (addition or subtraction of sample points) are needed.

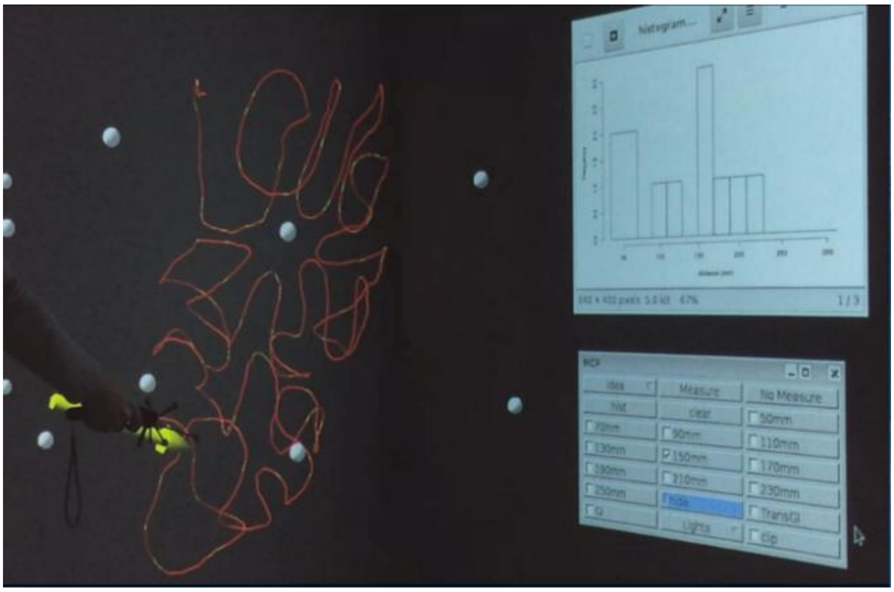

Figure 2.12: Interactive tool inside the NIST 3D immersive platform

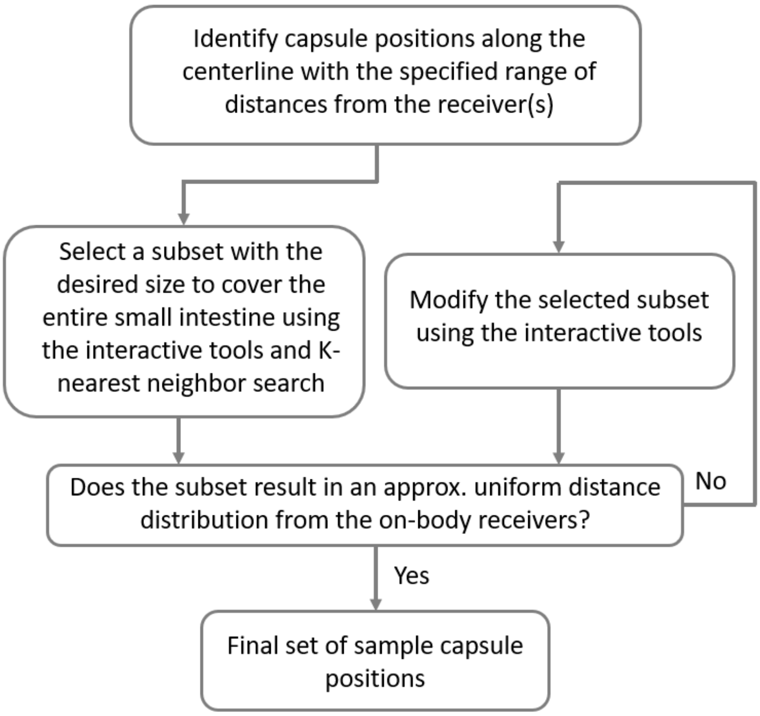

Figure 2.13: Block diagram of the process to select the final capsule positions

Following the above procedure and interaction with the 3D model of the GI tract inside NIST immersive platform, 20 candidate positions for the capsule antenna placement were carefully selected. The final set of transmitter positions resulted in an almost uniform distance distribution from all ten on-body receivers located on the abdomen surface. Histograms presented in Figure 2.14 highlight the difference in distance distribution for sample position that are uniformly spaced along the centerline, and 20 sample positions carefully selected by following the described steps.

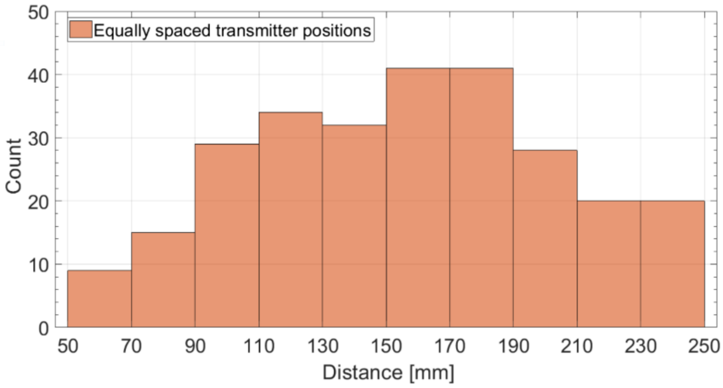

(a)

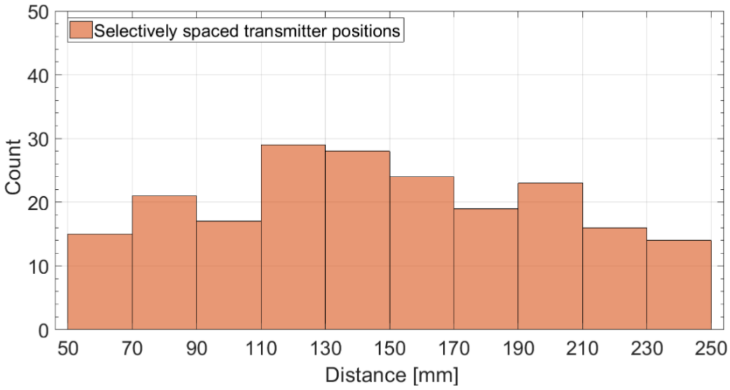

(b)

Figure 2.14: Histogram of distance distribution for (a) equally spaced sample positions, (b) sample positions selected using immersive platform

CHAPTER 3
UWB Channel Characterization in Capsule Endoscopy

3.1. Pathloss Modeling

Having the final set of capsule positions obtained by using the process described in the previous chapter, the forward transmission coefficients (S_{21}) of the wireless channel between the transmitter and each of the on-body receivers can be computed. ANSYS 3D high frequency electromagnetics solver is used to conduct the virtual experiments. A step size of 20 MHz has been used over the frequency range 3.1 GHz to 4.1 GHz to obtain the S_{21}.

Pathloss ($PL\ (d, f)$) in dB between the capsule antenna and an on-body receiver at distance d ($d \geq d_0$) and frequency f ϵ [3.1 4.1] GHz can be represented by the following log-distance model:

$$\mathrm{PL}(d,f)=\mathrm{PL}(d_0,f)+10n(f)\log_{10}\left(\frac{d}{d_0}\right)+\mathrm{S}(f)\ ,\quad \mathrm{d} \geqslant \mathrm{d}_0 \tag{3.1}$$

where d_0 is the reference distance (chosen to be 50 mm), $n(f)$ is the pathloss exponent at frequency f and $S(f)$ is the fading component at frequency f. $S(f)$ models the deviation from the mean value caused by different body tissues in the propagation path of the transmitted signal (e.g., bone, muscle, fat, etc.), multipath, and non-isotropic radiation pattern or gain of the receiver and transmitter antennas. Normally in other application like cellular, the $S(f)$ only shows fading due to the obstacles in environment. However, for this application, because there is no antenna de-embedding, $S(f)$ includes the impact of radiation pattern or gain of the antennas.

The pathloss exponent $n(f)$ heavily depends on the environment of the RF signal propagation. In free space, this exponent is two regardless of the frequency. However, since the human body is an extremely lossy environment, a higher value for this exponent is expected for propagation from wireless implants and ingestible electronics.

Using the data obtained from the 200 propagation channels, resulting from the 20 selected capsule positions and 10 on-body receivers, parameters of the statistical pathloss model were calculated through data analysis in MATLAB. The selected capsule locations inside the small intestine cover a distance range of 5 cm to 25 cm from the on-body receivers. Figure 3.1 shows the scatter plot of the pathloss for the measurement scenarios as a function of transmitter-receiver distance at 3.6 GHz frequency. The solid red line is obtained by using the least squares linear regression and minimizing the root mean square deviation of sample pathloss data points. It represents the mean value of the pathloss samples in the scatter plot.

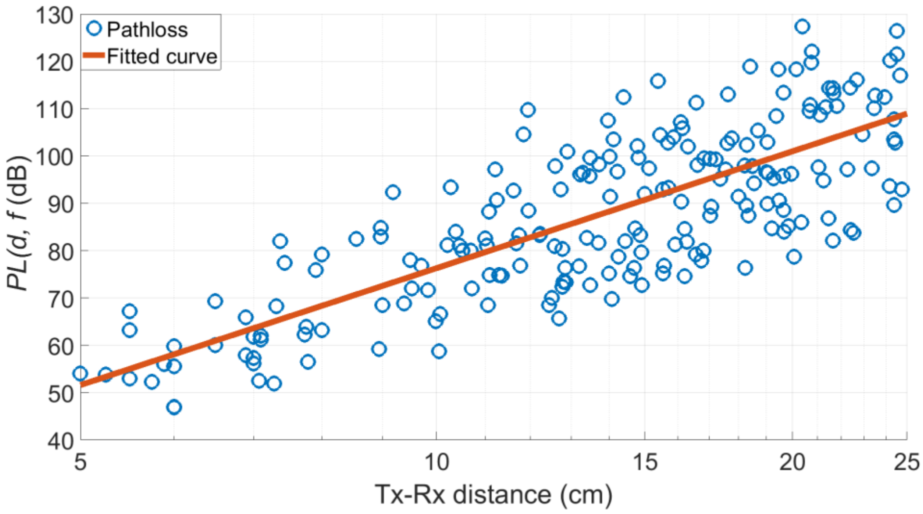

Figure 3.1: Scatter plot of the pathloss for the measured scenarios and the regression line at 3.6 GHz

Random scatter around the mean value of the pathloss occurs due to the following:

1. Changes in tissue composition along the signal propagation path between the transmitter and receiver: This happens when different transmitter-receiver pairs positioned at different locations inside or on the abdomen have the same distance. Such scenarios capture random shadow fading caused by the variations in body tissues between the transmitter and receiver.

2. Multipath: Reflections, scattering and diffraction of the signal along its path from the transmitter to the receiver could also cause multipath fading that is captured by the $S(f)$ component.
3. Changes in the relative orientations of the capsule and/or the on-body antennas: As discussed earlier, the antennas have non-isotropic radiation patterns, so any changes in their relative orientations will also affect the pathloss.

Normalized histogram of this random variable at 3.6 GHz is shown in Figure 3.2. As observed, the random variable has normal distribution with zero mean and standard deviation $\sigma_s(f)$ (i.e., $N(0, \sigma_s)$) and can be used to model the $S(f)$ component in the pathloss model (3.1). Normal distribution of shadowing was additionally confirmed with Chi-Square Goodness-of-Fit test.

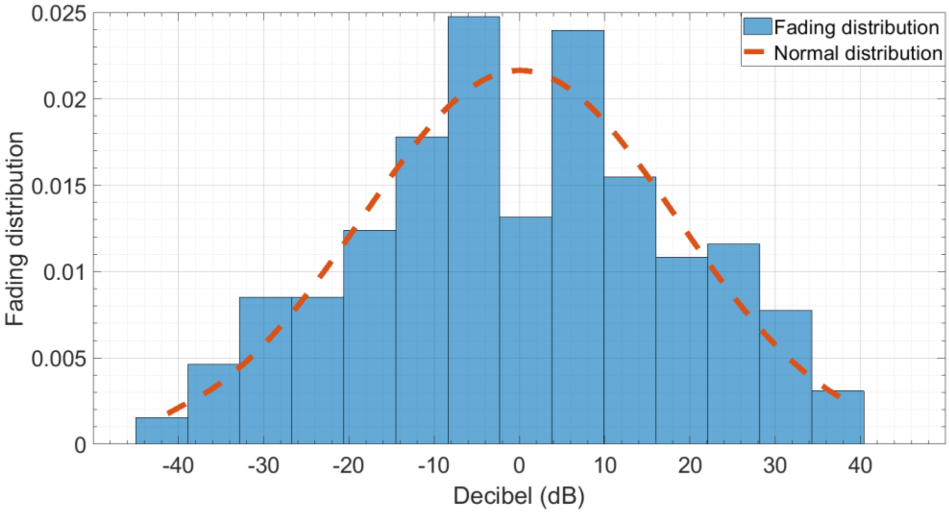

Figure 3.2: Fading distribution at 3.6 GHz

Parameters of the pathloss model in (1) can be obtained through numerical analysis at any frequency $f \in [3.1\ 4.1]$ GHz. Variations of these parameters ($PL(d_0,f)$, $n(f)$, $\sigma_s(f)$) versus frequency are shown in Figure 3.3. As observed, pathloss exponent $n(f)$ is nearly flat; however, the pathloss at reference distance and standard deviation $\sigma_s(f)$ is monotonically increasing with a slight slope. The mean values of these parameters ($\overline{PL}(d_0), \overline{n}, \overline{\sigma_s}$) over the frequency range 3.1 GHz to 4.1 GHz are provided in Table 3.1.

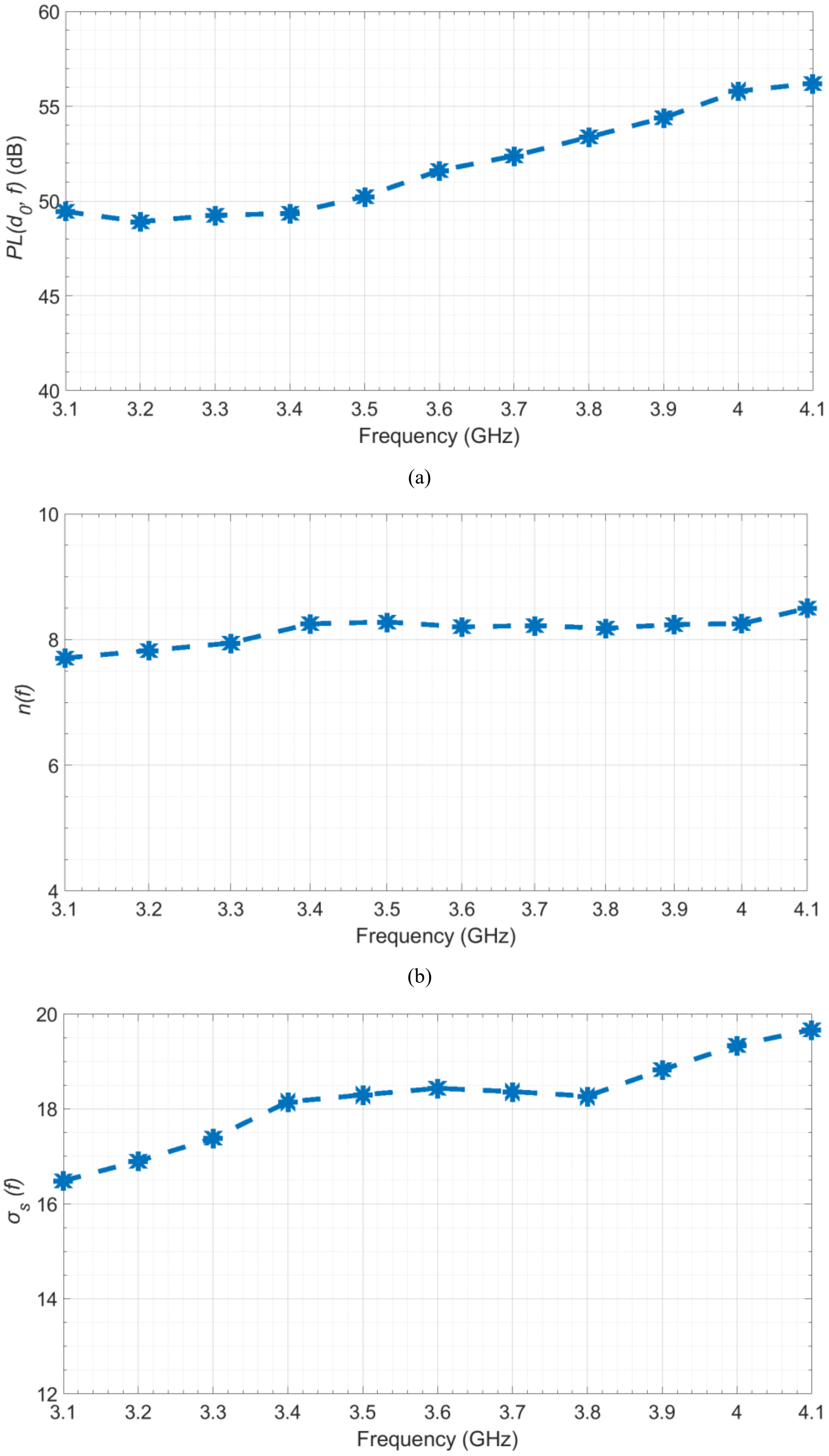

(a)

(b)

(c)

Figure 3.3: Parameters of the capsule pathloss model versus frequency: (a) PL (d0, f), (b) n(f), (c) σ_s *(f)*

Table 3.1: Mean values of the parameters of the capsule pathloss model (f ϵ [3.1 4.1] GHz)

$\overline{PL}(d_0)$ [dB]	$\bar{n}$	$\bar{\sigma}_s$ [dB]
51.9014	8.1454	18.1921

The high pathloss exponent indicates the significant loss experienced by the UWB signal due to the human body tissues. Based on the maximum allowable transmit power and receiver sensitivity, this would limit the feasible range of communication with a capsule endoscope operating at UWB frequencies. So, it can be expected that multiple receivers would be needed to exploit spatial diversity and achieve reliable communication with the capsule throughout its journey inside the small intestine. Our results also indicate the significant impact of the antenna orientation on the standard deviation of the fading component of the pathloss model. Due to the mobile nature of the capsule inside the small intestine, the accurate modeling of the signal variations caused by the imperfect i.e., non-isotropic capsule antenna pattern is critical for a reliable communication with a capsule endoscope. This necessitates better modeling of the fading component with realistic antennas, a more accurate computational body model and considering more pragmatic antenna positions for the measurements. These are all the intricate issues that have been considered in this study to generate the statistical pathloss model.

Figure 3.4 shows the comparison of results on the average pathloss versus distance with the results obtained by other researchers in [24, 25, 71]. As observed, the pathloss exponent (i.e., $\bar{n}$) is nearly in-line with the results obtained by other researchers. However, the standard deviation of the fading component obtained with this research more accurately represent the potential variations of the signal strength at the on-body receiver.

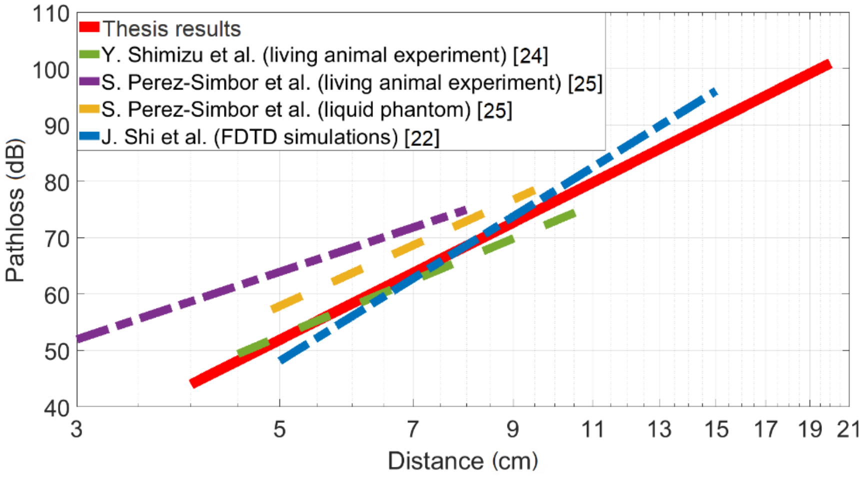

Figure 3.4: Comparison of the average pathloss

3.2. Model Verification

To partially investigate the accuracy of the model obtained through virtual measurement using the developed computational platform and compare the results with physical measurements, the liquid phantom measurement system described in [25] was emulated. A computational model of the multilayer phantom container with identical dimensions, thickness, and material properties of each layer was developed. This ensures identical propagation environments for comparison purposes.

Since verified models of the UWB transmitter and receiver antennas in [25] were not available, different antennas with approximately similar peak gain were used for the simulations, instead. For each transmitter antenna position on the grid inside the phantom and a given receiver position on the container surface, the channel pathloss for the frequencies 3.1 GHz to 4.1 GHz were computed using the computational platform. Statistical pathloss model for each frequency can be obtained following the methodology described earlier.

Because of the non-identical antennas used in the physical and virtual measurements, a full comparison of the acquired pathloss models cannot be made. However, if the measurement positions for the antennas are carefully chosen, the pathloss exponent which is indicative of the rate at which the received signal strength decreases with distance is less impacted by the differences in the antennas' performance. Figure 3.5 shows the comparison of pathloss exponents for the frequency range 3.1 GHz to 4.1 GHz. As observed, the frequency dependent pathloss exponent obtained by the computational experiment closely matches the one obtained through the physical experiment.

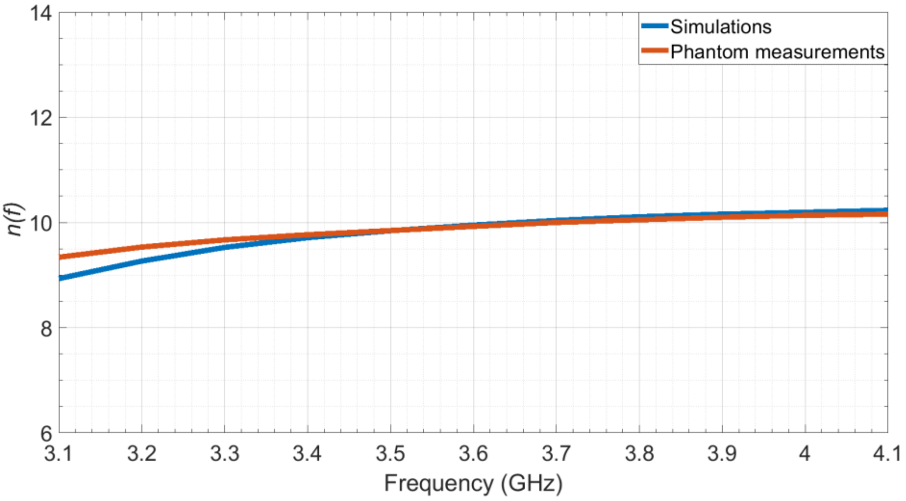

Figure 3.5: Comparison of the pathloss exponent n(f) obtained through computational and physical experiments with a liquid phantom

This comparison serves as a partial verification of the developed platform with data from measurements. Other parameters of the pathloss model such as standard deviation of the $S(f)$ component in the pathloss model could not be compared as the gain pattern of the antennas used in simulations were not identical to the ones used in the physical experiments. The same computation model of the liquid phantom was also used to study the importance of the antenna position distribution on the accuracy of the resulting pathloss model. This study can be found in [66] and will be briefly summarized next.

3.3. Sample Points Distribution

Characterization of a propagation channel involves conducting a measurement campaign (either computational or physical) and selecting a set of candidate test points. These sample points are used to collect numerical values of the desired signal at the receiver. Typically, the measurement points for channel characterization are chosen based on equally spaced locations (e.g., a rectangular grid) where either transmitter or receiver are positioned. This is a common approach in wireless channel characterization. However, as already explained in Chapter 2, careful selections of sample measurement point locations are needed for better evaluation of the UWB channel for implant applications.

Using the results in [25] and a sequence of matching computational simulations, the impact of sample measurement points on the extracted channel model was studied in [66]. The study and findings are discussed below.

3.3.1. Computational Measurement System

Using the developed platform, the core elements of the physical measurement system described in [25] were emulated using ANSYS HFSS (Figure 3.6). Computational model of the multilayer phantom has identical dimensions, thickness and material properties as the physical multilayer phantom container. The model of the phantom container also includes the divider sheet that separates the fat and muscle phantoms in the experiment. Each respective section of the container is then filled with muscle and fat tissues. The corresponding frequency-dependent material properties of these tissues are set to be identical to the liquid phantoms used in the experiment.

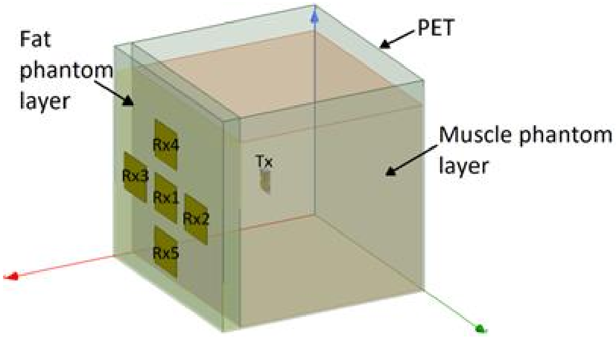

Figure 3.6: Simulated phantom container [65]

To evaluate the simulation system, the magnitude of the forward transmission coefficient S_{21} obtained through measurement and simulation were compared for a given receiver and several transmitter positions that are located at 5.5, 6.5, 7.5 and 8.5 cm away from the receiver. The receiver (i.e., on-body) antenna is located on the external side of the fat phantom layer while the transmitter (i.e., in-body) antenna is placed at the above distances facing the receiver antenna on a horizontal line in the center of the container. As observed in Figure 3.7, there is a relatively good agreement among the measured (solid lines) and simulated (dashed lines) S_{21} values versus distance.

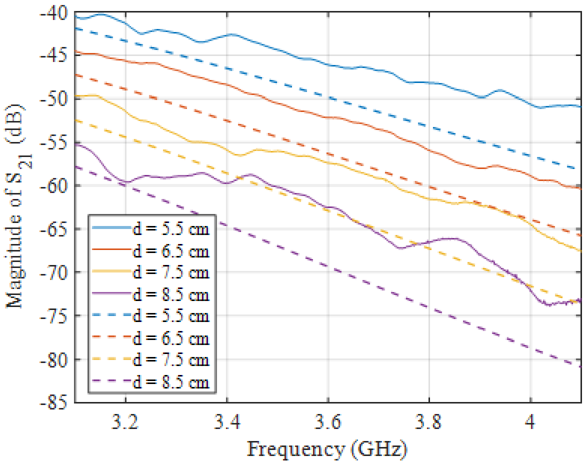

Figure 3.7: Comparison of S_{21} vs. frequency at various distances between the transmitter and receiver [65]

In the measurement process, there is a slight misalignment of the antenna pairs due to different elevations of the receiver and transmitter positions. However, in the simulations, both receiver and transmitter are on the same horizontal plane and completely facing each other. This misalignment causes the relative antenna pattern orientations between the receiver and transmitter to be different, and in turn will impact the resulting measured S_{21} values. Also, the slight difference in elevation between the receiver-transmitter means that the actual distance between the pair is slightly higher than the specified X-axis deviations of 5.5 through 8.5

centimeters. The combination of these two issues has therefore resulted in slight differences among the observed numerical values of the simulation versus measurements in Figure 3.7.

3.3.2. Impact of Grid Point Distribution

To study the impact of the measurement grid and the resulting sample point distribution, two different grids were set up in the virtual model of the multi-layer phantom as shown in Figure 3.8.

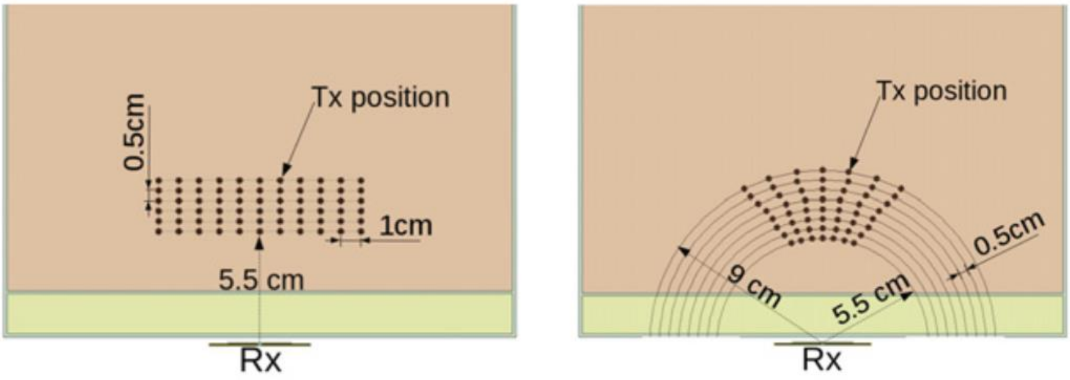

(a) (b)

Figure 3.8: (a) Sample rectangular measurement grid (b) Circular measurement grid

The rectangular grid is set up through a uniform rectangular lattice with 0.5 cm spacing on the x-axis and 1 cm spacing on the y-axis. To increase the number of sample points, two or more levels of this rectangular grid (i.e., with different elevations) can be considered for simulation purposes. Here, to minimize the impact of antenna orientation on the results, only one level of grid points (at the same elevation as the receiver) was considered. The actual distances between grid points and the receiver location (i.e., the distance between the center of the in-body and on-body antenna) will result in the histogram shown in Figure 3.10(a).

On the other hand, the circular grid is set up through intersection of circles (co-centered at the receiver location) with different radii as observed in Figure 3.8(b). The spacing between circles as well as angular spacing among different radii can be variable and chosen according to the requirement of the statistical model in consideration. In this study, the spacing between circles was chosen to be 0.5 cm; and, to minimize the impact of antenna orientation on the extracted parameters, small angular spread was considered. The circular grid shown in Figure 3.8(b) will result in the transmitter-receiver distance histogram in Figure 3.10(b).

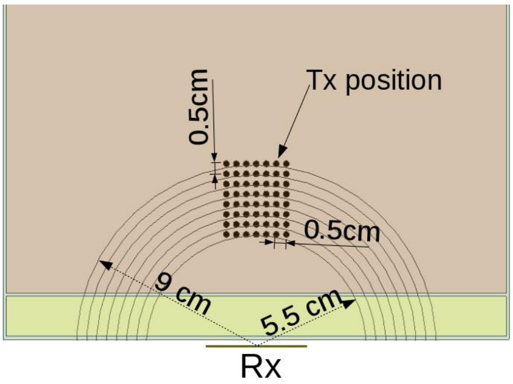

Figure 3.9: Another example of Circular measurement grid

In general, the final set of grid points do not necessarily have to lie on any circles. Instead, they can be also located in between circles spacing like shown in example in Figure 3.9. This pattern will also lead to a uniform distance histogram as shown in Figure 3.10(b).

Simulations with the computational model of the multi-layer phantom were performed using both types of grids shown in Figure 3.8 to obtain the $S_{21}(f)$ values for frequency range of 3.1 to 4.1 GHz. It should be noted that at each grid point the in-body antenna was facing parallel to the receiver and no antenna rotation was considered at any points. Through statistical analysis of these data, and again assuming the pathloss model in (3.1), the average pathloss exponent $\bar{n}(f)$ was obtained and presented in Table 3.2.

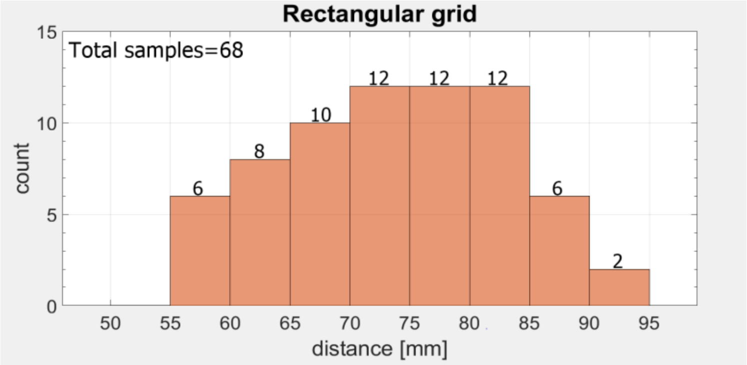

(a)

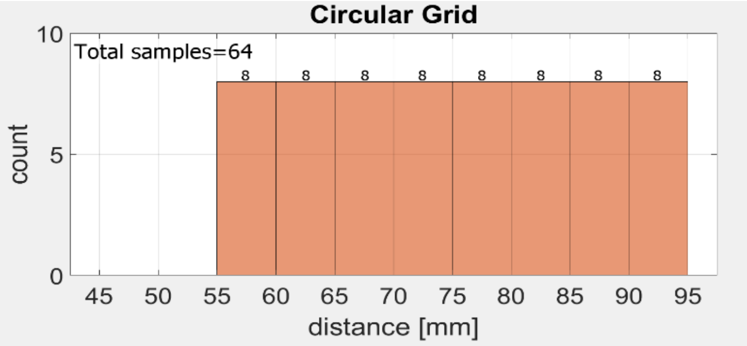

(b)

Figure 3.10: Histogram of the Tx-Rx distances in the (a) Rectangular grid (b) Circular grid

Table 3.2: Average pathloss exponent for different grids

	$\overline{\boldsymbol{n}}(\boldsymbol{f})$
Rectangular Grid	9.68
Circular Grid	10.60

The results show the potential impact of the measurement points distribution on the extracted pathloss exponent. The circular grid leads to a more uniform distribution of sample point distances; and therefore, all samples are fairly and equally represented during the statistical analysis process. This in turn could lead to more accurate channel model parameters. Mathematical nature of the statistical model can also be considered to get additional input for the grid points selection. For example, logarithmic based models can benefit from using a logarithmic scale to space out circles in the circular grid layout. The characteristics of the specific implant application in consideration can provide the overall guidelines on the arrangement and selection of optimal grid points before the measurement process.

Although only the impact on the pathloss exponent was considered in this study, it is conjectured that similar impact on other parameters of the statistical model also exists. For example, better representation of the sample measurement points could lead to a more accurate $S(f)$ which captures random variations of the pathloss around the mean value in (3.1).

The short communication distances and limited number of measurement points are among the reasons that differentiates implant communication with any other wireless channels. In general, the specifics of the intended use-case should drive the selection of sample measurement points for such channel modeling efforts. The results of this study are meant to serve as a guideline for future measurements and design of an optimal set of sample point locations to obtain UWB implant channel models. For future studies, it is also possible to expand the model to include more tissues of interest. Researchers at Institute of Telecommunications and Multimedia Applications (iTEAM), University of Valencia, developed gel phantoms for body microwave propagation [72]. These gel phantoms can be tailored to control the liquid content and absorb different mixtures in addition to water so that they can imitate different body tissues in a wide bandwidth (2-26.5 GHz). The advantage of these phantoms is that they work better with high-water content tissues, since they are based on hydrogels, but they could be cross-linked in high percentages to have a very little water content, and thus approximate tissues such as bones or fat. Moreover, they are mechanically much more resistant than natural polymers, can be swollen reversibly, and are more stable in general.

3.4. Time Domain Analysis

Time domain characterization of UWB propagation channels for wireless implants and ingestible sensors is also a challenging task that requires further research. Authors in [68, 69] have conducted preliminary time domain analysis and multipath study for an implant communication channel in the human chest. However, there are very few studies in the literature for capsule endoscopy application at UWB frequencies [29, 70, 71].

To conduct time domain analysis, frequency response of the channels for each capsule position has been converted to time domain using the Inverse Fast Fourier Transform (IFFT). A modified Hann window is also used to reduce ringing and remove any discontinuity. Figure 3.11 shows an example of the time domain response for a capsule position that is 6 cm away from an on-body receiver. Hilbert Transform has been used to detect the signal envelope (red line). As observed, this channel can be approximately represented by a single pulse with a delay of about 1.5 ns. In general, the propagation delay between a receiver-transmitter pair is determined by dividing the distance with the speed of the electromagnetics wave. In the human body, this speed is affected by the dielectric properties of the tissues along the propagation path of the RF signal. Assuming that ε_{avg} represents the average permittivity of the small intestine, muscle, fat, and skin over the frequency range 3.1 GHz to 4.1 GHz, then, the average speed of the RF signal (v_{avg}) can be approximated by the following equation:

$$v_{avg} = \frac{c}{\sqrt{\varepsilon_{avg}}} \tag{3.2}$$

For capsule endoscopy application, ε_{avg}= 49, and therefore v_{avg}= 42.86×10^6 m/s. Considering the 6 cm distance between the transmitter and receiver, the propagation delay of the channel is estimated to be 1.4 ns ((6×10^{-2}) / (42.86×10^6)). This delay reasonably matches the time associated to the peak amplitude of the time domain response as seen in Figure 3.11.

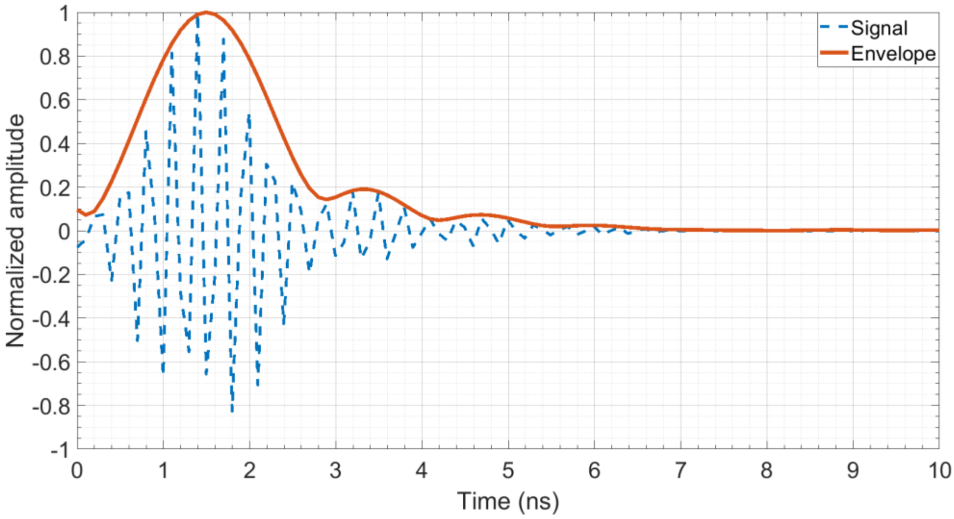

Figure 3.11: Time domain response of the channel (3.1 GHz to 4.1 GHz) between the capsule and an on-body receiver with a distance of 6cm

Different dielectric properties of various tissues in the complex environment of the human body affect the propagation of RF waves transmitted from a wireless source inside the body. For implants or ingestible electronics, it is generally assumed that the human body environment is causing multipath due to possible reflections, diffractions, or scattering from various tissue layers. However, there is a lack of research on the severity of multipath and its impact on the received signal. To investigate multipath in more detail, the time domain responses of all 200 channels discussed in Chapter 3.1. were obtained to look for examples or scenarios where non-line-of-sight paths are observable in the time domain.

Since pulse width in the channel response is proportional to the inverse of the bandwidth, a higher bandwidth using the frequency range [3.1 to 5.1 GHz] was also considered to try to better distinguish multiple paths. For the frequency range 3.1 GHz to 4.1 GHz considered so far, two propagation paths would be easily distinguishable if they are separated by 2 ns or more. For 2 GHz bandwidth, this time reduces to 1 ns. Figure 3.12 shows the normalized amplitude of the time domain response for the example scenario with the 6 cm distance between the transmitter and receiver (Figure 3.11) but using the frequency range 3.1 GHz to 5.1 GHz instead. No multipath behavior is observed for this channel even with the higher bandwidth. Looking at most of the channels with the same capsule position but different on-body receivers also did not bring up any visible multipath behavior.

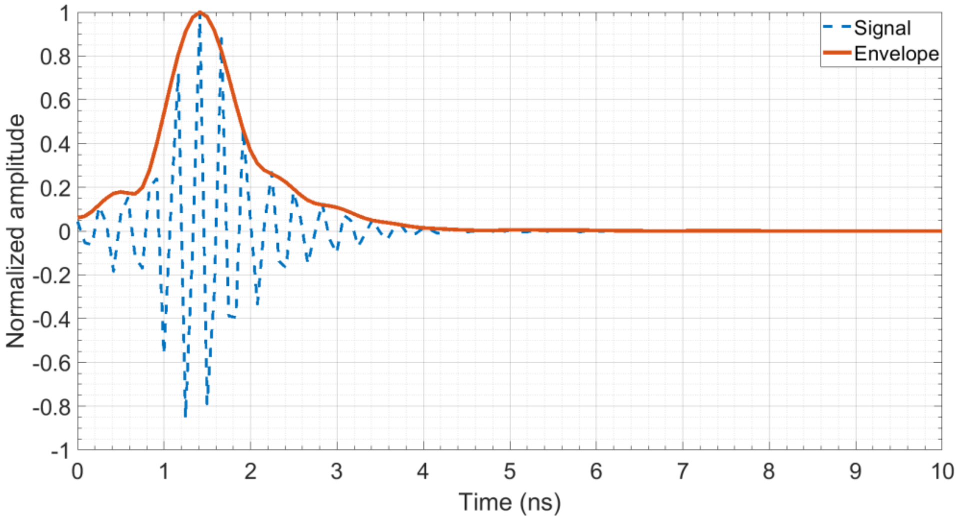

Figure 3.12: Time domain response of the channel (3.1 GHz to 5.1 GHz) between the capsule and an on-body receiver with a distance of 6 cm

The phase of the forward transmission coefficient of the channel, $\angle S_{21}(f)$, can also be used to investigate the presence of multipath. Figure 3.13 shows the phase of $\angle S_{21}(f)$ versus frequency for two separate on-body receivers at 6 cm and 12 cm distances from the capsule position. The linearity of the phase indicates that there is either one main propagation path (likely the line-of-sight) or other secondary paths are severely attenuated before reaching the receiver, and therefore cause very little or no phase distortion at the received signal. It is worth noting that, as expected, the slope of the phase plot for the receiver that is located 12 cm away from the capsule is almost double the slope for the 6 cm channel.

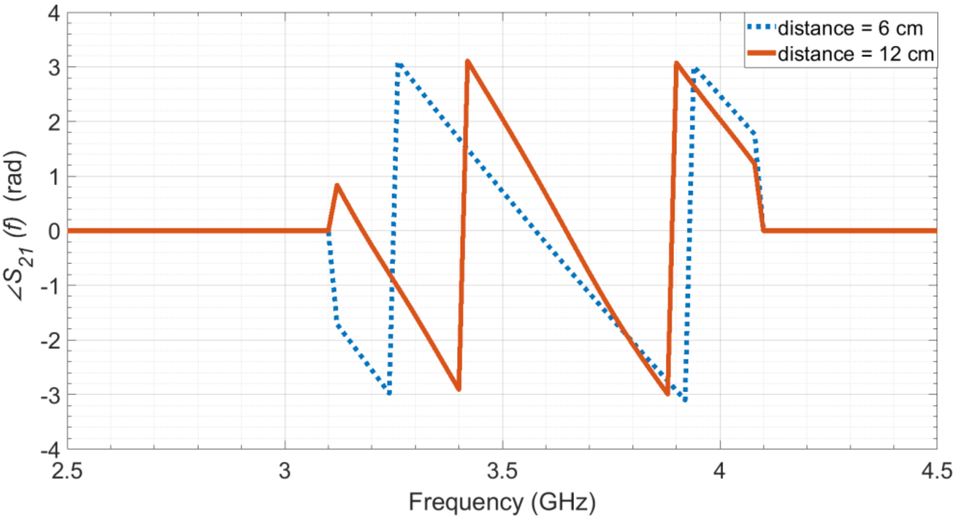

Figure 3.13: Comparison of $\angle S_{21}(f)$ for two channels between the capsule and two on-body receivers with distances d = 6 cm and d =12 cm

The capsule position corresponding to Figures 3.11, 3.12, and 3.13 is in the middle of the abdomen with no bone structure in its vicinity. Looking at other capsule positions inside the small intestine, a position in the lower segment of the abdomen, closer to the hip bone (i.e., the ilium which is the largest part of the pelvis) was also selected as another example. The channel response between this new position and an on-body receiver that is 14 cm away was calculated. Figure 3.14 shows the normalized amplitude of the time domain response for this channel using 3.1 GHz to 4.1 GHz as well as 3.1 GHz to 5.1 GHz frequency ranges. The results indicate the existence of a strong second path for this capsule position.

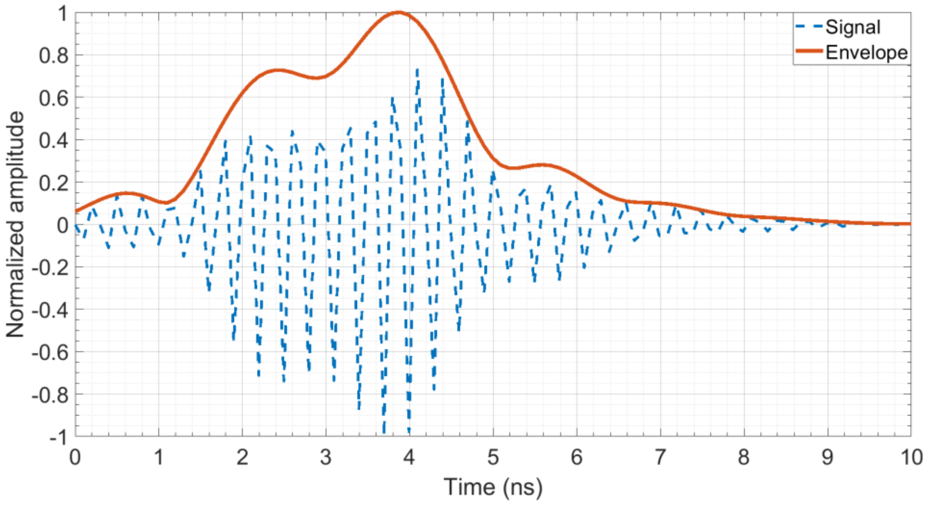

(a)

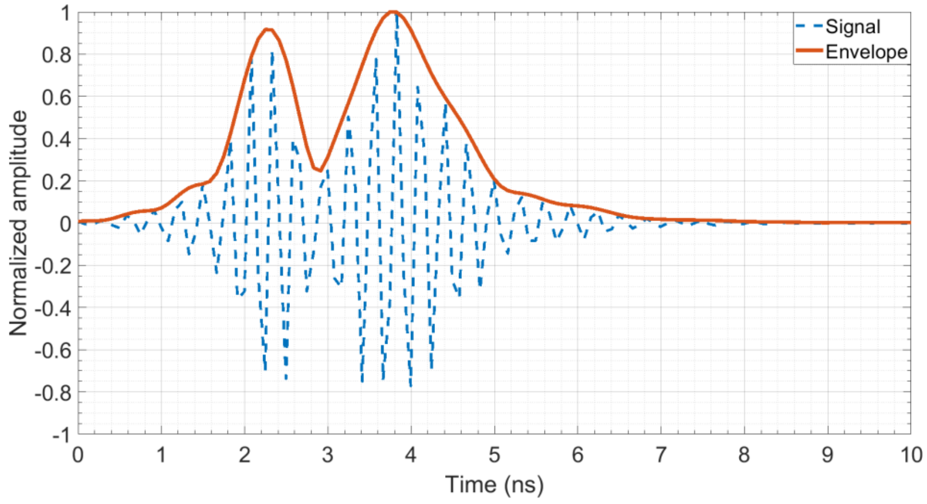

(b)

Figure 3.14: Time domain response of the channel between the capsule and an on-body receiver with a distance of 14 cm using (a) 3.1 GHz to 4.1 GHz (b) 3.1 GHz to 5.1 GHz

Although it is conceivable that the bones could contribute to multipath fading of the received signal by causing reflection, refraction, or scattering, evidence that they could lessen the impact of multipath by further shadowing (or blocking) a potential propagation path was also found. For example, choosing a capsule position in the middle of the small intestine and an on-body receiver on the side of the abdomen, simulations to obtain the channel responses with and without the skeleton in the human body model were conducted. Figure 3.15 shows the results.

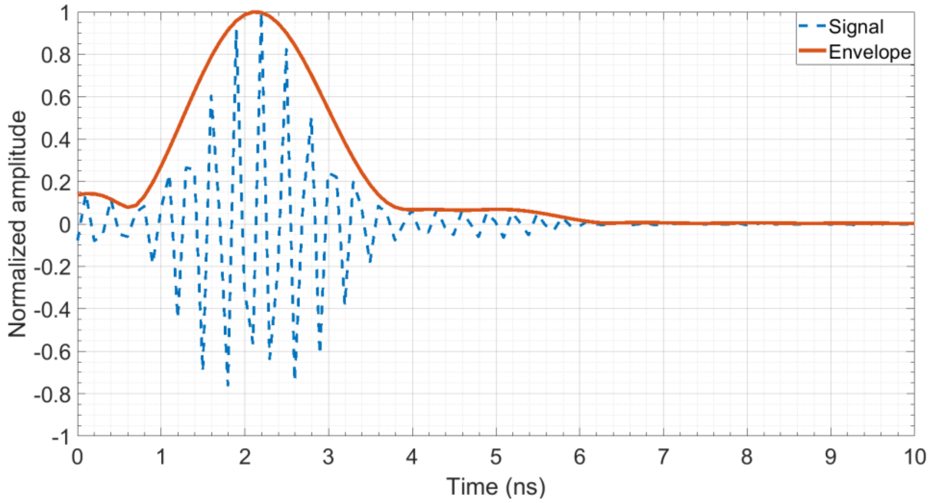

(a)

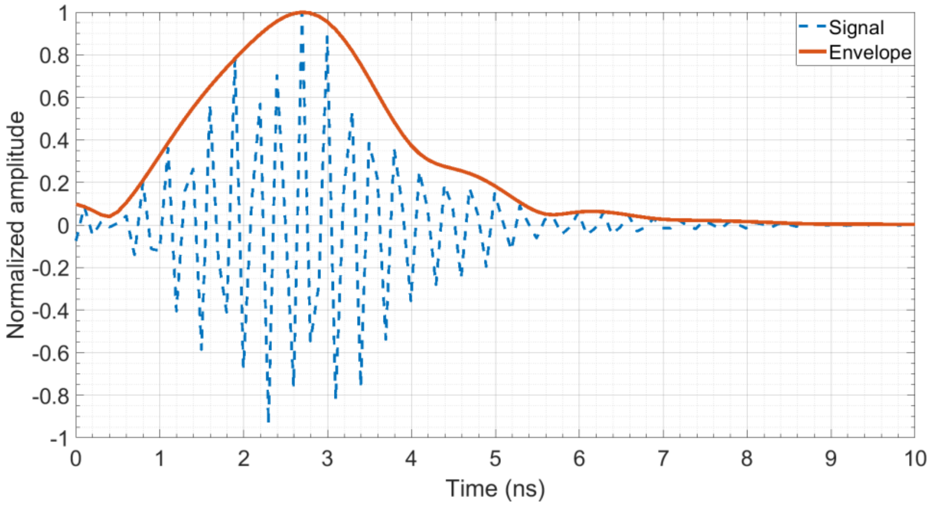

(b)

Figure 3.15: Time domain response of the channel between the capsule and an on-body receiver with a distance of 12 cm using the body model (a) with skeleton (b) without skeleton

As observed, the broadening of the pulse after the removal of skeleton is indicative of interfering paths that would have otherwise been weakened by the bones in the vicinity of the signal propagation path. Comparing the amplitude and phase of the frequency response of this channel (i.e., $S_{21}(f)$) with and without the skeleton also points to the existence of multipath as seen in Figures 3.16 and 3.17. The fading in the amplitude of $S_{21}(f)$ around 3.3 GHz (Figure

3.16) and the nonlinearity of the phase of $S_{21}(f)$ as evident in the phase derivative plot (Figure 3.17(b)) are both indicative of the impact of multipath distortion in this channel.

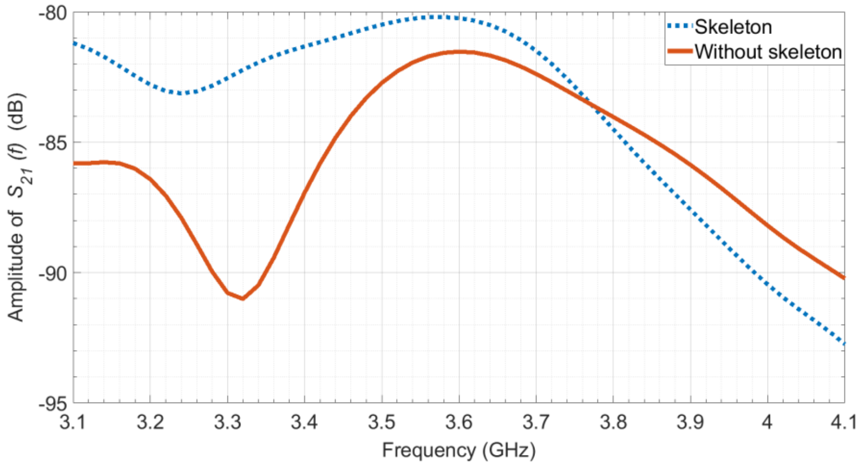

Figure 3.16: Amplitude of $S_{21}(f)$ for the channel between the capsule and an on-body receiver placed on the left side of the abdomen

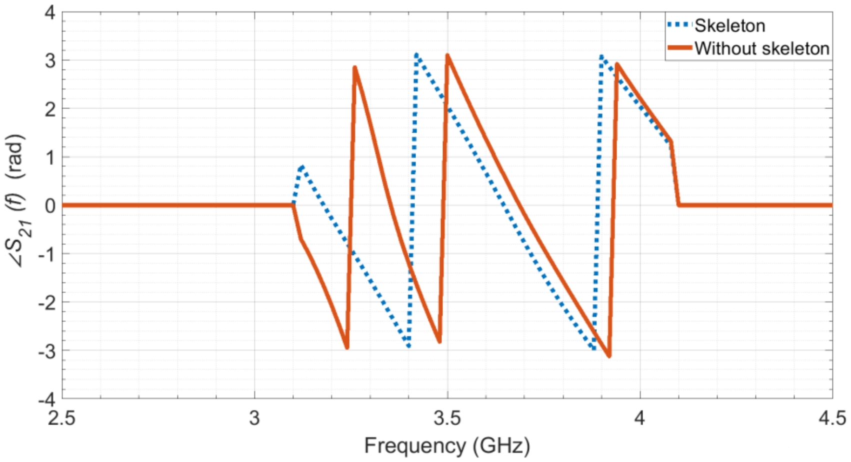

(a)

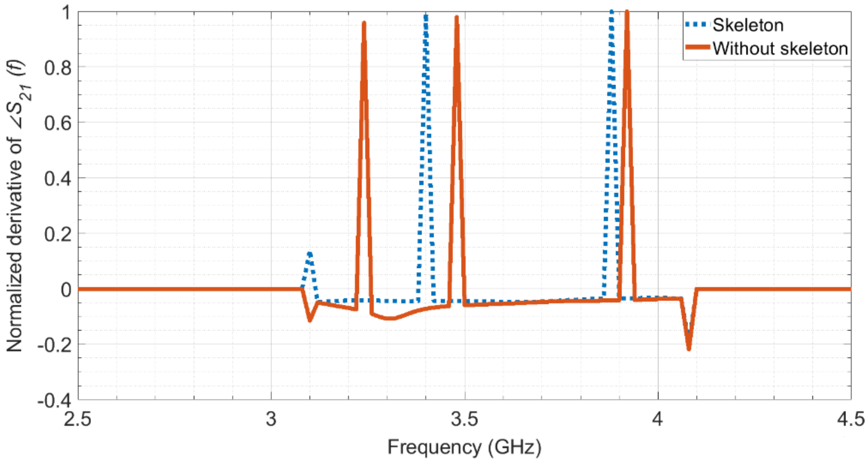

(b)

Figure 3.17: (a) Phase of $S_{21}(f)$ (b) phase derivative of $S_{21}(f)$ for the channel between the capsule and an on-body receiver on the abdomen side

Investigating the presence of multipath, scenarios where the first arrival path is not necessarily the direct path between the transmitter and receiver were also observed. There are possible capsule and receiver antenna positions that could result in a first path being a diffracted path from the body surface (through creeping waves) while the weaker second path is the direct line-of-sight path between the transmitter-receiver pair. In those scenarios, the arrival time of the first component could be earlier that the arrival time of the direct line-of-sight path between the transmitter-receiver pair. This is again due to the higher speed of the electromagnetics wave on the body surface (for the diffracted path) versus in-body propagation speed (for the direct line-of-sight path). This phenomenon will be further discussed in next section.

Presented time domain results indicate higher signal attenuation in the human body with increasing frequency. Therefore, it is informative to know the most effective range of the frequencies within the unlicensed UWB spectrum that can be used for capsule endoscopy. Consider $E(f_h)$ to be the energy of the received signal when the bandwidth $f_h - 3.1$ GHz is utilized by the capsule UWB transmitter. Then, for a given transmitter and receiver locations, $E(f_h)$ can be calculated as follows.

$$E(f_h) = \int_{3.1\times10^9}^{f_h} |S_{21}(f)|^2 df \tag{3.3}$$

Next, define the relative increase in the energy of the received signal when the bandwidth $f_h - 3.1$ GHz is utilized compared to the case when 3.1 GHz to 4.1 GHz frequency range is used by the following equation.

$$I(f_h) = \frac{E(f_h) - E(4.1)}{E(4.1)} \tag{3.4}$$

For the examples discussed earlier in this chapter, I (5.1) = 0.1245, and I (6.1) = 0.1349. In other words, using 2 GHz or 3 GHz bandwidth only results in a 12% and 13% increase in the energy of the received signal respectively. For this reason, the proposed practical range for using unlicensed UWB frequencies for capsule endoscopy application is 3.1 GHz to 4.1 GHz.

3.5. Visualization of the Multipath Propagation

To get more insight into the dominant propagation paths, data from the Poynting vectors in the 3D space between the transmitter and receiver can be used. The Poynting vector at a given point in space is defined as the cross product of the Electric and Magnetic field vectors:

$$\vec{\boldsymbol{S}} = \vec{\boldsymbol{E}} \times \vec{\boldsymbol{H}} \tag{3.5}$$

where **E** is the electric field vector and **H** is the magnetic field vector.

The Poynting vector represents the directional energy flux (the energy transfer per unit area per unit time) of an electromagnetic field. The flux of the Poynting Vector through a certain surface represents the total electromagnetic power flowing through that surface. Therefore, at each point in space surrounding the transmitter, the direction and magnitude of the Poynting vector provides information on the direction and intensity of the flow of RF energy at that particular point in space, respectively. The flow of RF energy between the transmitter and the receiver can be visualized by constructing and displaying “streamlines”, which are 3D paths that are derived from the Poynting vector field. Each path is constructed by treating the Poynting vector field as a flow field, ensuring that the Poynting vector field is tangent to the streamline throughout its length [73]. A seed point is selected first and then numeric integration from that point both forward and backward through the Poynting vector field is performed. A fifth order Runge-Kutta method with adaptive step size [74, 75] control is used to perform the integration. This algorithm is available through the open-source visualization application ParaView [76] which uses the implementation of this method from the open-source VTK library [77].

The streamlines as mentioned above provide an effective way to visualize the flow of the RF energy from the transmitter and therefore study multipath behavior of the channel. To generate them, the Poynting vector field data are calculated in a defined volume using electromagnetic simulation solver (Ansys HFSS software). The data is then imported into ParaView and streamlines are visualized using the customized code Stream Tracer filter. The starting seed points are placed on the surface of the receiver in a 5×5 grid giving 25 seed points total. To capture other possible propagation paths another set of seed points is placed behind the receiver. Using backward integration, the algorithm then traces the streamlines of vector field back to the transmitter.

3.5.1. Poynting Vector Streamlines for a Simplified Phantom Model

The flow of the RF energy was first studied for a simplified layered phantom model and one Tx-Rx link. Simulations were performed with the same computational model of the multi-layer phantom from study in [66] mentioned in chapter 3.3.

The simulated multi-layer phantom container, shown in Figure 3.18, is made of polyethylene terephthalate (PET) material with a width of 1.5 mm and has an overall internal volume of 25 × 25 × 25 cm^3. The container consists of two layers, with dimensions of 23 × 25 × 25 cm^3 and 2 × 25 × 25 cm^3 for muscle and fat layer respectively. The simulated container also includes the divider sheet that separates the fat and muscle liquid phantoms. Each segment of the container is then filled with muscle and fat with the corresponding frequency-dependent material properties of these tissues.

Capsule antenna is placed inside the muscle tissue and on-body receiver to the outside of the container, with distance of 8 cm between them. To capture all possible propagation paths, antennas are positioned in a way that they are not directly facing each other. Moreover, the capsule antenna was rotated in several different directions.

The Poynting vector values were calculated in the Fields Calculator extension of the Ansys HFSS electromagnetic solver software. Poynting vector was calculated for a defined volume enclosing the capsule and on-body antennas at 3.6 GHz. The resulting data were then imported into ParaView for visualization using the streamline tracer. Figure 3.19 shows the propagation paths of the transmitted RF signal while the orientation of the capsule antenna changes. The values of the Poynting vector magnitude are normalized for better clarity. As observed, irrespective of the orientation of the capsule antenna, the signal arrives at the receiver mainly through two distinguished paths. The first is the direct path, i.e., the shortest distance or equivalently line of sight path between the capsule and receiver. The second path is an indirect (none-line-of-sight) path where the transmitted signal travels through the shortest path to the surface and then propagates over the surface similar to creeping waves toward the receiver.

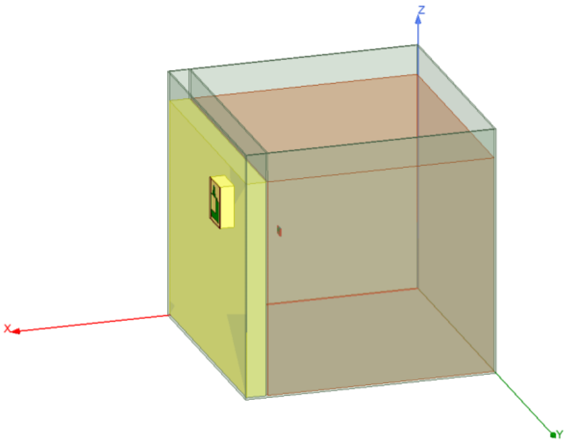

Figure 3.18: Virtual phantom container setup for streamline visualization simulations

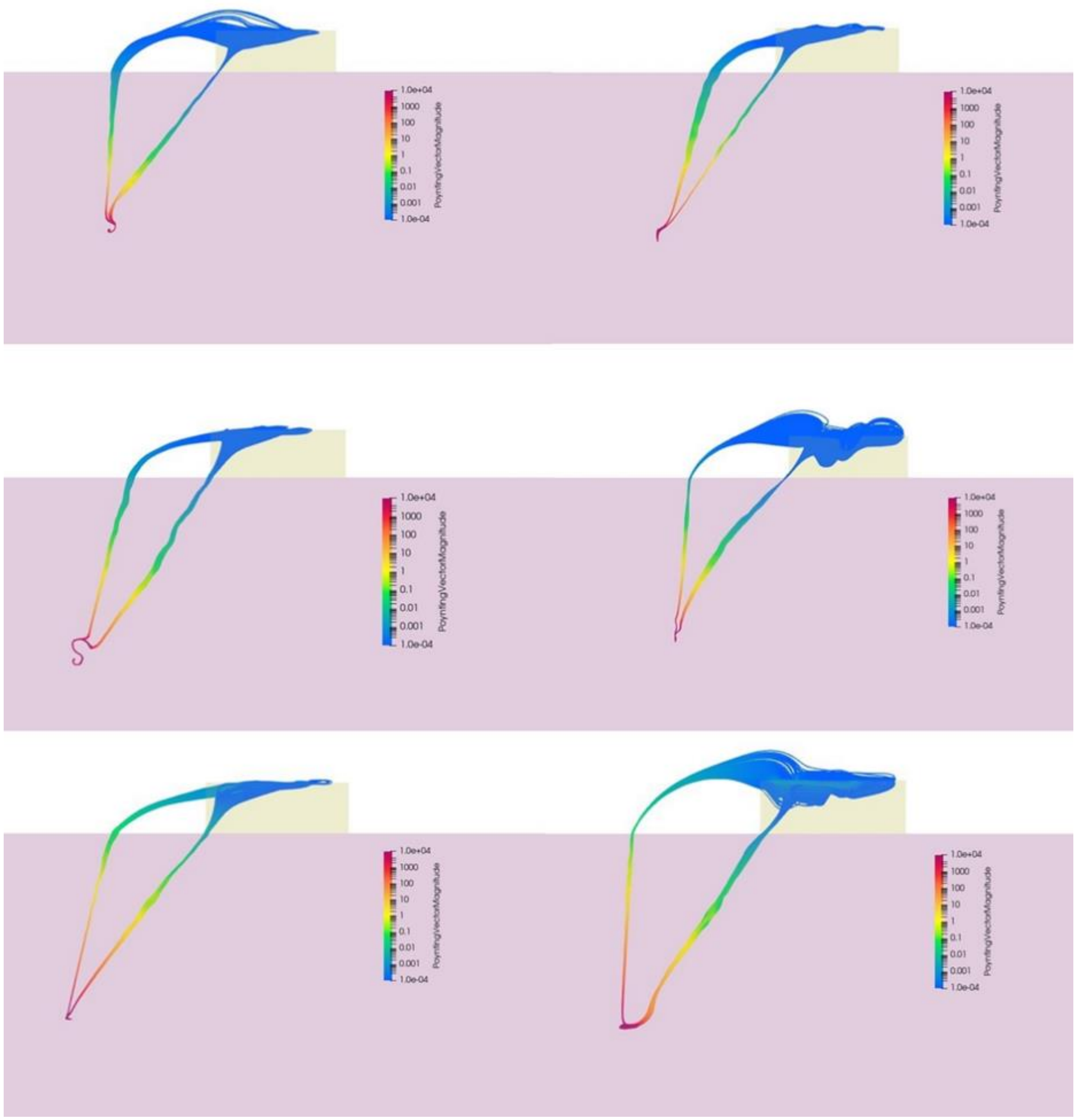

Figure 3.19: Propagation paths for different capsule antenna orientations

3.5.2. Poynting Vector Streamlines for the Computational Body Model

Propagation of the radio waves through the computational human body model was also studied using streamlines visualization. Using Poynting vector field data obtained through electromagnetic simulation solver, the signal path between a capsule antenna transmitter inside the GI tract and a receiver on the abdomen was obtained. The Poynting vector data vas imported into ParaView and visualized using streamlines tracer algorithm.

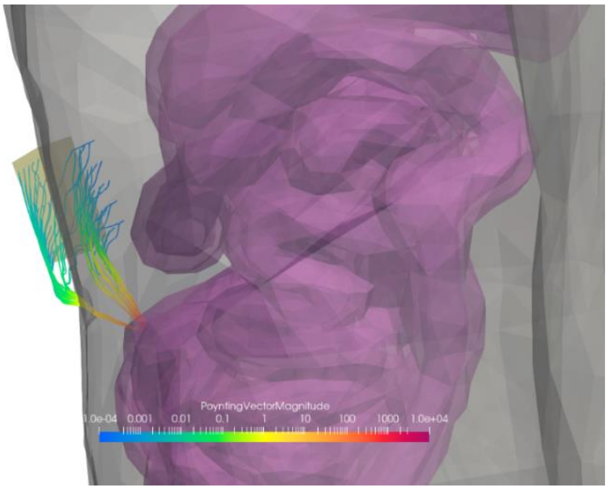

Figure 3.20: Visualization of the propagation paths from the capsule inside the GI tract using streamlines

The streamlines in Figure 3.20 show propagation paths from one capsule position inside the small intestine and the receiver Rx1 on the body surface. As observed, the signal propagation is again mainly through two distinguished paths i.e., direct line-of-sight and indirect through the body surface. The time domain channel response for this communication link is shown in Figure 3.21. The direct distance between the capsule antenna and the receiver for this scenario is 110 mm. Using equation (2) for the average speed of the RF signal, the propagation delay of this direct path is estimated to be 2.56 ns. This delay approximately matches the second peak of channel response shown in Figure 3.21. Going through different capsule and receiver positions, similar multipath behavior was observed. In other words, when there are two noticeable paths in the channel response, the first path is typically a diffracted path from the body surface (through creeping waves) while the weaker second path is the direct line-of-sight path between the transmitter-receiver pair. In those scenarios, the arrival time of the first component is earlier than the arrival time of the direct line-of-sight path between the transmitter-receiver pair, although the indirect path is usually longer in the traveled distance than the direct path. This is again due to the higher speed of the electromagnetics wave on the body surface (for the diffracted path) versus in-body propagation speed (for the direct line-of-sight path).

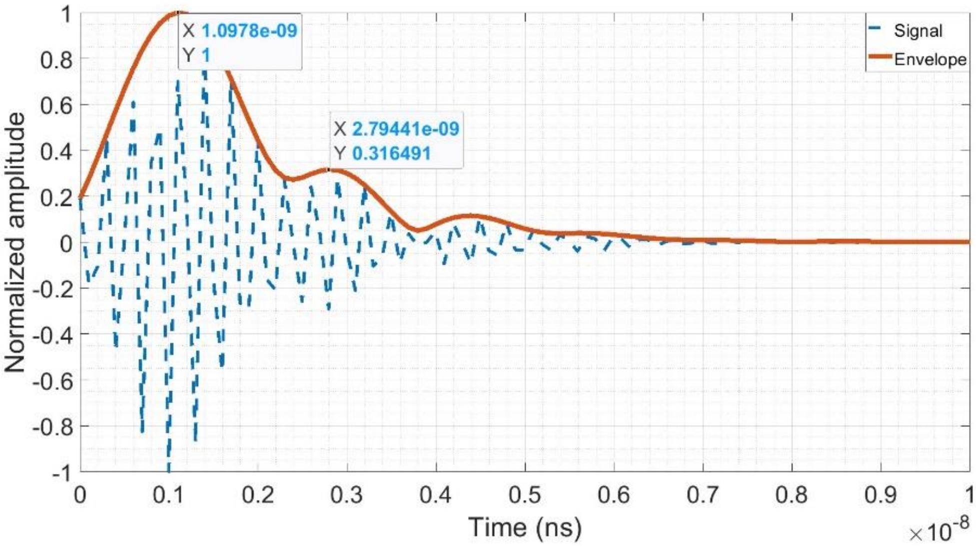

Figure 3.21: Time domain response of the channel between the capsule and an on-body receiver Rx1

CHAPTER 4
Capsule Orientation Estimation

Eighteen years after the first invention of this technology, positioning and mapping metrology science in this area is still in its infancy. As a result, doctors receive clear pictures of abnormalities such as bleeding and tumors inside the GI-tract, but they have no way to determine their precise locations within the body or the relative distance of the abnormality from an anatomic landmark such as the pylorus or the ileocecal valve. This is due to lack of knowledge about location and orientation of a capsule at the time when an image is taken. Lack of such critical information necessitates follow-on use of expensive and invasive testing such as deep enteroscopy, CT enterography, or even surgery to determine the site of the tumor, lesion, or bleeding. The elasticity of the GI tract and looped and folded nature of some its components (e.g., small intestine) along with variable speed and irregular motion pattern of a WCE pose several unique metrology challenges for this problem. Therefore, as of now, there are no reliable methodology that can accurately determine the location and/or orientation of the CE inside the GI tract.

For the current commercially available CE, the simplest approach is the transit-time based localization. In this approach, the times of the capsule entry to the stomach, duodenum, and cecum are identified, and then, the capsule position is estimated based on the elapsed time from one of these landmarks [60]. This technique has low precision in the estimated position due to the irregular motion of the capsule. Given Imaging has tested their RF-based localization by measuring the received signal strength (RSSI) at the sensors on the patient’s abdomen. The tracking algorithm made location predictions based on the observation that as the transmitter moves closer to the receiver, the receiver will detect stronger signal. Researchers in [78] evaluated the Given Imaging localization algorithm by comparing the predicted location and real positions provided by fluoroscopic images. The average error was found to be 3.77 cm and, due to the high inaccuracy, this technique has been withdrawn in the end. Olympus also tried an RF-based localization method to approximate the location of the capsule for their EndoCapsule system. Compared to the Given Imaging, they added a Z-dimension to allow for 3D localization. In a validation study involving 30 volunteers [79] results showed that the average error, compared to fluoroscopic control images, was 2.00, 2.64, and 2.51 cm for X, Y, and Z coordinates respectively.

As the CE continues to evolve and increase its performance, more precise methods of localization and measurement of traveled distance are needed. Current commercially available CEs operate at MICS frequency range of 402 MHz to 405 MHz, but they lack the ability to meet the demands for high-quality video and reliable localization. Since the next generation of endoscopy capsules are expected to achieve higher quality images and videos, as well as have more diagnostic and therapeutic functionalities, Ultra-Wideband (UWB) technology has been considered for the wireless communication links between the transmitter antenna inside the capsule and the receiver antennas located on the body. Although UWB signals experience high attenuation inside the body, this technology is still a leading choice for future CE and its accurate localization due to advantages such as higher bandwidth, increased data rates, and simpler transceiver design.

4.1. Literature Overview

In the past several years, there have been several studies on the development of an accurate localization system for CE. The techniques that have been used for this purpose can be divided into the following categories:

- Electromagnetic (RF) localization
- Magnetic localization
- Video localization
- Other localization techniques

Electromagnetic (RF) localization

Localization using RF signals is regularly used for locating an object in both outdoor and indoor environments with the accuracy around tens of centimeters to a few meters [80]. With the introduction of BAN and implantable medical micro-robots, researchers have started to utilize this technique for localization inside the human body. Using the RF signal that is used for image transmissions by the CE to also locate the capsule offers a natural and low-cost solution. However, using radio frequency for tracking a CE while moving inside a complex environment, such as the GI tract, is a challenging task. High frequency signals suffer from high attenuation when passing through different body tissues, while low frequency signals, because of their long wavelengths, are not able to deliver the desired precision.

The basis of RF-based localization for CE is to apply a well-known localization method to the same RF signal that is used for transmitting video images to the receivers on the body surface. Some of the methods considered in literature are received signal strength (RSS), time of arrival (ToA), and direction of arrival (DoA). RSS method is the most commonly used. Transforming the received signal into a distance between the capsule and sensors on the body surface, position of the capsule can be then estimated using approximation or estimation algorithms such as trilateration, least square method, or maximum likelihood algorithm [81].

While localization performances of RF-based techniques in the MICS band are widely available in literature [81–83], studies conducted in the UWB frequency band are still limited. Pathloss model plays an important role in the RF-based localization methods. However, there is a lack of standardized channel model for in-body to on-body communications at UWB frequency. In order to reduce the position error of RF localization method, it is necessary to first develop a more accurate attenuation model for capsule endoscopy. UWB signals, in addition to enable low power consumption and high data rate, also have capability of the more precise localization and tracking. Having a reliable UWB propagation channel model could offer improvements in current RF localization techniques.

Measurement campaign at 2–2.4 GHz using a homogeneous phantom model to investigate the influence of body tissue on the accuracy of ToA-based ranging technique is presented in [84]. Results showed the possibility of achieving average localization error 1.5cm for TOA based localization technique. However, to achieve these levels of accuracy, more than 32 sensors on the body surface are needed. Moreover, the phantom used for measurements was filled with purified water which is not an accurate representation of human body dielectric properties. Also, homogeneous phantoms emulate only one human tissue and do not provide accurate representation of the complex human body environment.

A compressive sensing (CS) based localization algorithm is presented in [85]. The algorithm utilizes signal sparsity in the RSS measurements using the computer simulation technology (CST) simulator with a finite integration technique (FIT) solver in 1–3 GHz and 3–5 GHz frequency bands. The best performance showed a mean localization error of 40 mm. However, the results were derived from limited amount of simulation data which lowers their reliability.

In [86] UWB frequency band has been used for RSS-based localization of CE. In-body antenna coordinates were estimated in 2D and 3D using linear and nonlinear least square method. For 2D localization, experimental laboratory measurements using a two-layer liquid phantom have been conducted. For 3D localization, data from *in-vivo* experiment have been used. Average relative localization error below 1 cm was achieved for both 2D and 3D localization. Nevertheless, the experimental setup used aligned UWB transceiver/receiver patch antennas with a maximum distance of 80 mm between the capsule and antenna on the body surface. In real scenario, CE passing through the GI-tract will likely exceed 80 mm distance from on-body receiver and antennas would not be aligned.

Magnetic localization

Advantage of magnetic field-based localization is that static and quasi-static magnetic fields have negligible interaction with the human body. Magnetic signals can pass through human tissue without any attenuation and, moreover, magnetic tracking is a non-line-of-sight method which means the capsule does not need to be in the line of sight with magnetic sensors in order to be detected. The results reported in literature showed that the magnetic-based localization outperforms both video and RF-based localization when it comes to achievable localization accuracy [82].

The magnetic field-based methods can be divided into static and quasi-static magnetic localization. Static magnetic localization approach uses external sensors to localize a small permanent magnet embedded inside the capsule. Generated static magnetic field is sensed by a sensor array placed around the abdomen of a patient [87–90]. The position and orientation of the capsule can then be estimated using the dipole model and nonlinear equation system algorithms.

For quasi-static magnetic localization an active coil fed with alternating current is placed outside the body and used as a magnetic field source. Generated magnetic field is sensed inside the capsule with a receiver coil [91] or magnetometer [92]. However, due to the limited space inside the capsule, the number of receiver coils/sensors is restricted. Additionally, coils worn on the abdominal surface use large batteries and high currents which might result in heating problems and be a potential risk for the patient.

Permanent magnet integrated into a capsule is a passive magnetic field source so additional batteries are not required. Also, a large number of sensors can be placed on the body surface. However, at the sensor array on the body surface, the magnetic flux of the permanent magnet is of the same order as the geomagnetic flux density. Consequently, both flux densities are interfering which leads to high localization errors and no reliable localization is possible without using a geomagnetic compensation [91].

Video based localization

Since CE is equipped with cameras, image analysis and computer vision can be used to determine motion of the capsule inside the GI tract [94–96]. The main advantage of video-based localization is that there is no requirement for extra hardware. Moreover, the tracking of the capsule is separated from the on-body sensors worn around the abdomen, which means the dynamic activities will not interfere with localization. Because the CE changes position and direction very slowly, some identical areas exist in the two successive endoscopic images, and the matching point pairs in these two images can be found. Using the image correspondences between points, regions or features in two consecutive frames, the motion (rotation and translation) parameters of capsule endoscope with an appropriate algorithm can be determined [97]. Oliveira et al. [98] conducted a comprehensive study where various image registration algorithms were evaluated and compared. The setup for experimental validation consisted of an ex vivo porcine colon in which a robotic arm moved an MC1000 Mirocam capsule at a constant speed. The results revealed that the well-known deep-learning method applied for image registration yielded the smallest errors. However, calibration was not performed, and so the localization errors were not determined in physical length.

In the majority of the video-based methods, simulation and experimental studies did not consider the elastic movement of the intestine walls. In addition, straight trajectories of capsule moving at a constant speed were used which do not convey the complexity and periodical contractions of the GI tract. Some of the constraints for the accuracy of video-based localization are the limited image quality and the frame rate of capsule endoscopes due to the low battery capacity and capsule operating at a low frequency. Overall, research on video-based localization of CE is considered to be in early stages and *in vivo* measurements must be conducted in future research to validate the reliability of video-based methods in real scenarios.

Other localization techniques

Hybrid localization methods are also considered for localization of CE to improve accuracy and performance of main localization methods. These methods usually combine two of the main approaches; the video-based method to enhance the accuracy of RF-based method or using inertial measurement unit (IMU) together with video-based, RF-based, or magnetic field-based localization method. Combining video-based and RF-based methods requires no additional hardware inside the capsule, while the second method requires integrating an IMU inside the capsule which can be challenging due to the limited available volume inside the CE. Bao et al. [99] proposed a hybrid localization technique by data fusion of vision and RF sensors. The proposed hybrid technique extracts motion information from the image sequences captured by the embedded visual sensor and combines it with the emitted RF signal. This enables to simultaneously localize and map the path traveled by the CE. Experimental results, conducted in MICS frequency band, showed that the proposed hybrid algorithm can reduce the average localization error and a 3-D map can be precisely constructed to represent the position of the CE inside small intestine. However, this method was only evaluated in a virtual, computational model and movement of the intestine walls was not considered.

In [100] researchers integrated an IMU together with four cameras into an CE. IMU was used to monitor the capsule’s orientation and direction of travel, while the cameras, installed along the wide wall, were responsible to measure the actual capsule movement. The displacement and orientation data were then fussed to determine the traveled distance. The reported approximate relative distance error was low (3.7%), and the estimate localization was accurate within 5-7 mm range. However, the capsule was moved along a linear trajectory within the porcine intestine for 45s, which does not reflect the looped, complex nature of the GI tract and diagnosis procedure of CE that lasts for at least 8 hours.

From this brief overview, it can be concluded that majority of recent publications and research activities on UWB CE are focused on developing methodologies that can achieve accurate position estimation. However, as the miniaturized camera in these capsules do not have a wide view angle, knowledge of the capsule orientation inside the Gastrointestinal tract could also be a valuable information for the physicians who review the transmitted images. This adds another layer of complexity to the already challenging localization problem for such capsules. Previous research on the detection (or control) of capsule orientation involved using magnetic field.

As one of the main objectives of this doctoral thesis, a preliminary study of capsule orientation estimation based on the RSS has been performed [101]. For simulations and data analysis, a specialized computing facility along with an immersive computational platform has been used. As it will be shown, the results indicate the possibility of extracting some orientation information from the RSS data.

4.2. Computational Platform and Coordinate System

As previously discussed in Chapter 2, a novel 3D immersive platform to evaluate the propagation channel between a CE and several on-body sensors has been developed. Additionally, a detailed, high-resolution 3D model of the GI tract has also been developed and integrated within a 3D computational human body model of an adult male. The 3D body model includes complex frequency-dependent dielectric properties of over 300 anatomical parts of a male human body. These dielectric properties are all user-definable, offering the flexibility in case a custom modifications or changes are desired.

Validated models of developed practical antennas (Figure 2.4 and Figure 2.7) have also been integrated into the computational system. This enables an accurate characterization and detailed analysis of the wireless link between the capsule and the on-body receiver antennas. Figure 4.1 shows the three-dimensional in-body radiation pattern of the transmitter antenna operating at a frequency of 3.6 GHz, assuming the capsule is located inside the small intestine.

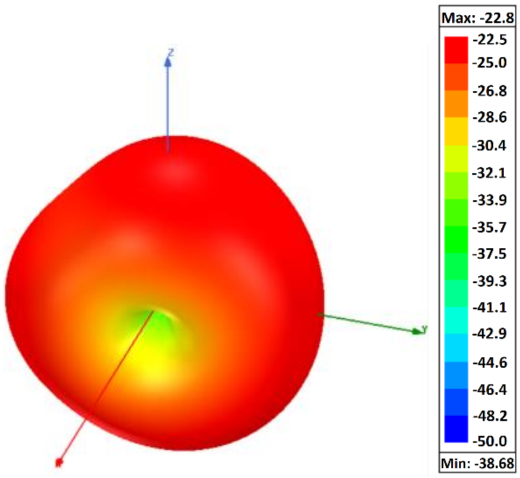

Figure 4.1: Transmit antenna in-body radiation pattern at 3.6 GHz

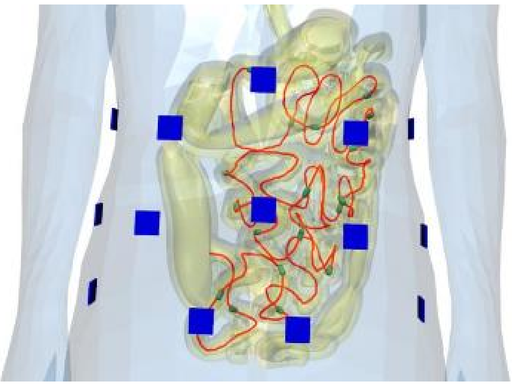

Figure 4.2: Locations of the on-body receivers (blue squares) and the centerline passing through the small intestine (red line)

The centerline that passes through the GI tract in 3D space has been calculated and used as the reference line for the capsule placement inside the small intestine (shown as a red line in Figure 4.2). Fourteen on-body receivers, indicated with the blue squares in the same figure, have been placed around the abdomen area to collect the received signal strength (RSS). The RSS values can also be additionally processed to get some information about the orientation of the transmitter antenna or the capsule. This can be observed by looking at the coordinate system in Figure 4.3. In this coordinate system, the angles α and β represent the orientation of the capsule positioned at the origin of a coordinate system. Also, this coordinate system is parallel to the global coordinate system of the platform and the body model.

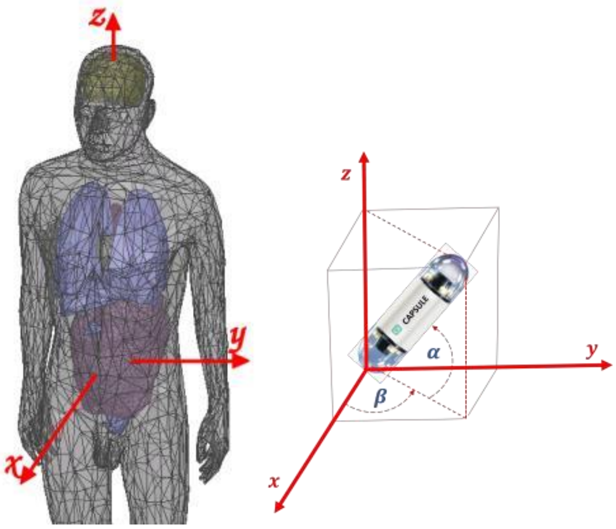

Figure 4.3: Specification of the capsule orientation (α and β)

To conduct an orientation estimation study, a high-performance computing server and Ansys Electronic Desktop software were used to perform simulations and obtain the forward transmission coefficient of the channel for the 3.6 GHz frequency.

Simulations were performed for three different sample positions with capsule antenna positioned at the beginning of the small intestine, about halfway through the length of small intestine, and close to the end of the small intestine. S_{21} was calculated at each position for direction of the antenna specified by α and β. Both α and β were varied from -90° to 90° in steps of 45°. For the second part of the study, capsule antenna had fixed orientation but was moved along the centerline in linear increments of 0.25 cm. The S_{21} was calculated for each of 12 displacement steps from the original position.

Figure 4.4 shows the magnitude of the forward transmission coefficient S_{21}. This coefficient corresponds to the signal transmitted from the antenna inside the capsule, located at one of the sample positions inside the small intestine, to one of the receivers on the body surface (in this case receiver Rx1). As can be seen on figure, changes in the angles α and β have a direct impact on the magnitude of S_{21}, and in turn the received signal strength at the receiver Rx1. This observation has been investigated further to see if it can be used to reliably estimate the values of α and β.

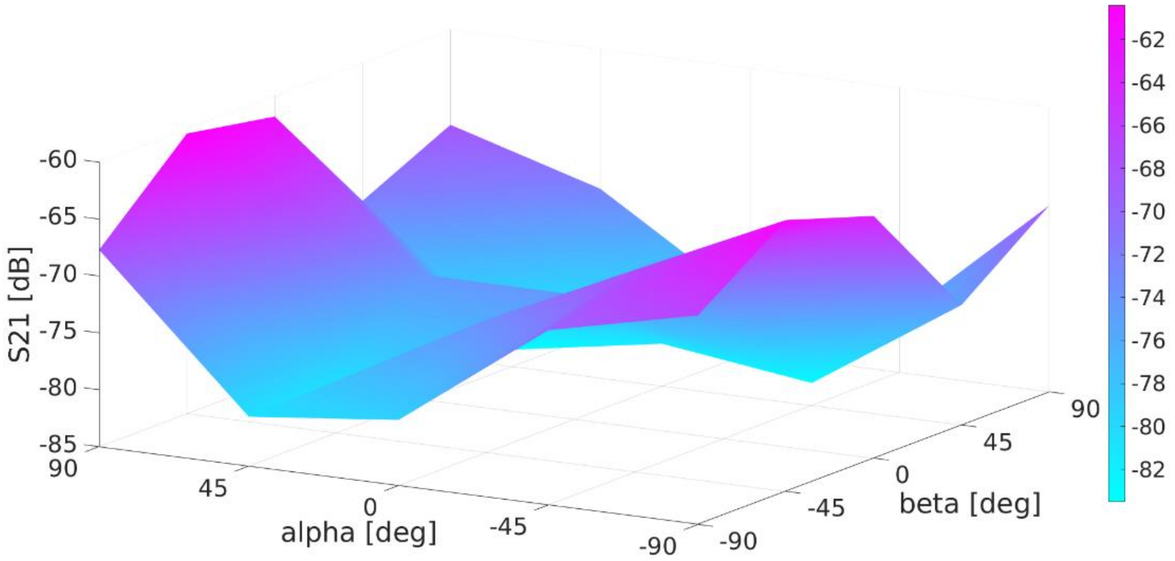

Figure 4.4: Magnitude of S_{21} at receiver Rx1 versus orientation angles α and β

4.3. Orientation Analysis and Estimation

For L number of receivers that are located on the abdomen area of the body model, as shown in Figure 2.1, vector $\vec{S}_{21}^{\alpha,\beta,\bar{P}_k}$ can be defined as:

$$\vec{S}_{21}^{\alpha,\beta,\bar{P}_k} = \left[\vec{S}_{21}^{\alpha,\beta,\bar{P}_k}(i)\right] \qquad i = 1, 2, \ldots, L$$

Where $\vec{S}_{21}^{\alpha,\beta,\bar{P}_k}$(i) represents the complex forward transmission coefficient (S_{21}) between the transmitter antenna inside the capsule and receiver 'i'. The capsule is located at a given position $\bar{P}_k = (x_k, y_k, z_k)$ inside the small intestine and its direction is specified by angles α and β.

The correlation coefficient ρ can also be defined as the following:

$$\rho^{\alpha,\beta,\bar{P}_k}(m,n,j) = \sum_{i=1}^{14} \frac{S_{21}^{\alpha,\beta,\bar{P}_k}(i) \cdot S_{21}^{(\alpha+m\Delta),(\beta+n\Delta),\bar{P}_{k+j}}(i)}{\left\|\vec{S}_{21}^{\alpha,\beta,\bar{P}_k}\right\| \cdot \left\|\vec{S}_{21}^{(\alpha+m\Delta),(\beta+n\Delta),\bar{P}_{k+j}}\right\|}$$

Where Δ is the unit angular step that is used to change α and β; and

$$m,n = 0, \pm 1, \pm 2, \dots \quad \text{and} \quad j = 0, 1, 2, \dots$$

The correlation coefficient defines the cross-correlation between the S_{21} vector at position $\bar{P}_k$ characterized by orientation α and β, and another S_{21} vector at position $\bar{P}_{k+j}$ with the orientation values of α + mΔ and β + nΔ.

High values of this coefficient suggest a certain level of similarity between the two capsule positions or orientations being compared. Therefore, if there is a previous knowledge about the S_{21} vector at a reference location, it can be possible to obtain some information regarding orientation α, β and $\bar{P}_k$ by analyzing the values of this coefficient.

The correlation matrix $R_{\bar{P}_k}$ at position $\bar{P}_k$ and orientation values α and β can be defined as:

$$R_{\bar{P}_k}(\alpha,\beta) = \left[\rho^{\alpha,\beta,\bar{P}_k}(m,n,0)\right] \quad m,n = 0, \pm 1, \pm 2, \dots$$

Then, the orientation of the capsule can be estimated by:

$$\left(\hat{\alpha},\hat{\beta}\right) = Argmax_{(\alpha,\beta)}\left[R_{\bar{P}_k}(\alpha,\beta)\right] \tag{4.1}$$

Where $\left(\hat{\alpha},\hat{\beta}\right)$ is the estimate value of the angles α, β.

How far can a capsule move from the reference position before the similarities among S21 vectors disappear was also studied. The correlation vector R_{α_0,β_0} at position $\bar{P}_k$ and orientation α_0, β_0 is defined as follows:

$$R_{\alpha_0\beta_0}(\bar{P}_k) = \left[\rho^{\alpha_0,\beta_0,\bar{P}_k}(0,0,j)\right] \quad j = 0, 1, 2, \dots$$

$\bar{P}_{k+j}$ indicates a sequence of capsule displacement along the centerline of the small intestine. While these displacements can be defined with equal increments, it is worth to note that the 3D distance from the reference position may not always linearly increase. This is due to the complex shape of the small intestine centerline in 3D space. There may even be cases where the 3D distance decreases while the linear displacements along the centerline increase. By examining the highest value of the correlation vector mentioned above, it is possible to obtain the maximum displacement of the capsule. This maximum correlation represents the displacement limit at which equation (4.1) (or some other alternative approaches) can still be effectively used to estimate the capsule orientation.

Another approach that is commonly used in other applications to evaluate the similarity between two vectors is the Minkowski distance. This methodology can also be applied here to estimate the values of α, β as follows.

Define Minkowski distance of order 'r' among two S_{21} vectors as:

$$d_{L_r}\left(\vec{S}_{21}^{\alpha_1,\beta_1,\bar{P}_k}, \vec{S}_{21}^{\alpha_2,\beta_2,\bar{P}_k}\right) = \left(\sum_{i} \left|S_{21}^{\alpha_1,\beta_1,\bar{P}_k}(i) - S_{21}^{\alpha_2,\beta_2,\bar{P}_k}(i)\right|\right)^{1/r}$$

Then, $(\hat{\alpha}, \hat{\beta})$ is obtained through the following equation:

$$(\hat{\alpha}, \hat{\beta}) = Argmin_{(\alpha,\beta)} d_{L_r}\left(\vec{S}_{21}^{\alpha,\beta,\bar{P}_k}, \vec{S}_{21}^{(\alpha_0+m\Delta),(\beta_0+n\Delta),\bar{P}_k}\right) \qquad (4.2)$$

$$m, n = 0, \pm 1, \pm 2, \ldots$$

This methodology was also implemented and compared with the correlation coefficient approach to evaluate its performance and effectiveness. The results are presented and discussed in the next section.

4.4. Simulation Results

As mentioned, simulations were performed for three different capsule sample positions, changing orientation values α and β from -90° to 90° in 45° increments. Given a sample capsule position inside the small intestine i.e. $\bar{P}_k$, the sample correlation coefficient vectors $\left[\rho^{\alpha_0,\beta_0,\bar{P}_k}(m,0,0)\right]$ $m = -2,-1,0,1,2$ and $\left[\rho^{\alpha_0,\beta_0,\bar{P}_k}(0,n,0)\right]$ $n = -2,-1,0,1,2$ highlight the sensitivity of the S_{21} vector with respect to α, β angular rotations. For $\Delta = 45°$, $L = 14$, $\alpha_0 = 0$ and $\beta_0 = 0$, example of correlation coefficient vector is below.

$$\left[\rho^{0,45^\circ,\overline{P}_k}(m,0,0)\right] = \begin{bmatrix}1.00 & 0.84 & 0.81 & 0.52 & 0.82\end{bmatrix}$$

$$\left[\rho^{45^\circ,0,\overline{P}_k}(0,n,0)\right] = \begin{bmatrix}1.00 & 0.77 & 0.70 & 0.19 & 0.74\end{bmatrix}$$

As observed from this example, the correlation coefficient is sensitive to rotations in α and β. This sensitivity can be expected by looking at the antenna pattern shown in Figure 4.1. Changes in the values of α or β will effectively change the direction where the null of the antenna is pointing. For a fixed value of $\alpha = 45°$, the correlation coefficient is decreasing as β changes from −90° to 45° in 45° increments. Similarly, when β is fixed at 45°, the correlation coefficient decreases as α changes from −90° to 45° in steps of 45°. As can be noticed, the coefficient experiences a sudden increase when α reaches 90° due to the symmetry in the antenna pattern. Moreover, if the center of the capsule is instead placed at the origin of the coordinate system shown in Figure 4.3, changing α from −90° to +90° while keeping β fixed would effectively flip the antenna in the same position. Therefore, a correlation coefficient with values close to 1 can be expected for 180° rotations of the antenna.

For this specific CE antenna used in simulations, the orientation of the null in its pattern is the same as the orientation of the camera inside the capsule. The direction of this null can be found by estimating the values of α and β, which in turn determines the orientation of the capsule itself. Following the methodology outlined in equation (4.1), a set of 10 different sample points was used to test estimation accuracy using correlation. Figures 4.5 and 4.6 show the real and estimated values of α and β.

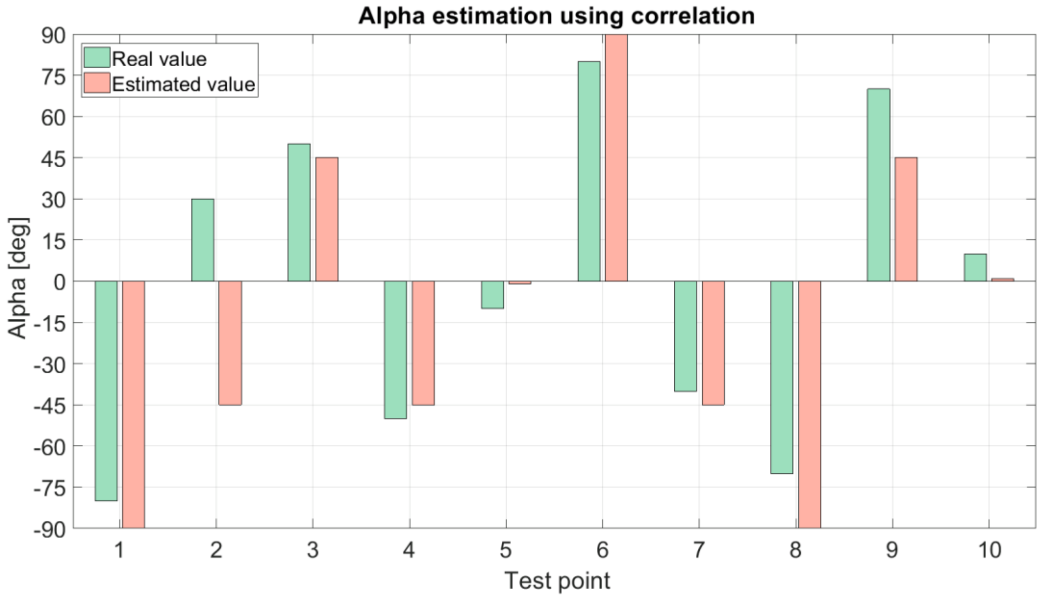

Figure 4.5: α versus $\hat{\alpha}$ using correlation coefficient

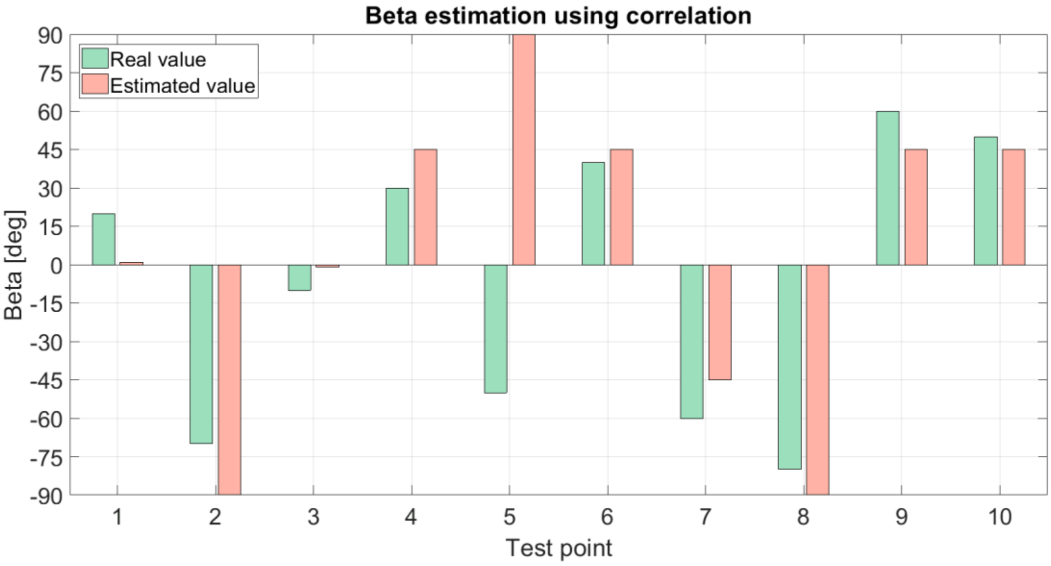

Figure 4.6: β versus $\hat{\beta}$ using correlation coefficient

As observed from the results, the estimated values of α and β were close to their actual values for 9 out of the 10 test scenarios. On average, the estimation error for both cases was 13.5°. Furthermore, following the Minkowski distance approach outlined in equation (4.2) and trying different orders, it was found that the 2nd order Minkowski distance results in more accurate performance for estimating α and β. Figures 4.7 and 4.8 show the comparison between the real and estimated α and β.

With the current number of test point samples, the correlation coefficient methodology showed a lower average error when compared to the Minkowski distance approach. The initial results presented here appear promising, however, more detailed studies along with the higher number of test scenarios are needed to better evaluate the performance of each methodology. Although, only the cross-correlation and Minkowski distances results were presented here, other methodologies that are based on similarity metrics such as Earth Mover and Hausdorff Distances are also planned to be implemented and evaluated in the future.

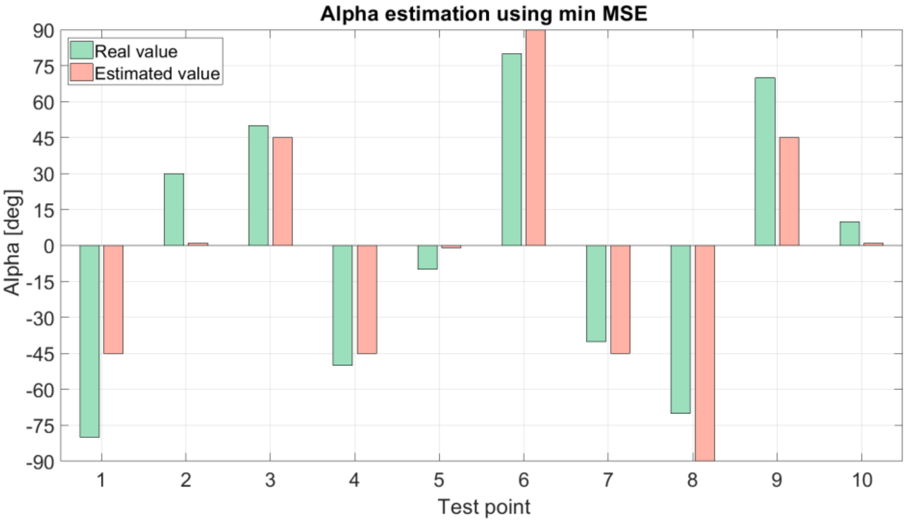

Figure 4.7: α versus $\hat{\alpha}$ using Minkowski distance of order 2

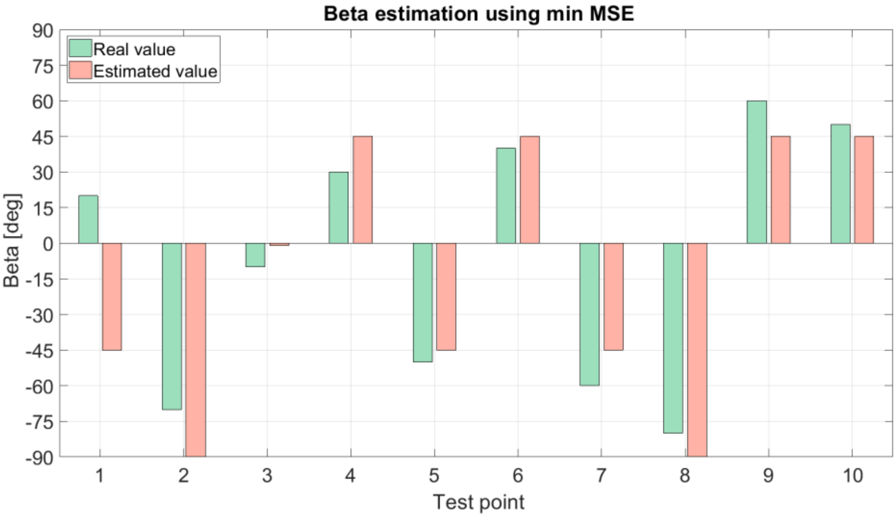

Figure 4.8: β versus $\hat{\beta}$ using Minkowski distance of order 2

Lastly, considering a displacement step of 0.25 cm, the correlation coefficient of the S_{21} vector, representing the correlation between different positions of the capsule, was also studied. The correlation coefficient was calculated for a range of values from 1 to 12, corresponding to different sample positions $\bar{P}_k$ (i.e., $R_{\alpha_0\beta_0}(\bar{P}_k)$ for $j = 1, 2, \dots, 12$). The obtained results for 3 different sample positions $\bar{P}_k$ are visually presented in Figure 4.9.

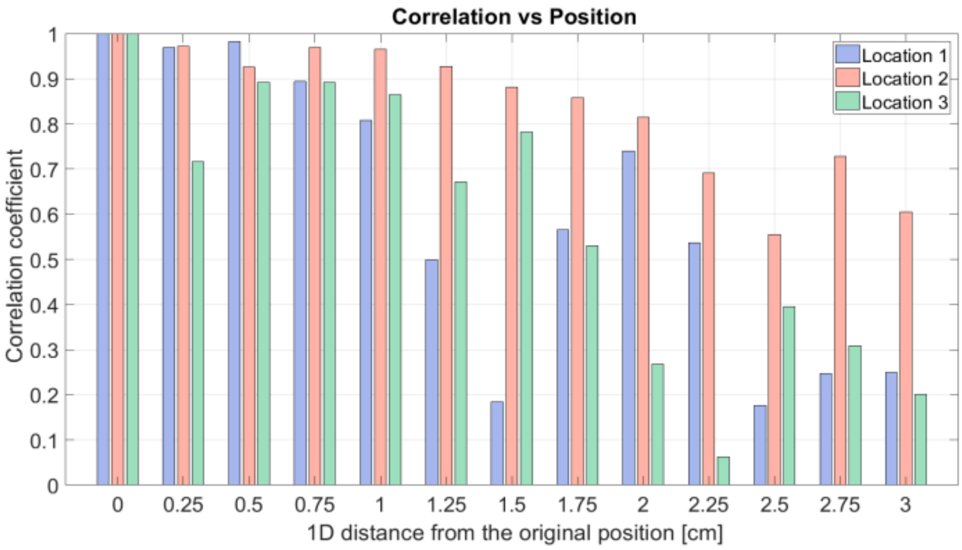

Figure 4.9: Correlation coefficient variation versus capsule displacement along the centerline

The behavior of these correlation coefficients will depend on two main factors: the initial position of the capsule, and the geometrical shape of the GI tract, specifically the centerline, around that particular location. As previously mentioned, the displacement of the capsule is done in linear steps of 0.25 cm along the centerline and without any changes to the angles α and β. However, the 3D direct distance between the new and the initial locations may not necessarily follow an increasing trend which means there can be some capsule displacement steps where the coefficient value increases with increasing displacement. Table 4.1 shows the difference in 1D distance and 3D direct distance displacements for one of the capsule sample locations (i.e., location 1). As it can be seen, increasing the capsule displacement from 1.5 cm to 1.75 cm, the 3D direct distance decreases which causes the correlation coefficient to increase. The same trend happens again for displacement from 1.75 cm to 2 cm, with correlation coefficient increasing from 0.57 to 0.74.

Table 4.1: 1D distance displacement, 3D distance displacement, and correlation coefficient values for one of the sample capsule locations

1D distance [cm]	***3D distance [cm]***	***Correlation coefficient***
0	0	0
0.25	0.27	0.97
0.5	0.42	0.98
0.75	0.64	0.89
1.0	0.9	0.81
1.25	1.16	0.5
1.5	1.28	0.18
1.75	1.04	0.57
2.0	0.82	0.74
2.25	1.0	0.54
2.5	1.2	0.18
2.75	1.42	0.25
3	1.27	0.25

Looking at the results presented in Figure 4.9, it can be concluded that a correlation coefficient of approximately 70% is maintained for distances of at least one centimeter around the original location of the capsule. These results imply that, despite the displacement, there still remains a solid degree of correlation between the capsules at different positions. Since capsule moves through the GI tract slowly and in short intervals, these findings offer useful knowledge for potential advancements in the field of location estimation for the CE and offer foundation for future investigations.

CHAPTER 5
Human Body Communication

As mentioned in the introduction chapter, Human Body Communication (HBC) is another wireless communication technology included in the IEEE 802.15.6 standard. In HBC, the human body acts as a communication channel between a transmitting and receiving electrodes placed on the surface of the skin. Information signal is transferred through the channel using capacitive or galvanic coupling between the electrodes. In capacitive coupling, a signal is delivered by forming an electric field around the human body induced by the transmitter electrode. Even with a weak electric field, the human body can act as a signal guide and capacitively couples the transmitting and receiving electrodes. The return path from the receiver electrode to the transmitter electrode is established through the environment. Very low complexity and energy consumption are among the reasons that make this technology attractive for wearable or implantable devices.

The first prototype HBC system was reported by T. G. Zimmerman in 1995 [31]. Since then, there have been several studies to investigate and model the mechanism of data transmission through the human body and the resulting communication channel. These studies are typically conducted in the form of measurement campaigns considering different scenarios. However, as the measurement results are highly dependent on the experimental conditions and setup such as type of the electrodes, type of instruments used, electrical grounding, electrode-impedance matching, electrodes' position on the body or even body posture, there are discrepancies observed across these studies [36]. The common element in most of the results published in the past several years is the bandpass shape of the channel attenuation in HBC with an approximate passband of 1-100 MHz. As pointed out earlier, depending on the instrumentation or methodology that is used for channel measurement, the frequency associated with the peak channel response within the passband could vary from 40 MHz to 70 MHz. Variations are also observed on the average magnitude of the forward transmission coefficient. This is due to the specifics of the parasitic return path in the HBC system.

To capture the fundamental concept of the HBC operation, and avoid discrepancies caused by different measurements processes, scenarios, etc., a simple parametric FEM-based model has been developed in this research. The parameters of this model can be adjusted to emulate a specific measurement scenario. Therefore, the model can be conveniently used for further studies on HBC technology, for example, to investigate the performance of different electrode types or evaluate the system performance for a given application. Finally, such a FEM-based model can be extended to study the implant HBC channel where physical measurements are no longer possible. Details of this model are described in the rest of this chapter.

5.1. A Parametric FEM-based Model

Modeling of an HBC channel is a challenging task due to the many parameters that can possibly affect the characteristics of the communication link. Among those are size and shape of the electrodes, locations and the distance between the Tx/Rx electrodes, separation between the signal and ground plates of each electrode, body posture, dielectric properties of the human tissues that are in contact with the electrodes and possibly the environment surrounding the human body.

For the HBC study [102], the 3D computational body model for the developed immersive platform to study wireless channels in body area networks, has been augmented with additional body surface layers (representing skin and fat) that fit over the exterior body mesh. The fat layer has adjustable thickness to represent a fit, an average, or an overweight person. Therefore, the potential impact of the fat layer on the forward path of an HBC channel can also be studied. Using this custom 3D computational human body model, the impact of the distance of the electrodes, size of the electrodes, location of the electrodes on the body, size of the ground plate, and distance between the signal and ground plates on the RF propagation can been studied.

5.1.1. Modeling the Electrodes

The electrodes were modeled as two metal plates representing capacitive coupling HBC. One electrode plate (i.e., signal plate) is in contact with the skin and the other plate is located with a certain distance away and directly facing the signal plate. To ensure full contact of the signal plate with the skin, whenever necessary, a small patch of skin tissue has been added directly underneath the plate. This guarantees that the surface of the signal plate and the skin are fully connected. Figure 5.1 shows an example of two electrodes placed on the right arm of the human body model. Size, plates separation, distance between the receiver/transmitter electrodes are all design variables; and therefore, the impact of each one of these parameters can be easily investigated with this computational model.

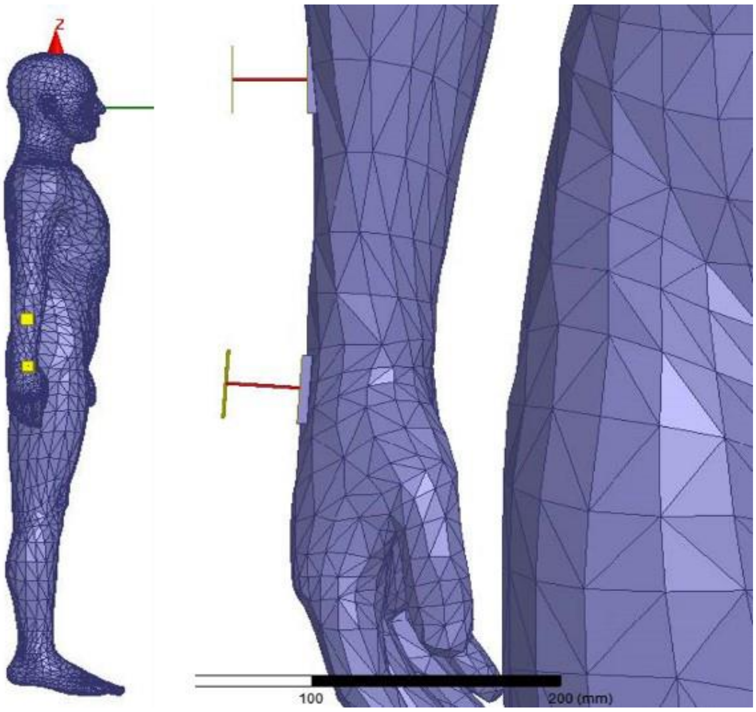

Figure 5.1: HBC electrodes on the computational body model

The biggest complexity in modeling the HBC channel is incorporating the impact of the parasitic return path and characteristic impedances of the electronic circuits generating the signal (or in case of physical measurement, parasitic of the probe PCB). In this FEM-based model, the coupling of the electrodes through the air (i.e., return path) is modeled by a capacitor (C_{Ret}). This is similar to the circuit or circuit-enabled models proposed in [41]. However, the capacitive return path has been implemented using RLC boundaries methodology. The signal leakage path between the electrode plates has also been modeled with capacitor C_L. The characteristic impedance of the source has been modeled by a cascade of resistor R_{Tx} and inductor L_{Tx}. These elements are schematically shown in Figure 5.2.

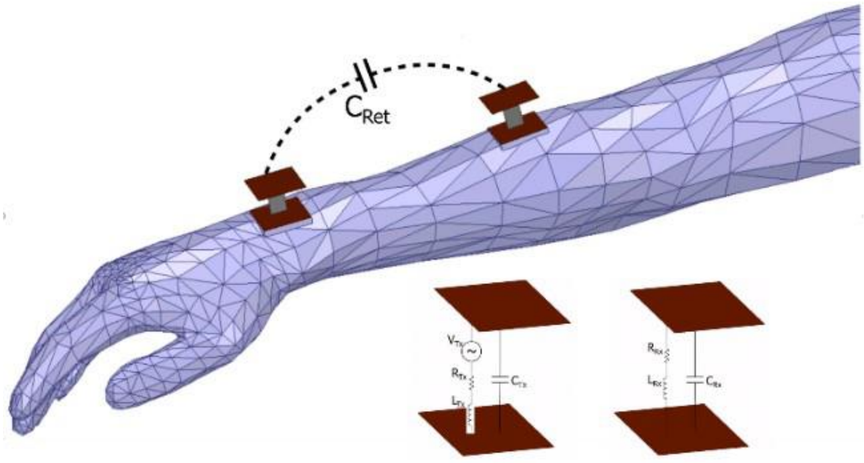

Figure 5.2: Electrodes and return path schematics

5.2. On-body HBC

Using ANSYS HFSS electromagnetic solver, a variety of different quantities such as the magnitudes of the electric field (inside, on the surface and outside of the body) and the scattering parameters (e.g., S_{21}) between the two electrodes can be calculated. For example, Figure 5.3 shows the underlying concept of the HBC operation by displaying the electric field distribution. Figure 5.3(a) shows the distribution of the magnitude of the electric field when the transmitting electrode is not in contact with the human body (i.e., operating in the air). On the other hand, when the electrode is placed on the human arm (as seen in Figure 5.3(b)), the electric field extends over the entire body surface. This ensures much higher received signal strength, and therefore, a better communication channel between the two electrodes. A signal frequency of 50 MHz has been used for the result shown in Figure 5.3.

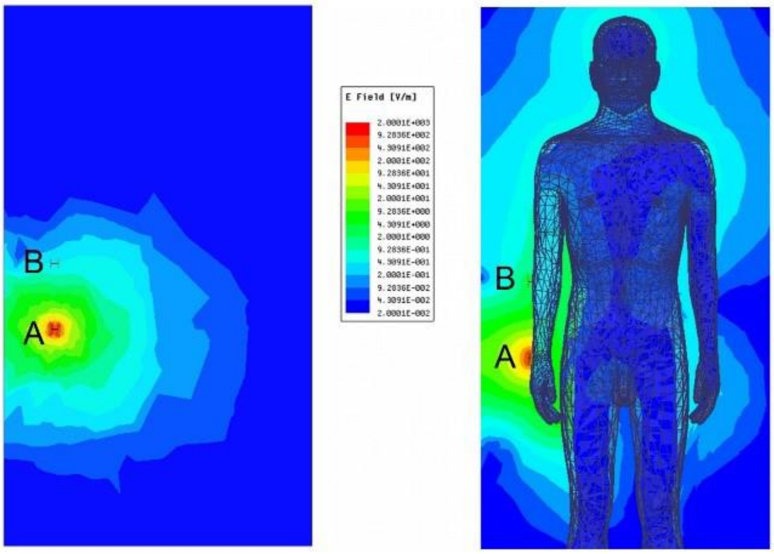

(a) *(b)*

Figure 5.3: Electric field distribution around the transmitter electrode (a) without the human body, (b) with the human body

The frequency range of interest in HBC is typically 1-100 MHz. Higher frequencies could result in the human body acting as an antenna and are also susceptible to external radiation [59]. Therefore, for frequencies higher than 100 MHz, significant channel variation and lower efficiency of the communication link can be expected. Using the simulation platform discussed in the previous section, the HBC channel attenuation can be measured by the forward transmission coefficient S_{21} for various scenarios. As mentioned earlier, limited measurement results in the literature indicate a bandpass profile with varying location of the peak frequency. The bandpass profile is mostly influenced by the capacitive leakage path as well as the parasitic inductance L_{Tx}.

To show the impact of these parameters, forward transmission coefficient S_{21} has been simulated for the scenario described in Figure 5.1 with a 15 cm distance between the two electrodes on the arm. Figure 5.4 displays the simulation results for various values of the capacitive return path (C_{Ret}) when L_{Tx}=225 nH. Similarly, Figure 5.5 reflects the impact of varying L_{Tx} while C_{Ret} is fixed. As observed, the bandpass profile shape and values for the S_{21} can be tuned and optimized to match the physical measurement results published in the literature. In fact, as presented in Figure 5.6, for 15 cm separation between the electrodes, C_{Ret}=5 pF, L_{Tx}=225 nH and C_L=35 pF, the simulation results match quite well with the reported physical measurement results in [42–45]. The source and load impedances were assumed to be 50 Ohms. The S_{21} results for distances of 30 cm and 45 cm as the receiver electrode was moved further up the arm and closer to the shoulder were also investigated. The same values for the parasitic capacitance and inductance resulted in the best match with the reported measurements in [43].

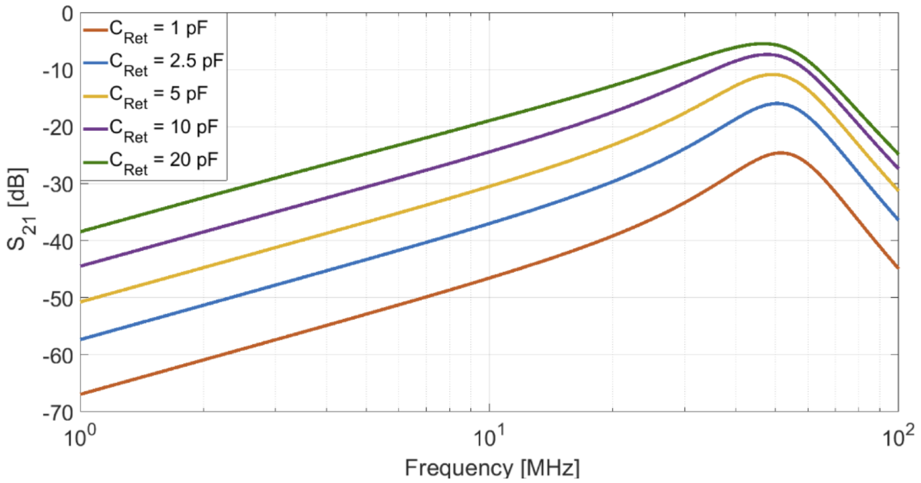

Figure 5.4: Forward transmission coefficient S_{21} for various C_{Ret} values

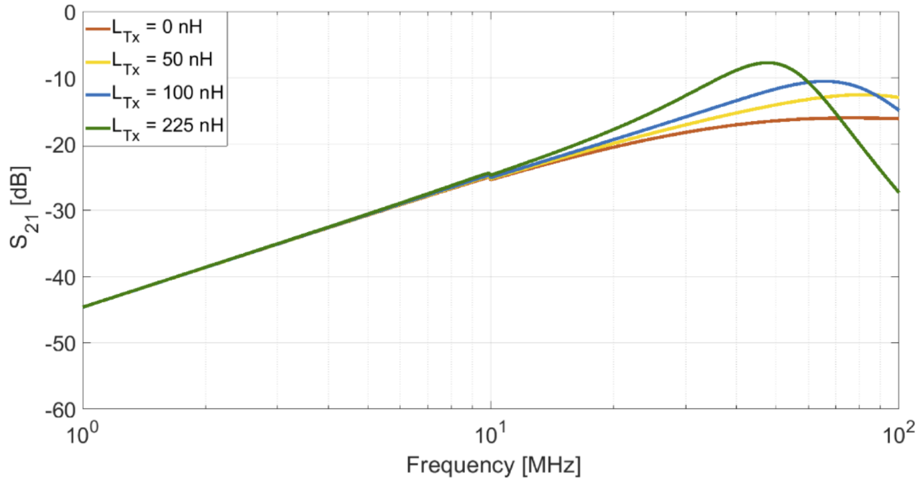

Figure 5.5: Forward transmission coefficient S_{21} for various parasitic inductance values L_{Tx}

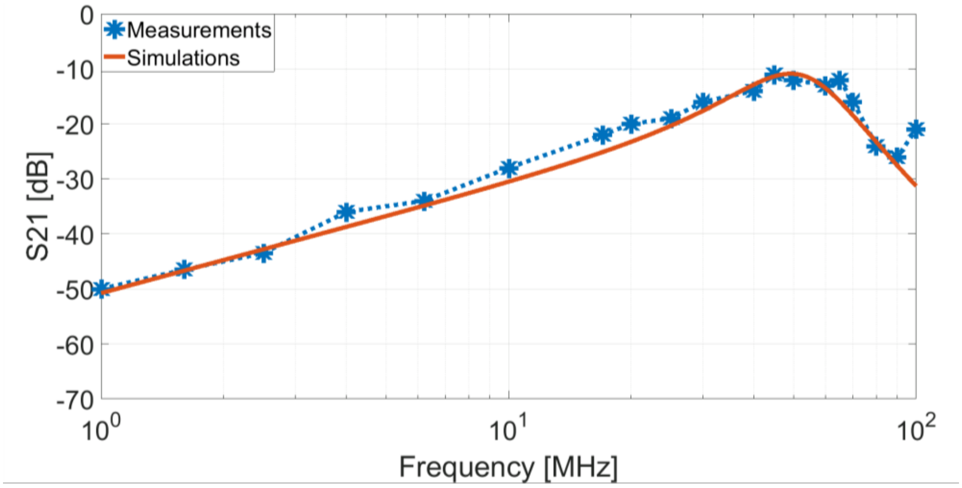

Figure 5.6: HBC simulation result vs physical measurements for 15 cm electrode separation

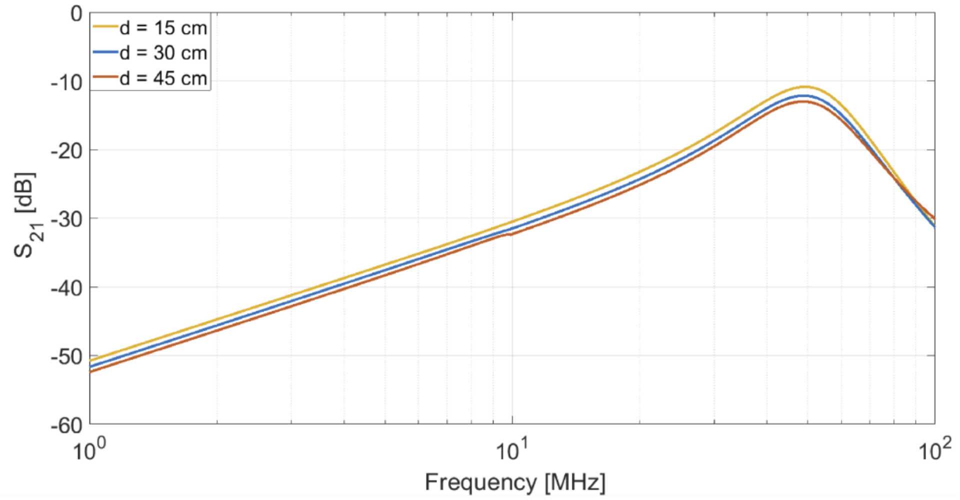

Figure 5.7: Forward transmission coefficient S_{21} for various electrodes distances

Looking at the results for electrode separations of 15, 30 and 45 cm (Figure 5.7), a slight degradation of the S_{21} versus distance is observed. However, the parasitic capacitance representing the return path seems to be the same. The S_{21} degradation is due to the higher attenuation of the forward path, i.e., the path through the body. For the three scenarios considered so far, the forward and return path distances are approximately the same as the receiver electrode is moved away from the transmitter along the straight human arm. It is worth noting that there could be scenarios where the forward and return path distances are quite different, for example, when the electrodes are located on the left and right wrists, and the arms are held straight down along the body (or even close to each other in front of the body).

Currently, there are no results in the literature that highlights the impact of this discrepancy between forward and return path distances. It is speculated that the parasitic capacitance could be a function of the return path distance. For example, if the electrodes are located on the separate wrists, the magnitude of S_{21} will change as the person under experiment move their hands closer or farther away from each other. Also, another uncertainty regarding the forward path distance is whether this distance is considered as the shortest path through the human body (i.e., in-body distance) or as the path along the body surface. For example, consider a scenario with two HBC electrodes, one located on the chest area and the other on the back side of the body. Depending on how the electric field is distributed, the length of the forward path could be the straight line through the body connecting the electrodes or the distance around the body surface separating the two electrodes. To better understand this issue, the impact of the return path needs to be eliminated first. This has been accomplished by shortcircuiting the ground plates of the electrodes with a perfect conductor. For the same scenario as in Figure 5.1 the resulting S_{21} versus frequency, which is now representing only the attenuation through the forward path, is shown in Figure 5.8.

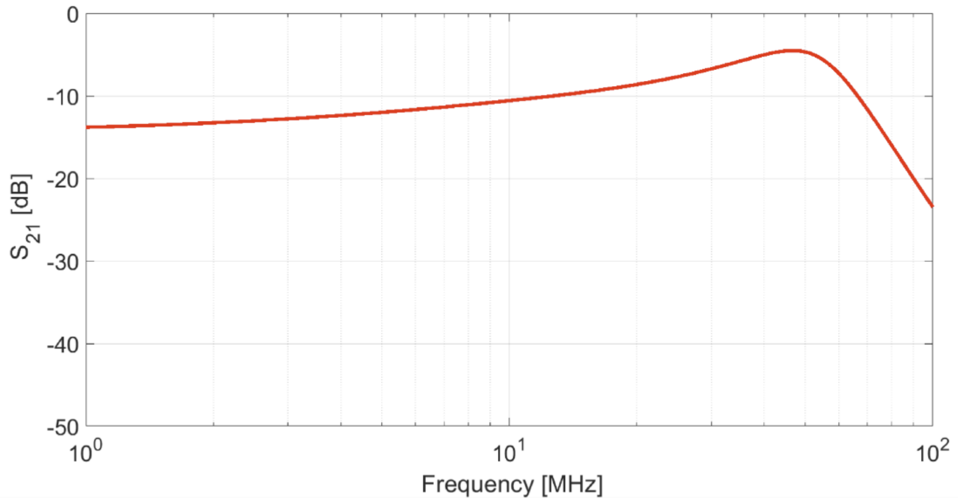

Figure 5.8: Forward path attenuation for the HBC scenario with 15 cm electrode separation

As observed, the body seems to be a uniform attenuator (for frequencies below 100 MHz) with approximately 10-15 dB loss when the distance between Tx and Rx electrodes is about 15 cm. This level of attenuation was also observed through physical measurement in [41].

As mentioned earlier, the 3D immersive platform used for this study allows researchers to visualize the distribution of electric field for any scenarios. For the scenario where electrodes are placed on the front and back side of the torso, visualization of the electric field determined that the forward path distance is actually the distance around the torso and not through the body (Figure 5.9).

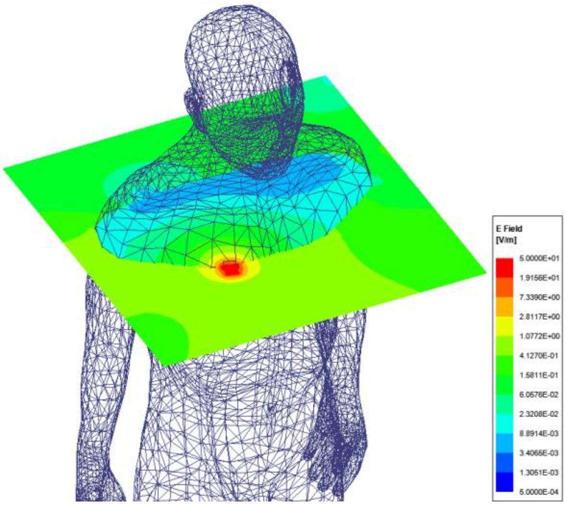

Figure 5.9: In-body electric field distribution for HBC scenario with electrodes on the front and back side of the torso

The material properties of the body tissues that are along the forward path of the HBC channel can also impact the signal attenuation. To observe this, a simulation using two body models representing a fit versus obese person was conducted. The electrodes were placed on the stomach area where a heavier concentration of fat exists. The electrode separation was chosen to be 20 cm. The S_{21} for the two human body models are shown in Figure 5.10. The result indicates higher attenuation for the obese person, which can be explained by the lower conductivity of the fat tissue versus muscle for the frequency range of 10 to 100 MHz.

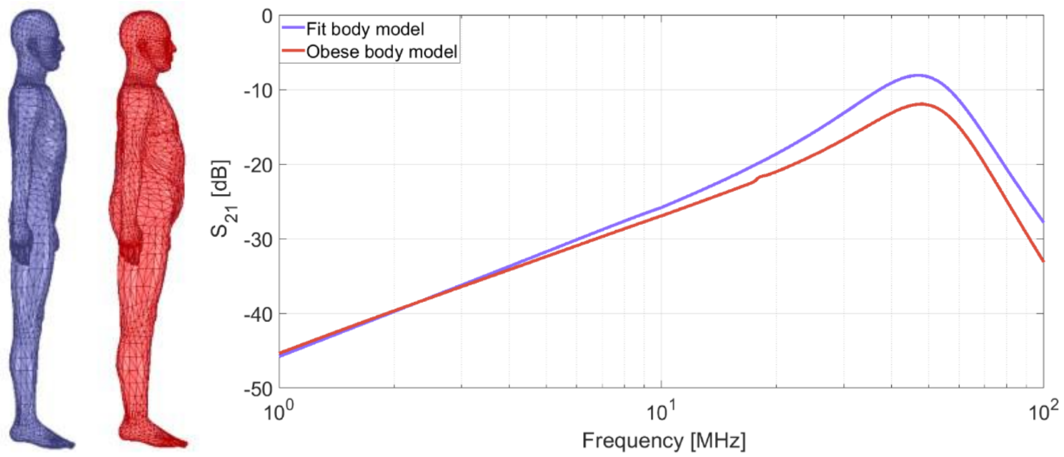

Figure 5.10: Forward transmission coefficient for different body shapes

5.3. In-body HBC

As mentioned in the introduction chapter, there are limited studies on using HBC for implants or ingestible electronics applications (i.e., in-body HBC) in the literature. Most of the earlier studies focused on galvanic HBC as it was assumed that capacitive HBC is not applicable for communication between implants. The assumption was due to the complexity in establishing the return path inside the body environment. However, authors in [51] showed that it is possible to achieve capacitive coupling inside the body if the ground plate in the electrode is isolated from the human tissues. Using the capacitive coupling for in-body HBC it is possible to achieve lower channel attenuation. Moreover, in comparison to galvanic coupling, the distance between transmitter and receiver electrodes has minimal impact on the signal attenuation in capacitive HBC.

Conducting physical experiments with implantable devices inside the human body are nearly impossible; therefore, channel measurements for in-body HBC are usually performed using liquid or tissue phantoms, or computer simulations. Liquid phantoms that mimic electrical properties of the human body tissues are developed by combining chemical substances with water to adjust conductivity and relative permittivity of the solution. However, since the dielectric properties of the body tissues are frequency-dependent, liquid phantom are typically used at a specific frequency (or a narrow frequency band) where the phantom has been designed for. Moreover, liquid phantoms are prone to evaporation over time, so the electrical properties of the liquid need to be checked and adjusted if the duration of the measurement process is long.

Authors in [54] emulated an in-body to on-body capacitive HBC channel by placing the transmitter electrode inside the axilla region (i.e., armpit) and tightly covering the electrode by the arm. For the transmitter electrodes they used EEG electrode attached to the bottom side of a PCB board. Copper side of a PCB was used as a transmitter ground electrode and was covered in hot glue to ensure insulation from signal electrode and body tissues. Receiver signal electrode was a standard self-adhesive Ag/AgCl electrode (Blue Sensor N) connected to the skin and a 2 cm x 2 cm copper foil as a ground electrode. The ground copper electrode was placed on a 1 mm thick plastic housing, 2 cm above the Ag/AgCl electrode, and oriented towards the environment. During the measurement process, the person was standing and held two still positions with transmitter electrodes placed under the left armpit and kept in position, while receiver electrodes were placed on 13 positions on the body. Measurements were performed for the 100 kHz to 100 MHz frequency range using a network analyzer and decoupling transformers. The results showed that up to 1.5 MHz the gain measured in all receiver positions on torso and arms for both channels differs by at most 1.5 dB. Then, the gain increased with 20 dB per decade. At higher frequencies, the highest gain was measured for the lowest distance from the transmitter. These preliminary results also showed that covering transmitter electrode with a small amount of tissue decreases measured gain up to 4 dB compared to the body surface measurements (on-body to on-body HBC channels with the electrodes placed in the same positions). In [55] authors presented a characterization of capacitive implant HBC (i.e., in-body to on-body channel) using liquid phantom measurements. Measurements were performed using proprietary developed battery-powered devices (transmitter and receiver) for both in-body to on-body and on-body to in-body scenarios. During the measurements, two 1 cm by 1 cm copper electrodes of the in-body device were always immersed in the phantom and separated by 2 cm. The signal electrode was in contact with the phantom, while the ground electrode was insulated by a plastic layer. Two sets of electrodes were evaluated for the on-body device. First, a standard Ag/AgCl medical electrode was used as the signal electrode and a copper electrode was used as the ground electrode. In the second set of measurements, the device was connected to a copper electrode as the signal electrode and an insulated copper electrode as the ground electrode, mirroring the electrode setup for the in-body device. The results showed very small variation in attenuation as a function of the distance between the electrodes and highlighted the importance of minimizing the bandpass profile effect caused by the long cables. Also, insulating the ground electrode affected the measured attenuation by about 6 dBm.

The results of limited studies on implant or in-body to on-body HBC in literature are always dependent on the measurement conditions, especially the type and size of electrodes, and separation between the electrode plates. In the FEM-based model, the values of capacitive leakage path C_{LTx}, parasitic inductance L_{Tx} and capacitive return path C_{Ret} will also change by placing the transmitter electrode inside the muscle tissue, effectively changing the environment between two metal plates of the electrode. To study the impact of these parameters on in-body to on-body propagation, forward transmission coefficient S_{21} between the two electrodes has been simulated for different electrode plate sizes and various values of parasitic elements using the developed parametric FEM-based models. The simulations were first performed using the computational model of the liquid phantom, and then using the immersive platform with a 3D computational body model. More details are provided in the following subsections. By choosing the appropriate values of the parasitic elements, the simulation results can be tuned to match the experimental measurements reported in the literature.

5.3.1. In-body to On-body HBC Simulations Using the Computational Model of a Liquid Phantom

A computational model emulating the liquid phantom used in [55] was created in Ansys HFSS software. The plastic container (Figure 5.11) was modeled as a 1.5mm thick polyethylene filled with material with identical dielectric properties as human muscle tissue. The internal volume of the phantom is 39 cm x 35 cm x 18 cm. While liquid phantom can only be used for measurements at a specific frequency or a narrow frequency band, there are no such restrictions in computer simulations with the computational model. Simulations were performed for 10 MHz to 100 MHz frequency range. Relative permittivity and dielectric loss tangent of the muscle tissue were modeled using a frequency-dependent multipole Debye model. The electrodes were modeled as a two metal plates representing capacitive coupling HBC, with transmitter electrode placed inside the muscle tissue and the on-body electrode placed on the outside surface of the container. The ground plate of the transmitter electrode was covered by a thin layer of glue to insulate it from the muscle tissue. The signal leakage path between the electrode plates has been modeled with capacitor C_{Tx} and the characteristic impedance of the source was modeled by a cascade of resistor R_{Tx} and inductor L_{Tx} (C_{Rx}, R_{Rx}, and L_{Rx} for receiver electrode). The coupling of the electrodes through the air (i.e., return path) is modeled by a capacitor C_{Ret}.

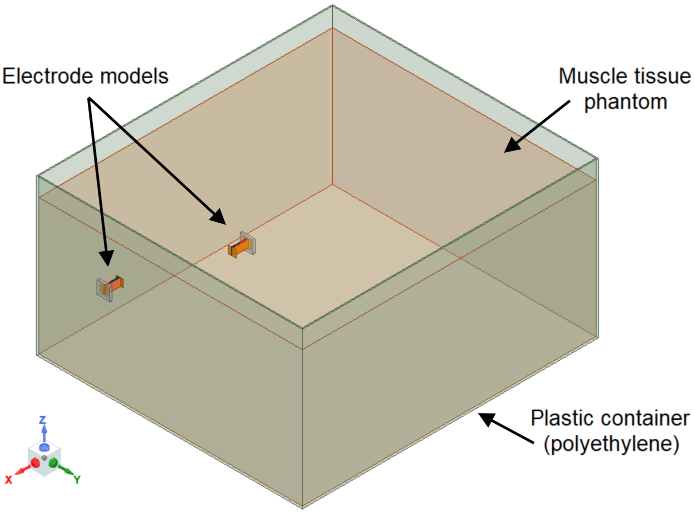

Figure 5.11: Computational model of the liquid phantom and electrodes

1) 2 cm × 2 cm electrodes

First set of simulations used the same electrode size (2 cm × 2 cm) as for on-body simulation scenario from chapters 5.1. and 5.2. As the receiver electrode is on the container surface surrounded by air, the parasitic elements between the signal and ground copper plates of the receiver electrode are the same as the on-body scenario; $C_{Rx} = 35$ pF and $L_{Rx} = 225$ nH. However, it is expected that the values of parasitic elements will change for the transmitter electrode placed inside the muscle phantom container. The values of C_{Tx}, L_{Tx} and also return path C_{Ret} used in simulations are listed in Table 5.1. Forward transmission coefficient S_{21} for various C_{Ret} values is shown in Figure 5.12. Values of C_{Tx} and L_{Tx} are fixed at 10 pF and 25 nH respectively, and the distance between in-body and on-body electrodes is 15 cm.

Table 5.1: Parameter values used in simulations with 2 cm × 2 cm electrodes

***C**$_{Ret}$*	20 pF	30 pF	40 pF	50 pF	60 pF
***L**$_{Tx}$*	0 nH	25 nH	50 nH		
***C**$_{Tx}$*	10 pF	35 pF			

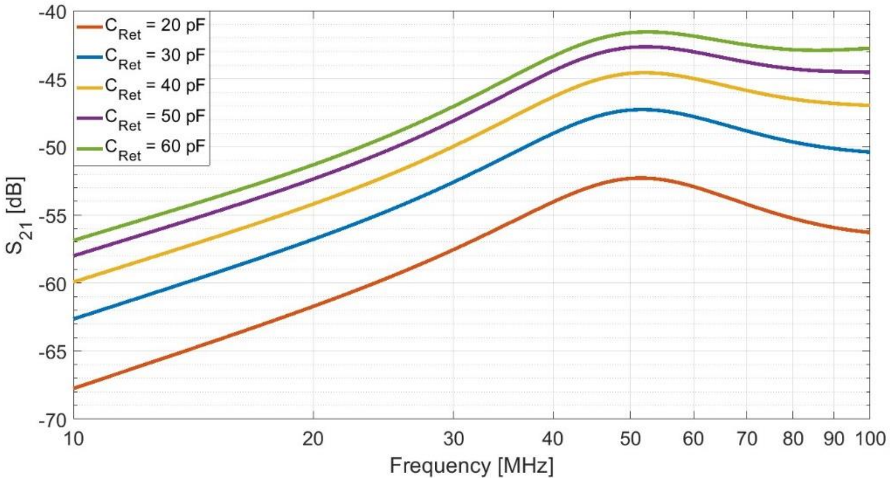

Figure 5.12: Forward transmission coefficient S_{21} for various C_{Ret} values

2) 1 cm × 1 cm electrodes

The simulations using the computational model of the liquid phantom were repeated using a smaller electrode plate (1 cm × 1 cm) and 2 cm distance between signal and ground plate of each electrode. The ground plate was covered in a thin layer of glue for isolation. The values for C_{Tx}, C_{Rx}, L_{Tx} and return path C_{Ret} used in simulations are listed in table below.

Table 5.2: Parameter values used in simulations with 1 cm × 1 cm electrodes

C_{Ret}	20 pF	30 pF	40 pF	50 pF	60 pF
L_{Tx}	0 nH	25 nH	50 nH	110 nH	
C_{Tx}	3 pF	10 pF	35 pF		
C_{Rx}	1 pF	10 pF	35 pF		

This simulation setup emulates the measurement setup using the liquid phantom in [54]. The measurements in [54] were performed at the following frequencies: 13.56 MHz, 21 MHz, 27.12 MHz, 40.68 MHz, 50 MHz, 62 MHz, 70 MHz, and 84 MHz. For 15 cm separation between electrodes, CRet = 40 pF, LTx = 25 nH, CTx = 10 pF, and CRx = 35 pF, the simulation results match well with the liquid phantom measurements (Figure 5.13). The slight discrepancy in the results is possibly due to the asymmetric measurement setup for the phantom measurements. The 47 cm long cable had to be used for in-body device which affected the phantom measurements. The authors highlighted the need to use battery-powered measuring devices to eliminate the impact of long cables and baluns on the measurement environment. On the other hand, computer simulations represent the ideal environment without any unwanted effects from the measurement equipment.

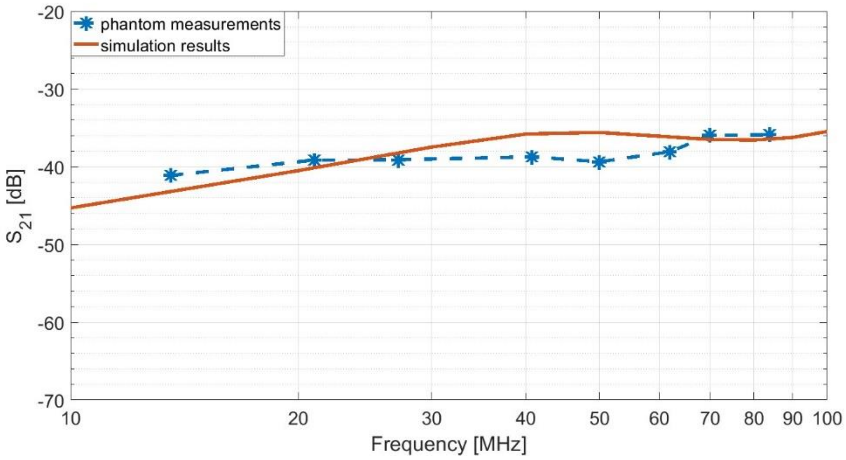

Figure 5.13: S_{21} comparison between simulation and phantom measurements

5.3.2. In-body to On-body HBC Simulations with Computational Human Body Model

Measurements of capacitive HBC implant channels in the literature are usually performed using battery-powered equipment with different human body phantoms, animal tissue phantoms, or using circuit models [51, 52, 57, 58]. As discussed earlier, authors in [54] emulated an in-body to on-body capacitive HBC channel by placing one electrode inside the axilla region (i.e., armpit) and tightly covering the electrode by the arm. The measurements scenario in [54] can be recreated using a computational human body model. The transmitter electrode is placed in approximately similar position (i.e., axilla region) while the receiver electrode is placed on the body surface as shown in Figure 5.14. The transmitter electrode is modeled using PEC (Perfect Electric Conductor) with 1 cm diameter size to emulate the EEG electrode attached to the bottom side of a 1.5 cm × 1.5 cm PCB board. On-body receiver electrode is modeled similar to the electrode (2 cm × 2 cm) used in simulation scenarios in chapters 5.1. and 5.2. For 15 cm separation between electrodes, C_{Ret} = 160 pF, L_{Tx} = 225 nH, C_{Tx} = 35 pF, and C_{Rx} = 35 pF, the simulation results match well with the results in [54]. The comparison is shown in Figure 5.15.

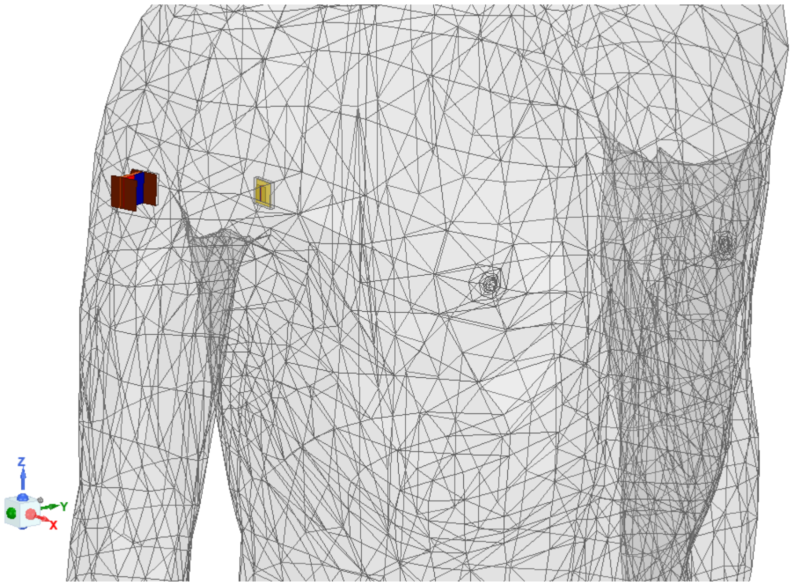

Figure 5.14: Simulation setup using computational human body model

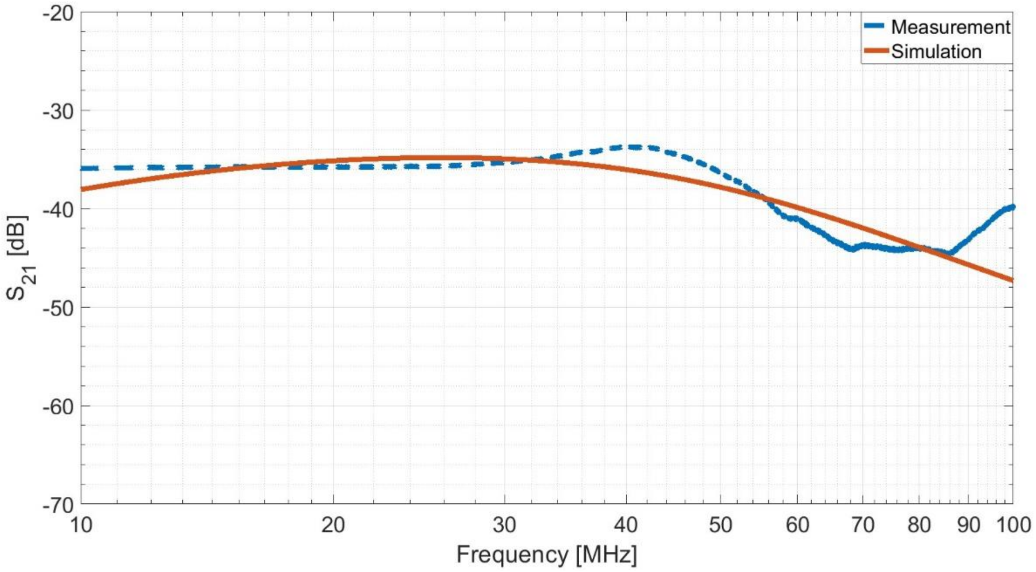

Figure 5.15: S_{21} comparison between simulation results and physical measurements

The flexible and customizable simulation model presented here allows researchers to study the HBC channel by considering variable electrode size, plate separation, and placement on the body. It will also enable designing virtual experiments to better understand the impact of variable return path distance for a fixed forward path through the human body. The S_{21} results for several scenarios presented in this study match the HBC channel attenuations reported in the literature with appropriate adjustment of the model parameters.

CHAPTER 6
Concluding Remarks

Since its invention in the early 1990s the technology behind capsule endoscopy has been making fast progress. The emergence of high-resolution miniature video cameras along with other microsensor technology have increased the data rate and power consumption requirements for the next generation of these capsules. High data rate transmission along with other features have made the Ultra-Wideband (UWB) technology an attractive candidate for wireless communication with the capsule endoscope.

An innovative 3D immersive platform including a detailed computational human body and gastrointestinal tract model has been presented in this thesis. The platform allows for an in-depth study of the wireless propagation channel between a capsule endoscope and on-body receivers at UWB frequencies. A statistical pathloss model including a fading component that more effectively captures the impact of various body tissues as well as the antenna orientation for the 3.1 GHz to 4.1 GHz frequency range has been obtained. It has been shown that this frequency range is more feasible for communication with a capsule endoscope within the unlicensed UWB spectrum. This is the first study that comprehensively captures the entire length of the small intestine while considering realistic positions for capsule along its natural trajectory in order to conduct virtual measurements.

Using realistic and practical antennas, a detailed computational human body with GI tract model, and more pragmatic antenna positions for the measurements, the received signal variations caused by the imperfect i.e., non-isotropic capsule antenna pattern were captured as part of the fading component in the presented model. To investigate the accuracy of the pathloss model obtained through virtual measurements using the computational platform, a liquid phantom measurement system was also emulated using the same platform. It was observed that the frequency dependent pathloss exponent obtained by the computational experiment closely matches the one obtained through physical experiment. It should be noted that variations of the electromagnetic properties of the environment surrounding the capsule due to the different body types (e.g., bodies with different body mass index) could lead to further variations of the signal strength at the on-body receiver. Modeling these variations require further virtual experimentation with a sequence of body models representing different body types, and/or 4D dynamic body models. The presented pathloss information can help with more accurate link budget and better understanding of the feasible communication range as the capsule traverses the small intestine. This knowledge can also assist in identifying the minimum number and optimal placements of the on-body receivers to ensure reliable signal reception from the capsule regardless of its position inside the GI tract. It is also conceivable to use array antennas and beamforming technology to achieve better signal strength, higher communication range or equivalently lower required transmit power by the capsule. Lower transmit power would translate to lower consumed energy which could help to alleviate the battery lifetime problem in capsule endoscopy applications.

The statistical pathloss model derived during this research has been contributed to the IEEE 802.15 Task Group 6ma and has been accepted as a part of the standard channel model for the capsule endoscopy use-case. IEEE 802.15.6ma is the revision of the standard IEEE 802.15.6-2012 for wireless body area networks.

The ultimate verification of presented pathloss model will require human subject experiments. As it can be imagined, this is extremely challenging and requires developing a practical hardware prototype. It also involves a very complicated clinical approval process. However, with continuous research by the community, this experimentation could be done under a clinical setting in the future.

Time domain analysis was also conducted to identify the presence of multipath for several capsule and on-body receiver positions. Due to the complexity and variety of the human body organs and tissues, it has been generally assumed that the UWB channel between a capsule endoscope or implant and an on-body receiver could exhibit strong multipath propagation. However, time domain channel responses examined in this research mostly revealed very few noticeable delayed paths (i.e., typically one line-of-sight and one non-line-of-sight paths). This is likely due to the very high attenuation experienced by longer propagation paths inside the human body. Therefore, a tapped-delay-line channel model for capsule endoscopy at UWB frequencies would basically include two main components. However, scenarios where the first path is not necessarily the direct path between the transmitter and receiver were also observed. There are possible capsule and receiver antenna positions that could result in a first path being a diffracted path from the body surface (through creeping waves) while the weaker second path is the direct line-of-sight path between the transmitter-receiver pair. In those scenarios, the arrival time of the first component could be earlier that the arrival time of the direct line-of-sight path between the transmitter-receiver pair. This is again due to the higher speed of the electromagnetics wave on the body surface (for the diffracted path) versus in-body propagation speed (for the direct line-of-sight path). The step size to obtain the forward transmission coefficient of the channel for each sample capsule antenna location in simulations was 20 MHz. Higher sampling resolution in the frequency domain during these measurements could lead to higher resolution in the time domain response of the channel. This might provide more detailed information on multipath characteristics of the communication link; however more powerful computational resources would be needed to ensure a reasonable execution time to generate the results. More extensive studies are needed to obtain the statistical distributions for the amplitude and delay of each component and to further characterize the time domain response of the UWB channel for capsule endoscopy.

The computational platform has also been extended to focus on methodologies that can assist in estimating the position or orientation of a WCE. Although for data communication purposes, it is clearly preferred to have a completely omni-directional antenna for the capsule, the initial results presented here indicate that any directionality (or equivalently any nulls) in the capsule antenna pattern could be exploited to estimate its orientation through observation of the signal strength by a set of on-body receivers. It is conjectured that a greater number of sensors on the abdomen area or lower value for unit angular step could lead to higher accuracy in the estimated orientation. Further studies are needed to determine the optimal locations for these sensors around the abdomen.

As the final part of this thesis, HBC has been studied as another possible communication technology for WCE. More specifically, a parametric FEM-based model has been developed to investigate the performance of this technology. The low complexity and energy consumption of HBC make this technology an attractive alternative for implantable or ingestible devices. Since implants are completely located inside the human body, physical measurements are no longer possible to examine the channel. Therefore, a simulation platform including a full human body model is very useful to study and characterize the implant HBC channel. The computational platform which includes the HBC model allows researchers to study the HBC channel by considering variable electrode size and plate separation, placement on the body, as well as designing virtual experiments to better understand the impact of variable return path distance for a fixed forward path through the human body. As discussed in Chapter 5, the S_{21} results for on-body simulation scenario match the bandpass HBC channel attenuation profile from measurements reported in the literature. The implant communication link is less affected by the environmental variables as both forward and return paths are confined within the human body. The S_{21} results for several in-body to on-body scenarios presented in this research match the channel attenuation profile measured with liquid phantom and the human body with appropriate adjustment of the model parameters. Development of the presented platform is the first step toward a comprehensive study of the implant HBC channel. The research in this thesis can be continued by further extending the computational human body model to include various postures. Also, further studies on the distribution of the electric field inside the body would be necessary to investigate the potential impact of using HBC on implant devices such as pacemakers or capsule endoscopes.

Bibliography

[1] "IEEE Standard for Local and metropolitan area networks - Part 15.6: Wireless Body Area Networks," in IEEE Std 802.15.6-2012 , vol., no., pp.1-271, 29 Feb. 2012, doi: 10.1109/IEEESTD.2012.6161600

[2] R. Chávez-Santiago, K. Sayrafian-Pour, A. Khaleghi, K. Takizawa, J. Wang, I. Balasingham, and H. -B. Li, “Propagation Models for IEEE 802.15.6 Standardization of Implant Communication in Body Area Networks,” in IEEE Communications Magazine, vol. 51, no. 8, pp. 80-87, August 2013, doi: 10.1109/MCOM.2013.6576343.

[3] K. Yekeh Yazdandoost, and K. Sayrafian, "Channel model for Body Area Network," IEEE P802.15 Working Group for Wireless Personal Area Networks, IEEE P802.15-08-0780-12-0006, November 2010.

[4] K. Sayrafian-Pour, W. Yang, J. Hagedorn, J. Terrill, and K. Y. Yazdandoost, “A statistical path-loss model for medical implant communication channels,” IEEE 20th International Symposium on Personal, Indoor and Mobile Radio Communications, pp. 2995–2999, September 2009.

[5] K. Sayrafian-Pour, J. Hagedorn, W. -B. Yang and J. Terrill, "A Virtual Reality Platform to study RF propagation in body area networks," 2012 IEEE 3rd International Conference on Cognitive Infocommunications (CogInfoCom), Kosice, Slovakia, 2012, pp. 709-713, doi: 10.1109/CogInfoCom.2012.6421944.

[6] K.Y. Yazdandoost and R. Kohno, "UWB antenna for wireless body area network," 2006 Asia-Pacific Microwave Conference, Yokohama, Japan, 2006, pp. 1647-1652, doi: 10.1109/APMC.2006.4429724.

[7] K.Y. Yazdandoost and R. Kohno, "An antenna for medical implant communications system," 2007 European Microwave Conference, Munich, Germany, 2007, pp. 968-971, doi: 10.1109/EUMC.2007.4405356.

[8] K.Y.Yazdandoost and R.Kohno, “Body Implanted Medical Device Communications”, IEICE Transactions on Communications, 2009, Volume E92.B, Issue 2, Pages 410-417, February 2009, doi: 10.1587/transcom.E92.B.410.

[9] J. Wang and Q. Wang, “Channel Modeling and BER Performance of an Implant UWB Body Area Link,” 2009 2nd International Symposium on Applied Sciences in Biomedical and Communication Technologies, Bratislava, Slovakia, 2009, pp. 1-4, doi: 10.1109/ISABEL.2009.5373707.

[10] D. Anzai, K. Katsu, R. Chavez-Santiago, Q. Wang, D. Plettemeier, J. Wang, and I. Balasingham, “Experimental Evaluation of Implant UWB-IR Transmission with Living Animal for Body Area Networks,” IEEE Transactions on Microwave Theory and Techniques, vol. 62, no. 1, pp. 183-192, January 2014, doi: 10.1109/TMTT.2013.2291542.

[11] M. Kanaan and M. Suveren, “A novel frequency-dependent path loss model for ultra-wideband implant body area networks, Measurement, vol 68, pp. 117-127, February 2015, https://doi.org/10.1016/j.measurement.2015.02.040.

[12] P. Leelatien, K. Ito, K. Saito, M. Sharma and A. Alomainy, "Channel Characteristics and Wireless Telemetry Performance of Transplanted Organ Monitoring System Using Ultrawideband Communication," IEEE Journal of Electromagnetics, RF and Microwaves in Medicine and Biology, vol. 2, no. 2, pp. 94-101, June 2018, doi: 10.1109/JERM.2018.2827779.

[13] M. Särestöniemi, C. Pomalaza-Ráez, C. Kissi and J. Iinatti, "Simulation and Measurement Data-Based Study on Fat as Propagation Medium in WBAN Abdominal Implant Communication Systems," IEEE Access, vol. 9, pp. 46240-46259, 2021, doi: 10.1109/ACCESS.2021.3068116.

[14] G. Iddan, G. Meron, A. Glukhovsky, and P. Swain, “Wireless capsule endoscopy,” Nature, vol. 405, pp. 417, May 2000, doi: 10.1038/35013140.

[15] M. Penazzio et al., “Small-bowel capsule endoscopy and device-assisted enteroscopy for diagnosis and treatment of small-bowel disorders: European Society of Gastrointestinal Endoscopy (ESGE) Clinical Guideline.” Endoscopy vol. 47, pp. 352-76, 2015, doi:10.1055/s-0034-1391855.

[16] M. Alizadeh, OH Maghsoudi, K. Sharzehi, H. Reza Hemati, A. Kamali Asl, and A. Talebpour “Detection of small bowel tumor in wireless capsule endoscopy images using an adaptive neuro-fuzzy inference system,” The Journal of Biomedical Research, vol 31, pp. 419-427, 2017, doi: 10.7555/JBR.31.20160008.

[17] G. Ciuti, A. Menciassi, and P. Dario, “Capsule Endoscopy: From Current Achievements to Open Challenges,” IEEE Reviews in Biomedical Engineering, vol. 4, pp. 59-72, 2011, doi: 10.1109/RBME.2011.2171182.

[18] M.R. Yuce, and T. Dissanayake, “Easy-to-Swallow Wireless Telemetry,” IEEE Microwave Magazine, vol. 13, no. 6, pp. 90–101, October 2012, doi: 10.1109/MMM.2012.2205833.

[19] C. Van de Bruaene, D. De Looze, and P. Hindryckx, “Small bowel capsule endoscopy: Where are we after almost 15 years of use?” World journal of gastrointestinal endoscopy, vol. 7(1), pp. 13-36, January 2015, doi:10.4253/wjge.v7.i1.13.

[20] Z. Liao, R. Gao, C. Xu, and Z.-S. Li, “Indications and detection, completion, and retention rates of small-bowel capsule endoscopy: a systematic review,” Gastrointestinal Endoscopy, vol. 71(2), pp. 280-286, February 2010, doi: 10.1016/j.gie.2009.09.031.

[21] IEEE 802.15 Wireless Speciality Networks Task Group 6ma (https://www.ieee802.org/15/pub/TG6ma.html)

[22] J. Shi and J. Wang, "Channel characterization and diversity feasibility for in-body to on-body communication using low-band UWB signals," 3rd International Symposium on Applied Sciences in Biomedical and Communication Technologies (ISABEL 2010), pp. 1-4, Rome, Italy, 2010, doi: 10.1109/ISABEL.2010.5702784.

[23] K. M. S. Thotahewa, J. -M. Redoutè and M. R. Yuce, "Propagation, Power Absorption, and Temperature Analysis of UWB Wireless Capsule Endoscopy Devices Operating in the Human Body," IEEE Transactions on Microwave Theory and Techniques, vol. 63, no. 11, pp. 3823-3833, November 2015, doi: 10.1109/TMTT.2015.2482492.

[24] Y. Shimizu, D. Anzai, R. Chavez-Santiago, P. A. Floor, I. Balasingham and J. Wang, "Performance Evaluation of an Ultra-Wideband Transmit Diversity in a Living Animal Experiment," IEEE Transactions on Microwave Theory and Techniques, vol. 65, no. 7, pp. 2596-2606, July 2017, doi: 10.1109/TMTT.2017.2669039.

[25] S. Perez-Simbor, C. Andreu, C. Garcia-Pardo, M. Frasson and N. Cardona, "UWB Path Loss Models for Ingestible Devices," IEEE Transactions on Antennas and Propagation, vol. 67, no. 8, pp. 5025-5034, August 2019, doi: 10.1109/TAP.2019.2891717.

[26] M. Barbi, C. Garcia-Pardo, A. Nevárez, V. Pons Beltrán and N. Cardona, "UWB RSS-Based Localization for Capsule Endoscopy Using a Multilayer Phantom and In Vivo

Measurements," IEEE Transactions on Antennas and Propagation, vol. 67, no. 8, pp. 5035-5043, August 2019, doi: 10.1109/TAP.2019.2916629.

[27] M. Särestöniemi, C.P. Raez, M. Berg, C. Kissi, M. Hämäläinen, and J. Iinatti, “WBAN Radio Channel Characteristics Between the Endoscope Capsule and on-Body Antenna,” Body Area Networks: Smart IoT and Big Data for Intelligent Health Management (BODYNETS 2019), Lecture Notes of the Institute for Computer Sciences, Social Informatics and Telecommunications Engineering, vol. 297, Springer, November 2019, doi:10.1007/978-3-030-34833-5_27.

[28] M. Särestöniemi, C. Pomalaza-Ráez, C. Kissi, M. Berg, M. Hämäläinen and J. Iinatti, "WBAN Channel Characteristics Between Capsule Endoscope and Receiving Directive UWB On-Body Antennas," IEEE Access, vol. 8, pp. 55953-55968, March 2020, doi: 10.1109/ACCESS.2020.2982247.

[29] M. Särestöniemi, A. Taparugssanagorn, J. Wisanmongkol, M. Hämäläinen and J. Iinatti, "Comprehensive Analysis of Wireless Capsule Endoscopy Radio Channel Characteristics Using Anatomically Realistic Gastrointestinal Simulation Model," IEEE Access, vol. 11, pp. 35649-35669, March 2023, doi: 10.1109/ACCESS.2023.3263555.

[30] H. Baldus, S. Corroy, A. Fazzi, K. Klabunde, and T. Schenk, "Human-centric connectivity enabled by body-coupled communications", IEEE Communications Magazine, vol. 47, no. 6, pp. 172-178, June 2009, doi: 10.1109/MCOM.2009.5116816.

[31] T. Zimmerman, “Personal Area Networks (PAN): Near-Field Intra-body Communication,” Master’s thesis, MIT, Cambridge, MA, 1995.

[32] T. Handa, S. Shoji, S. Ike, S. Takeda, and T. Sekiguchi, “A very low-power consumption wireless ECG monitoring system using body as a signal transmission medium,” Proceedings of the International Solid State Sensors and Actuators Conference (Transducers '97), vol. 2, pp. 1003–1006, June 1997, doi: 10.1109/SENSOR.1997.635344.

[33] D. P. Lindsey, E. L. McKee, M. L. Hull, and S. M. Howell, “A new technique for transmission of signals from implantable transducers,” IEEE Transactions on Biomedical Engineering, vol. 45, no. 5, pp. 614–619, May 1998, doi: 10.1109/10.668752.

[34] T. G. Zimmerman, “Personal area networks: Near-field intrabody communication,” IBM Systems Journal, vol. 35, no. 3–4, pp. 609–617, 1996, doi: 10.1147/sj.353.0609.

[35] M. A. Callejon, L. M. Roa, J. Reina-Tosina, and D. Naranjo-Hernandez, “Study of Attenuation and Dispersion Through the Skin in Intrabody Communications Systems,” IEEE Transactions on Information Technology in Biomedicine, vol. 16, no. 1, pp. 159–165, January 2012, doi: 10.1109/TITB.2011.2171702.

[36] M. A. Callejon, D. Naranjo-Hernandez, J. Reina-Tosina, and L. M. Roa, “A Comprehensive Study into Intrabody Communication Measurements,” IEEE Transactions on Instrumentation and Measurements, vol. 62, no. 9, pp. 2446–2455, September 2013, doi: 10.1109/TIM.2013.2258766.

[37] M. S. Wegmüller, “Intra-body Communication for Biomedical Sensor Networks,” PhD thesis, ETH Zurich, Switzerland, July 2007.

[38] M. S. Wegmüller, M. Oberle, N. Felber, N. Kuster, and W. Fichtner, “Galvanical Coupling for Data Transmission through the Human Body,” 2006 IEEE Instrumentation and Measurement Technology Conference Proceedings, pp. 1686-1689, Italy, April 2006, doi: 10.1109/IMTC.2006.328197.

[39] M. S. Wegmüller, A. Kuhn, J. Froehlich, M. Oberle, N. Felber, N. Kuster, and W. Fichtner, “An Attempt to Model the Human Body as a Communication Channel,” IEEE Transactions on Biomedical Engineering, vol. 54, no. 10, pp. 1851–1857, October 2007 , doi: 10.1109/TBME.2007.893498.

[40] J. Bae, H. Cho, K. Song, H. Lee, and H.-J. Yoo, “The Signal Transmission Mechanism on the Surface of Human Body for Body Channel Communication,” IEEE Transactions on Microwave Theory and Techniques, vol. 60, no. 3, pp. 582–593, March 2012, doi: 10.1109/TMTT.2011.2178857.

[41] R. Xu, H. Zhu and J. Yuan, "Electric-Field Intrabody Communication Channel Modeling with Finite-Element Method," in IEEE Transactions on Biomedical Engineering, vol. 58, no. 3, pp. 705-712, March 2011, doi: 10.1109/TBME.2010.2093933.

[42] Z. Lucev, I. Krois, and M. Cifrek, “A Capacitive Intrabody Communication Channel from 100 kHz to 100 MHz”, IEEE Transactions on Instrumentation and Measurement, vol. 61, no. 12, pp. 3280–3289, December 2012, doi: 10.1109/TIM.2012.2205491.

[43] Z. Lucev Vasic, “Intrabody Communication based on Capacitive Method,” Doctoral Thesis, Zagreb 2014.

[44] J. Park, H. Garudadri, and P. P. Mercier, “Channel Modeling of Miniaturized Battery-Powered Capacitive Human Body Communication Systems,” IEEE Transactions on

Biomedical Engineering, vol. 64, no. 2, pp. 452–462, February 2017, doi: 10.1109/TBME.2016.2560881.

[45] M. Pereira, G. Alvarez-Botero, F. Rangel de Sousa, “Characterization and Modeling of the Capacitive HBC Channel,” IEEE Transactions on Instrumentation & Measurement, Vol. 64, no.10, Oct. 2015

[46] M. S. Wegmueller, M. Hediger, T. Kaufmann, F. Buergin and W. Fichtner, "Wireless Implant Communications for Biomedical Monitoring Sensor Network," 2007 IEEE International Symposium on Circuits and Systems, pp. 809-812, May 2007, doi: 10.1109/ISCAS.2007.378029.

[47] M. S. Wegmueller, M. Hediger, T. Kaufmann, M. Oberle, N. Kuster and W. Fichtner, "Investigation on Coupling Strategies for Wireless Implant Communications," IEEE Instrumentation & Measurement Technology Conference IMTC 2007, pp. 1-4, May 2007, doi: 10.1109/IMTC.2007.379310.

[48] M. Swaminathan, F. S. Cabrera, J. S. Pujol, U. Muncuk, G. Schirner and K. R. Chowdhury, "Multi-Path Model and Sensitivity Analysis for Galvanic Coupled Intra-Body Communication Through Layered Tissue," IEEE Transactions on Biomedical Circuits and Systems, vol. 10, no. 2, pp. 339-351, April 2016, doi: 10.1109/TBCAS.2015.2412548.

[49] S. Zhang, S.-H. Pun, P. U. Mak, Y. P. Qin, Y. H. Liu, Y. M. Gao, and M. I. Vai, "Experimental Verifications of Low Frequency Path Gain (PG) Channel Modeling for Implantable Medical Device (IMD)," IEEE Access, vol. 7, pp. 11934-11945, January 2019, doi: 10.1109/ACCESS.2019.2892130.

[50] D. Naranjo-Hernández, A. Callejón-Leblic, Ž. Lučev Vasić, M. Seyedi, and Y.-M. Gao, "Past Results, Present Trends, and Future Challenges in Intrabody Communication," Wireless Communications and Mobile Computing, vol. 2018, Article ID 9026847, March 2018. https://doi.org/10.1155/2018/9026847.

[51] J. Li, Z. Nie, Y. Liu, L. Wang and Y. Hao, "Characterization of In-Body Radio Channels for Wireless Implants," IEEE Sensors Journal, vol. 17, no. 5, pp. 1528-1537, March 2017, doi: 10.1109/JSEN.2016.2635700.

[52] M. Li, Y. Song, G. Wang, Q. Hao, and K. Zang, “Characterization of the Implantable Intra-body Communication based on Capacitive Coupling by Transfer Function,” 10th International Conference on Sensing Technology (ICST), pp. 1–5, November 2016, doi: 10.1109/ICSensT.2016.7796259.

[53] M. Li, Y. Song, Y. Hou, N. Li, Y. Jiang, M. Sulaman, and Q. Hao "Comparable Investigation of Characteristics for Implant Intra-Body Communication Based on Galvanic and Capacitive Coupling," IEEE Transactions on Biomedical Circuits and Systems, vol. 13, no. 6, pp. 1747-1758, Dec. 2019, doi: 10.1109/TBCAS.2019.2940827.

[54] Ž. Lučev Vasić, M. Cifrek, Y. Gao, and M. Du, "Preliminary Characterization of Capacitive Intrabody Communication Channel under Implantable-Like Conditions," 2020 IEEE International Instrumentation and Measurement Technology Conference (I2MTC), pp. 1-5, May 2020, doi: 10.1109/I2MTC43012.2020.9128564.

[55] M. Roglić, Y. Gao, I. Artić and Ž. Lučev Vasić, "Characterization of Implantable Capacitive Intrabody Communication Channel between In-body and On-body Devices on a Liquid Phantom," 2023 IEEE International Symposium on Medical Measurements and Applications (MeMeA), pp. 1-6, June 2023, doi: 10.1109/MeMeA57477.2023.10171879.

[56] J. Jang *et al.*, "4-Camera VGA-resolution Capsule Endoscope with 80Mb/s Body-Channel Communication Transceiver and Sub-cm Range Capsule Localization," 2018 IEEE International Solid-State Circuits Conference - (ISSCC), pp. 282-284, February 2018, doi: 10.1109/ISSCC.2018.8310294.

[57] J. Jang and H.-J. Yoo, "A Capsule Endoscope System for Wide Visualization Field and Location Tracking," 2018 IEEE Biomedical Circuits and Systems Conference (BioCAS), pp. 1-4, October 2018, doi: 10.1109/BIOCAS.2018.8584812.

[58] J. Jang *et al.*, "A Four-Camera VGA-Resolution Capsule Endoscope System With 80-Mb/s Body Channel Communication Transceiver and Sub-Centimeter Range Capsule Localization," IEEE Journal of Solid-State Circuits, vol. 54, no. 2, pp. 538-549, February 2019, doi: 10.1109/JSSC.2018.2873630.

[59] B. Kibret, A. K. Teshome, D. T. H. Lai, “Human Body as Antenna and Its Effect on Human Body Communications,” Progress in Electromagnetics Research, Vol. 148, 2014.

[60] M. Hanscom and D.R. Cave, “Endoscopic Capsule Robot-based Diagnosis, Navigation and Localization in the Gastrointestinal Tract,” Frontiers in Robotics and AI, vol. 9, September 2022, doi:10.3389/frobt.2022.896028.

[61] K. Y. Yazdandoost, "Antenna for Wireless Capsule Endoscopy at Ultra-Wideband Frequency," 2016 IEEE 27th Annual International Symposium on Personal, Indoor,

and Mobile Radio Communications (PIMRC), pp. 1-5, September 2016, doi: 10.1109/PIMRC.2016.7794781.

[62] K. Yekeh Yazdandoost and R. Kohno. “UWB Antenna for Wireless Body Area Network,” 2006 Asia-Pacific Microwave Conference, pp. 1647-1652, December 2006, doi: 10.1109/APMC.2006.4429724.

[63] K. Y. Yazdandoost and R. Kohno, "Ultra-wideband L-loop antenna," 2005 IEEE International Conference on Ultra-Wideband, pp. 201-205, September 2005, doi: 10.1109/ICU.2005.1569984.

[64] Given Imaging– PillCam® Capsule Endoscopy User Manual, RAPID® v8.0, March 2013, http://www.medtronic.com/content/dam/covidien/library/us/en/product/diagnostic-testing/pillcam-rapid-v8-user-manual.pdf

[65] K. Ladic, K. Sayrafian, D. Šimunić and K. Y. Yazdandoost, "Wireless Channel Characterization for UWB Communication in Capsule Endoscopy," in IEEE Access, vol. 11, pp. 95858-95873, 2023, doi: 10.1109/ACCESS.2023.3310216.

[66] S. Perez-Simbor, K. Ladic, C. Garcia-Pardo, K. Sayrafian, D. Simunic, and N. Cardona, "Impact of Measurement Points Distribution on the Parameters of UWB Implant Channel Model," 2018 IEEE Conference on Standards for Communications and Networking (CSCN), pp. 1-6, October 2018, doi: 10.1109/CSCN.2018.8581808.

[67] H. Tangelder and A. Fabri, “dD Spatial Searching,” CGAL User and Reference Manual, CGAL Editorial Board, 4.14 ed., 2019, available at: https://doc.cgal.org/latest/Spatial_searching/index.html

[68] A. Khaleghi, R. Chávez-Santiago, and I. Balasingham, “Ultra-wideband Statistical Propagation Channel Model for Implant Sensors in the Human Chest,” IET Microwaves, Antennas Propagation, vol. 5, no. 15, pp. 1805-1812, December 2011, doi: 10.1049/iet-map.2010.0537.

[69] J. Wang and Q. Wang, "Channel Modeling and BER Performance of an Implant UWB Body Area Link," 2009 2nd International Symposium on Applied Sciences in Biomedical and Communication Technologies, pp. 1-4, November 2009, doi: 10.1109/ISABEL.2009.5373707.

[70] S. Perez-Simbor, C. Garcia-Pardo, and N. Cardona, "Initial Delay Domain UWB Channel Characterization for In-Body Area Networks," 2019 13th International Symposium on Medical Information and Communication Technology (ISMICT), pp. 1-5, May 2019, doi: 10.1109/ISMICT.2019.8743767.

[71] J. Shi, D. Anzai, and J. Wang, “Channel Modeling and Performance Analysis of Diversity Reception for Implant UWB Wireless Link,” IEICE Transactions on Communications, vol. E95-B, no.10, pp.3197-3205, October 2012, doi: 10.1587/transcom.E95.B.3197.

[72] S. Castelló-Palacios, C. Garcia-Pardo, M. Alloza-Pascual, A. Fornes-Leal, N. Cardona and A. Vallés-Lluch, "Gel Phantoms for Body Microwave Propagation in the (2 to 26.5) GHz Frequency Band," IEEE Transactions on Antennas and Propagation, vol. 67, no. 10, pp. 6564-6573, October 2019, doi: 10.1109/TAP.2019.2920293

[73] P. K. Kundu, M. Cohen, D.R. Dowling, “Fluid Mechanics,” Fifth Edition, Academic Press, Inc., pp. 71-72, 2012.

[74] Cash, J.R., and Karp, A.H. 1990, ACM Transactions on Mathematical Software, vol. 16, pp. 201– 222.

[75] Press, W. H., et al., 1992, Numerical Recipes in C, Second Edition, Cambridge University Press, pp. 714-722.

[76] ParaView, available at: https://www.paraview.org

[77] VTK, available at: https://www.paraview.org

[78] Fischer, D., Schreiber, R., Levi, D., and Eliakim, R. Capsule endoscopy: The localization system. Gastrointest. Endosc. Clin. N. Am. 14 (1), 25–31, 2004., doi:10.1016/j.giec.2003.10.020

[79] Marya, N., Karellas, A., Foley, A., Roychowdhury, A., and Cave, D. Computerized 3-dimensional localization of a video capsule in the abdominal cavity: Validation by digital radiography. Gastrointest. Endosc. 79 (4), 669–674, 2014., doi:10.1016/j.gie.2013.11.022

[80] K. Yu, I. Sharp, Y. Guo, “Ground-Based Wireless Positioning,” New York, Wiley, 2009.

[81] S. Zeising, A. S. Thalmayer, M. Lübke, G. Fischer and J. Kirchner, "Localization of Passively Guided Capsule Endoscopes—A Review," in IEEE Sensors Journal, vol. 22, no. 21, pp. 20138-20155, 1 Nov.1, 2022, doi: 10.1109/JSEN.2022.3205721.

[82] H. Mateen et al., “Localization of Wireless Capsule Endoscope: A Systematic Review,” IEEE Sensors Journal, Vol. 17, No. 5, pp. 1197–1206, March 2017.

[83] I. Umay et al., “Localization and Tracking of Implantable Biomedical Sensors.” Sensors (Basel, Switzerland) vol. 17,3 583. 13 Mar. 2017, doi:10.3390/s17030583

[84] Ye, Y., “Bounds on RF Cooperative Localization for Video Capsule Endoscopy,” Ph.D. thesis, Worcester Polytechnic Institue, Worcester, MA, USA, 2013

[85] A. S. Bjornevik, “Localization and Tracking of Intestinal Paths for Wireless Capsule Endoscopy,” Master of Science Thesis, Norwegian University of Science and Technology, Norway, 2015.

[86] M. Barbi et al., “UWB RSS-based localization for capsule endoscopy using a multilayer phantom and in vivo measurements,” IEEE Trans. Antennas Propag., vol. 67, no. 8, pp. 5035–5043, Aug. 2019.

[87] Hu, C.; Ren, Y.; You, X.; Yang, W.; Song, S.; Xiang, S.; He, X.; Zhang, Z.; Meng, M.Q.H. Locating Intra-Body Capsule Object by Three-Magnet Sensing System. IEEE Sens. J. 2016, 16, 5167–5176.

[88] Wang, M.; Shi, Q.; Song, S.; Hu, C.; Meng, M.Q.H. A Novel Relative Position Estimation Method for Capsule Robot Moving in Gastrointestinal Tract. Sensors 2019, 19, 2746.

[89] Pham, D.M.; Aziz, S.M. A real-time localization system for an endoscopic capsule using magnetic sensors. Sensors 2014, 14, 20910–20929.

[90] Memduh Suveren.; Muzaffer Kanaan. 5D Magnetic Localization for Wireless Capsule Endoscopy Using the Levenberg-Marquardt Method and Artificial Bee Colony Algorithm. 2019 IEEE 30th International Symposium on Personal, Indoor and Mobile Radio Communications (PIMRC Workshops), Istanbul, Turkey, 8–11 September 2019.

[91] Shimizu, R.; Shirai, R.; Hashimoto, M. Position and Posture Estimation of Capsule Endoscopy with a Single Wearable Coil Toward Daily Life Diagnosis. In Proceedings of the 2020 IEEE 63rd International Midwest Symposium on Circuits and Systems (MWSCAS), Springfield, MA, USA, 9–12 August 2020.

[92] Islam, M.N.; Fleming, A.J. Resonance-Enhanced Coupling for Range Extension of Electromagnetic Tracking Systems. IEEE Trans. Magn. 2018, 54, 1–9

[93] Zeising, S.; Anzai, D.; Thalmayer, A.; Fischer, G.; Kirchner, J. Evaluation of the Impact of Static Interference on an Empirical Data Based Static Magnetic Localization Setup for Capsule Endoscopy. Curr. Dir. Biomed. Eng. 2020

[94] L. Liu, C. Hu, W. Cai, MQ-H Meng, “Capsule endoscope localization based on computer vision technique,” Annual International Conference of the IEEE In Engineering in Medicine and Biology Society (EMBC), pp. 3711–3714, 2009.

[95] D. K. Iakovidis, E. Spyrou, D. Diamantis, I. Tsiompanidis, “Capsule endoscope localization based on visual features,” 2013 IEEE 13th International Conference on Bioinformatics and Bioengineering (BIBE), pp. 1–4, 2013.

[96] D. K. Iakovidis, G. Dimas, A. Karargyris, F. Bianchi, G. Ciuti and A. Koulaouzidis, "Deep Endoscopic Visual Measurements," in IEEE Journal of Biomedical and Health Informatics, vol. 23, no. 6, pp. 2211-2219, Nov. 2019, doi: 10.1109/JBHI.2018.2853987.

[97] G. Bao, “Body SLAM: Simultaneous Localization and Mapping inside Human Body,” PhD Thesis, Worcester Polytechnic Institute, 2014.

[98] M. Oliveira, H. Araujo, I. N. Figueiredo, L. Pinto, E. Curto, and L. Perdigoto, “Registration of consecutive frames from wireless capsule endoscopy for 3D motion estimation,” IEEE Access, vol. 9, pp. 119533–119545, 2021.

[99] G. Bao, K. Pahlavan, and L. Mi, “Hybrid localization of microrobotic endoscopic capsule inside small intestine by data fusion of vision and RF sensors,” IEEE Sens. J., vol. 15, no. 5, pp. 2669–2678, May 2015.

[100] S. S. Vedaei and K. A. Wahid, “A localization method for wireless capsule endoscopy using side wall cameras and IMU sensor,” Sci. Rep., vol. 11, no. 1, p. 11204, Dec. 2021.

[101] K. Ladic, K. Sayrafian, M. Alasti, K. Y. Yazdandoost and D. Simunic, "A Study of Capsule Endoscopy Orientation Estimation Using Received Signal Strength," 2018 IEEE 29th Annual International Symposium on Personal, Indoor and Mobile Radio Communications (PIMRC), Bologna, Italy, 2018, pp. 345-349, doi: 10.1109/PIMRC.2018.8580786.

[102] K. Ladic, K. Sayrafian, G. Noetscher and D. Simunic, "A Simulation Platform to Study the Human Body Communication Channel," 2019 41st Annual International Conference of the IEEE Engineering in Medicine and Biology Society (EMBC), Berlin, Germany, 2019, pp. 4040-4043, doi: 10.1109/EMBC.2019.8857883.

List of figures

List of tables

Biography

Katjana Ladić (née Krhač) was born in 1991 in Čakovec. She enrolled at the University of Zagreb, Faculty of Electrical Engineering and Computing in 2010. She graduated with the master of science degree in information and communication technology (profile wireless communications) in 2016.

She enrolled on a postgraduate study of electronics at the Faculty of Electrical Engineering and Computing in October 2016. From 2016. to 2021. she was a guest researcher at the Information Technology Laboratory (ITL) of the National Institute of Standards and Technology (NIST), Gaithersburg, Maryland. Since 2021 she is employed a research associate at ITL NIST working on projects related to the application of the Internet-of-Things (IoT) in healthcare. Her research interests include analysis and modeling of wireless communication channels for wearables and implants.

She is a co-author of a journal paper and several international conference papers. She has been recipient of the IEEE CSCN 2018 best paper award and the NIST ITL outstanding conference paper awards in 2019. and 2022.

List of publications

Journal articles and review articles in CC journals

[1] **Katjana Ladic**, Kamran Sayrafian, Dina Šimunić, and Kamya Y. Yazdandoost, "Wireless Channel Characterization for UWB Communication in Capsule Endoscopy," in IEEE Access, vol. 11, pp. 95858-95873, 2023, doi: 10.1109/ACCESS.2023.3310216.

Scientific conference papers with international peer-review

[1] **Katjana Ladic**, Kamran Sayrafian, Mehdi Alasti, Kamya Y. Yazdandoost, and Dina Simunic, “A Study of Capsule Endoscopy Orientation Estimation Using Received Signal Strength,” *2018 IEEE 29th Annual International Symposium on Personal, Indoor and Mobile Radio Communications (PIMRC),* Bologna, Italy, 2018, pp. 345-349, doi:10.1109/PIMRC.2018.8580786.

[2] Sofia Perez-Simbor, **Katjana Ladic**, Concepcion Garcia-Pardo, Kamran Sayrafian, Dina Simunic, and Narcis Cardona, “Impact of Measurement Points Distribution on the Parameters of UWB Implant Channel Model,” *2018 IEEE Conference on Standards for Communications and Networking (CSCN),* Paris, France, 2018, pp. 1-6, doi: 10.1109/CSCN.2018.8581808.

[3] **Katjana Ladic**, Kamran Sayrafian, Gregory Noetscher, and Dina Simunic, “A Simulation Platform to Study the Human Body Communication Channel,” *2019 41st Annual International Conference of the IEEE Engineering in Medicine and Biology Society (EMBC),* Berlin, Germany, 2019, pp. 4040-4043, doi: 10.1109/EMBC.2019.8857883.

Životopis

Katjana Ladić (djevojački Krhač) rođena je 1991. godine u Čakovcu. Studij elektrotehnike na Fakultetu elektrotehnike i računarstva Sveučilišta u Zagrebu (FER) upisala je 2010. godine. Diplomirala je s naglaskom na znanstveno-istraživačkom radu u srpnju 2016. godine, na studiju informacijske i komunikacijske tehnologije, profil radiokomunikacije.

Poslijediplomski doktorski studij elektrotehnike na FER-u upisala je u listopadu 2016. Od 2016. do 2021. g. bila je gostujući istraživač u Laboratoriju za informacijsku tehnologiju Nacionalnog instituta za standarde i tehnologiju (National Institute of Standards and Technology, NIST), Gaithersburg, Maryland, gdje od 2021.g. radi kao znanstveni suradnik na projektima vezanim uz primjenu internet stvari (Internet of Things, IoT) u zdravstvu. Njeni profesionalni i znanstveni interesi uključuju analizu i modeliranje bežičnih komunikacijskih sustava za prijenos signala ljudskim tijelom.

Autorica je članka u CC časopisu te više članaka objavljenih u zbornicima radova s međunarodnog znanstvenog skupa. Dobitnica je nagrade za najbolji rad na “IEEE CSCN 2018”, te NIST ITL nagrade za izvanredni konferencijski rad 2019. i 2022.godine.